SUSPENDED-CORE PHOTONIC MICROCELLS MADE BY POST-PROCESSING MICRO-STRUCTURED OPTICAL FIBERS

CHAO WANG

Ph.D

The Hong Kong Polytechnic Univerysity

2014

The Hong Kong Polytechnic Univerysity

Department of Electrical Engineering

SUSPENDED-CORE PHOTONIC MICROCELLS MADE BY POST-PROCESSING MICRO-STRUCTURED OPTICAL FIBERS

CHAO WANG

A thesis submitted in partial fulfillment of the requirements for the degree of Doctor of Philosophy

August 2013

CERTIFICATE OF ORIGINALITY

I hereby declare that this thesis is my own work and that, to the best of my knowledge and belief, it reproduces no material previously published or written, nor material that has been accepted for the award of any other degree or diploma, except where due acknowledgement has been made in the text.

Chao WANG (Name of student)

ABSTRACT

Micro-structured Optical Fibers (MOFs) have attracted plenty of research interests for their unusual properties such as endlessly single mode operation, high birefringence, high non-linearity, and novel dispersion. The MOFs with holey structure also provides degrees of freedom to modify their properties by post-processing techniques. In this dissertation, a novel technique has been demonstrated for fabricating in-line suspended-core (SC) photonic microcells by post-processing holey MOFs. The technique is highly flexible in making SC microcells with various cross-sectional shapes. These microcells may find versatile applications in photonic sensors and devices.

The technique involves opening of selected air-hole at the end of a MOF, pressurization of the air-holes, and tapering the MOF at selected locations. The outcome is a photonic microcell with a SC section with reduced core dimension and significantly inflated air-holes. The microcells possess the unique properties of the SC fibers (SCFs), but avoid the problem of large connection loss with standard single mode fibers. The insertion loss resulted from the adiabatic transitions between the SC region and the MOF pigtails are typically less than ~0.2 dB at 1550 nm. This makes the microcells easier to be integrated into standard fiber optic systems. The air-holes surrounding the SC of a microcell can be made significantly larger and hence the outer cladding walls thinner than those of a typical SCF, making it easier to fill fluidic materials into the holes transversely through side holes, or fabricate micro/nano structures on the SC by, for example, using a focused femtosecond (fs) laser to scan across the fiber from side.

Six types of SC microcells with different core-shape and core-number have been made by the novel post-processing technique. Numerical models based on the finite element method (FEM) have been developed to study the mode properties of three types of the microcells, namely the 6-, 4-, and 3-hole microcells made by inflating

the innermost ring of holes of the PCF. As examples of applications, in-fiber accelerometers, refractive index (RI) sensors, optical gain cells, and long period gratings (LPGs) are made based on these cells.

Based on a photonic microcell with a hexagon-like SC surrounded by six air-holes, a robust micro-cantilever accelerometer within the microcell was made by use of an fs laser micromachining system. The device demonstrated a linear response to acceleration with sensitivity ~2.5 mV/g and a flat frequency response up to 2.5 kHz.

A photonic microcell with a rhombus-like SC and four surrounding holes exhibits a very high group birefringence of about 5×10^{-3}. By filling RI oil into the holes and testing the microcell within a Sagnac loop, it is shown that the birefringence of the SC is highly sensitive to RI. With an oil-filled microcell, a temperature sensor with sensitivity ~3.04 nm/°C (corresponding to RI sensitivity ~9.1×10^3 nm/RIU) is demonstrated. Based on the RI change of gas under pressure, a pressure sensor with a sensitivity of ~0.31 nm/Bar (corresponding to RI sensitivity ~1.5×10^3 nm/RIU) is implemented.

By use of a photonic microcell with a triangular-like SC and three surrounding holes, an optical gain cell was made by drilling holes from the side-walls of microcell and circulating the ethylene glycol solution of rhodamine 6G in the air-columns. A net optical gain of ~ 2.04 dB was experimentally demonstrated at 633 nm with a 1 cm-long microcell side-pumped by a continuous 100mW 532 nm green laser. LPGs in the SCs of 3-hole microcells were also made by use of an fs laser and a point-by-point inscription technique.

ACKNOWLEDGEMENTS

First and foremost I would like to express my sincere appreciation to my supervisor Dr. Wei Jin for his help, support and continuous encouragement throughout my Ph.D period. His perceptive and enlightening guidance on each critical time of my research works provided a great deal of initial insight and inspiration. His enthusiasm and professional attitude in the research on phonics sensors and devices largely aroused my interests in this field, which made me determinedly overcoming the difficulties met in Ph. D study.

Many thanks to all the members of research group for their discussion, company, and each willingness to help. I would like to thank Jun Ma, Ying Wang, and Wa Jin for sharing not only the knowledge and experience but also all the precious moments in the labs and office. Thank Tao Chen for his kind assistance in performing some of the theoretical calculation. Thank Changrui Liao for introducing me the femtosecond laser drilling technique and the fiber tapering technique. Thank Hoi Lut Ho for assistance on preparing the equipment and facilities for some of the experiments. And also thank those who I have just omitted here.

I would also like to thank the Hong Kong Research Grants Council for providing finance support through a GRF project, and the Hong Kong Polytechnic University, Electrical Engineering department for providing convenient facilities and service,

Finally, my special thanks to my wife Lihua Peng, my son Mingxuan Wang, and my parents for their continuous support.

CONTENTS

LIST OF FIGURES

LIST OF TABLES

LIST OF PUBLICATIONS

The following is a list of articles published in journals, and national or international conferences arising from the research works during my Ph.D. study.

Journal Papers

1. Chao Wang, Wei Jin, Jun Ma, Ying Wang, Hoi Lut Ho, and Xin Shi, "Suspended core photonic microcells for sensing and device applications," Optics Letters, 38, 1881-1883 (2013)
2. Wa Jin, Chao Wang, H.F. Xuan, and Wei Jin, “Tunable comb filters and refractive index sensors based on fiber loop mirror with inline high birefringence microfiber”, Optics Letters, 38, 4277-4280 (2013)
3. Ying Wang, Dongning Wang, Chao Wang, and Tianyi Hu, "Compressible fiber optic micro-Fabry-Pérot cavity with ultra-high pressure sensitivity," Optics Express, 21, 14084-14089 (2013)
4. Changrui Liao, Lei Xu, Chao Wang, Dongning Wang, Yiping Wang, Qiao Wang, Kaiming Yang, Zhengyong Li, Xiaoyong Zhong, Jiangtao Zhou, and Yingjie Liu “Tunable phase-shifted fiber Bragg grating based on femtosecond laser fabricated in-grating bubble” Optics Letters, 21, 4473-4476 (2013)
5. Chen-Yu Hong, Jian-Hua Yin, Wei Jin, Chao Wang, Wan-Huan Zhou, and Hong-Hu Zhu, "Comparative study on the elongation measurement of a soil nail using optical lower coherence interferometry method and FBG method," Advances in Structural Engineering, 13, 309-320 (2010)

Conference Papers

6. Chao Wang, Wei Jin, Jun Ma, and Ying Wang, "Suspended-core In-line Micro-cell for Sensing Applications," OFSC 2013 (He Fei, China, 2013). Best Student Paper Award.

7. Chao Wang, Wei Jin, Jun Ma, Wa Jin, and Hoi Lut Ho, "Photonic microcells for novel devices and sensor applications," APOS2013, 8924-207 (2013)
8. Wa Jin, Haifeng Xuan, Chao Wang, and Wei Jin, “High Sensitivity Pressure Sensor Based on a Birefringent Microfiber Loop Mirror,” APOS 2013 (Wuhan, China, 2013)

Chapter 1 : Introduction

Micro-structured Optical Fiber (MOF) is widely adopted as the generic name for fibers with complex refractive index (RI) profiles typically constructed by incorporating the air-columns along the length of the fiber [1]. According to guiding mechanism, MOFs are commonly divided into photonic crystal fibers (PCFs), photonic band gap fibers (PBGFs), suspended core fibers (SCFs), Fresnel fibers, Bragg fibers, and many other types of holey fiber. [2, 3]

At the end of 1990s, the emergence of PCFs and PBGFs with two-dimensional (2D) photonic crystal (PC) claddings have greatly promoted the research and development activities in the area of guide wave photonics. In recent years, SCFs with simple holey structures become new hot spots in MOFs research after PCFs and PBGFs. Compared with conventional all-solid step-index optical fibers, the MOFs possess some new or improved features, such as the properties of endless single mode, guidance in the air, unusual dispersion, high nonlinearity and low bending-loss [2]. Nowadays, the MOFs have found an increasing number of applications in ever-widening fields of science and technology.

Different from the 2D periodical structure in PCFs and PBGFs, the interior of SCFs is typically constructed with one or several core(s) surrounded by just one ring of air-columns. The core(s) of SCFs is (are) connected to the protective jacket tube via spoke-like membranes with nano-scale thickness. Examples of such fibers include grapefruit fiber, steering-wheel fiber, and suspended dual- or multi-core fibers etc. The guiding mechanism of SCFs can be classified into index-guiding (IG) mechanism, which is similar to the mechanism of conventional SI optical fibers and PCFs. However, different from conventional SI fibers and PCFs, the light propagating in SCFs is strongly confined in the fiber core due to the high refractive index (RI) difference between core(s) and cladding, that is, the air-columns. The unique properties of the SCFs have been applied in evanescent field sensing, fluorescent excitation, supercontinuum generation etc. [4]

1.1 Research Motivation and Contributions

In practical applications of the MOFs, the connection between MOFs and the widely used single mode fibers (SMFs) is almost inevitable. However, the difference in mode field distributions between SMF and most MOFs may always cause high loss in connection. To minimize the connection loss, the MOFs with similar mode field distribution to conventional SMF have been designed, such as the ESM-12 PCF from NKT Co. In addition, optimizing the splicing parameter would helpful to decrease the loss for some MOFs. Nevertheless, for most MOFs, the connection problem still exists.

Locally modifying the core shape of MOFs to convert various mode distributions in MOFs to a SMF-like mode could be one solution to the problem. The selective inflation technique on MOFs provides the possibility to locally modify the mode distribution in fiber. By using this fiber post-processing technique, anamorphic core-shape transitions on PCF and mode converters with only 0.1 dB loss at wavelength around 1000 nm are demonstrated [5, 6]. However, producing converters with SMF-like mode distribution on various MOFs may not be an easy task, and the connection problem of SCFs is not solved yet. In this dissertation, new flexible post-processing techniques are developed to produce segments of SCF on a commercially available PCF. The connection problems between the SCF segments and SMF can be solved automatically. Furthermore, the technique also endues the PCF with extra features of SCFs. A series of in-fiber devices can be produced by using the post-processed PCFs.

The contribution of my study include following parts:

(1) A novel method based on modified selective inflation technique is developed to produce local SCFs segment based on PCFs. Different to previous selective inflation technique, all the unselected air-columns collapse during the process of selective inflating PCFs, and the SC structures are be produced with adiabatic transitions to the unprocessed parts of PCFs. Therefore, PCFs can be endued with extra properties of various SC structures by applying the technique. In addition, if the PCFs specially designed for low-loss connection to SMFs are adopted in the process, the insertion loss of the whole structure including SC region, two transitions and two splicing points to SMFs can be optimized to a very low value. Furthermore, in-situ monitoring on the spectrum, which largely facilitates the processing parameter optimization, is available during the process.

(2) Based on the versatile method, six types of in-line SC structures are experimentally realized based on the commercially available PCFs (LMA-10 and ESM-12). Some of the structures are reported for the first time. The whole SMF-PCF-SCF structure introduce very low insertion loss (<1 dB).

Different to the hollow core (HC) microcells which are typically constructed by hermetically splicing PBGFs between SMFs, the SC structure region features a solid core configuration. Nevertheless, both of the two types of structures possess larger holey region inside fiber. Therefore we name the novel in-line SC structure ‘SC microcell’. The SC microcell has lower fraction of optical power propagating in the holey region than HC microcell. However, it may be superior to HC microcell in many aspects, such as anamorphic in core shape, large operation wavelength range, and low connection loss with conventional SMFs.

(3) The optical and mechanical properties of the microcells have been discussed. Numerical studies have been conducted on three types of microcells which are six holes and hexagon-like shaped core microcell (6-hole SC microcell in short), four holes and rhombus-like shaped core microcell (4-hole SC microcell), and three

holes and triangular-like shaped core microcell (3-hole SC microcell).

(4) Based on the 6-hole SC microcell, a novel micro-cantilever can be built inside the microcell with the aid of femtosecond (fs) laser micromachining. It possesses a robust structure and immunity to environment influences. The micro-cantilever based devices exhibit linearly response to the acceleration imposed to the microcell with high sensitivity as well as wide range of flat frequency response.

(5) The 4-hole SC microcells exhibit high birefringence because of the two-fold rotational symmetry core structure. The birefringence of the microcell is highly sensitive to RI of matter adjacent to the core. Integrating the device within a Sagnac loop interferometer, the linear response of the structure to the gas pressure is investigated. With the same test structure, but different microcell which is filled with RI oil, a high sensitivity temperature sensor is demonstrated.

(6) Based on the 3-hole SC microcell, an optical gain cells is demonstrated. The laser dye (Rhodamine 6G solution), which serves as gain medium, is infiltrated in the microcell via the side holes drilled on the jacket tube of the cell with the aid of gas pressure. About 2.5 dB optical gain was measured at 633 nm with 532nm laser side pumping a ~10 mm microcell. Furthermore, a type-II long period grating (LPGs) is successfully inscribed in the SC region of microcells by using the point-by-point fs laser grating inscribing technique. Different to other type-II LPGs, the LPG on microcell is robust because the damages of LPG points only exist inside the cell, and the surface of cell remains intact.

1.2 Outline of the Dissertation

This dissertation is structured as follows:

Chapter 1 (<u>Introduction</u>) Motivation of my research on the fabrication and application of SC microcells are introduced. Contributions of the research are organized and outlined.

Chapter 2 (Background Review) The background information related to our research is given. At first, the basic properties of MOFs are reviewed on the aspects of structure, fabrication, and guiding mechanism. Then the technical details and applications of two fiber post-processing techniques are introduced.

Chapter 3 (Fabrication of the Suspended Core (SC) Micro-cells) We elaborate a modified selective inflation technique used in fabricating the SC microcells. Some innovations of the fabrication process, such as transverse pressurization, splicing with holes in alignment, are highlighted. Based on the technique, six types of SC microcells are made as examples. Comprehensive discussion on the properties of 3 kinds of microcells is presented in the last section.

Chapter 4 (The 6-hole Microcell - Properties and Application) The characteristic of the 6-hole SC microcell is investigated. Based on its unique features, we fabricated a novel micro-cantilever embedded in the microcell with its surface intact. The cantilever is applied in building accelerometer which exhibits linear response to the acceleration imposed on the cell.

Chapter 5 (The 4-hole Microcell - Properties and Applications) The characteristic of the birefringent 4-hole SC microcell is investigated. The birefringence of microcell is highly sensitive to the RI of matter in the holey region. Based on the property, the response of the microcell to gas pressure is investigated by connecting this microcell in a Sagnac loop interferometer. With the same test setup, but different microcell which is filled with RI oil, a sensor with high sensitivity to the environmental temperature is demonstrated.

Chapter 6 (The 3-hole Microcell - Properties and Applications) The characteristic of the 3-hole SC microcell is investigated. Based on its unique features, we propose a novel optical gain cell based on the laser dye (Rhodamine 6G solution). The solution is infiltrated inside the air-columns around the fiber core via the side holes drilled by fs laser, and flows in the air-column under gas pressure. Net optical gain of ~2 dB at 630 nm is measured by a side pumped with green laser. In addition, the fabrication of a type-II LPG in the microcell is introduced. The temperature response of the LPG is measured.

Chapter 7 (Conclusion and Future Works) The summary of the completed works are given. Some suggestions for potential future works extended from the works done in this dissertation are discussed.

1.3 References

[1]. B. Eggleton, C. Kerbage, P. Westbrook, R. Windeler, and A. Hale, "Microstructured optical fiber devices," Optics Express **9**, 698-713 (2001).

[2]. T. M. Monro, and H. Ebendorff-Heidepriem, "Progress in microstructured optical fibers," Annu. Rev. Mater. Res. **36**, 467-495 (2006).

[3]. J. Canning, "Diffraction-free mode generation and propagation in optical waveguides," Optics Communications **207**, 35-39 (2002).

[4]. T. M. Monro, S. Warren-Smith, E. P. Schartner, A. François, S. Heng, H. Ebendorff-Heidepriem, and S. Afshar V, "Sensing with suspended-core optical fibers," Optical Fiber Technology **16**, 343-356 (2010).

[5]. K. Lai, S. Leon-Saval, A. Witkowska, W. Wadsworth, and T. Birks, "Wavelength-independent all-fiber mode converters," Optics Letters **32**, 328-330 (2007).

[6]. A. Witkowska, K. Lai, S. Leon-Saval, W. Wadsworth, and T. Birks, "All-fiber anamorphic core-shape transitions," Optics Letters **31**, 2672-2674 (2006).

Chapter 2 : Background Review

Different to conventional optical fibers, the micro-structured optical fibers (MOFs) possess more complex internal structures which are typically constructed by air-columns or solid rods embedded in the major fiber material. The air-columns of the holey MOFs provide extra microfluidic channels and light-matter interaction space in comparing to the all-solid MOFs. The application region of the MOFs can be further extended by applying the fiber post-processing techniques, such as tapering, etching, micromachining, and milling. Nowadays, the holey MOFs have attracted a great number of interesting in their applications on optical sensing, communication, and device making [1-3].

In this chapter, some background information about the structure, fabrication and mechanism of some representative MOFs will be reviewed firstly. Then two widely used techniques on post-processing optical fibers, that is the fiber tapering technique and the femtosecond (fs) laser micromachining, will be introduced.

2.1 Micro-structured Optical Fibers

The suspended core fibers (SCFs), the photonic crystal fibers (PCFs), and the photonic band gap fibers (PBGFs) which guide light based on different mechanism may be the three most widely studied types in the family of holey MOFs. It is worth to note that many other types of MOFs, such as Fresnel fibers and Bragg fibers, possess extra unique properties. [4-6] However, limited by the length of thesis, the discussion in this part will be focused on the solid-core SCFs, PCFs, and hollow-core PBGFs.

2.1.1 Structures and fabrication

The cross-sectional micrographs of the firstly reported SCF, PCF, and PBGF are demonstrated in Figure 2.1 [7-9]. As shown in Figure 2.1 (a), the idea of introducing air-cladding inside a fiber was firstly proposed and experimentally realized by Kaiser and his colleague as early as 1973 for the porpose of simplifying the fabrication and minimize the loss of fiber [7]. In Kaiser's designe, the solid fiber core(s) is suspened in side the fiber by extremely thin spoke-like membranes. It might be the earliest SCF as well as MOF. However, constrained by fiber fabrication technique at that time, the fiber have non-circular cross-sectional pattern and nonstandard dimention and core position. These weakness limit the application of this fiber. In the nearly twenty years after Kaiser's work, the research on the SCF was rare.

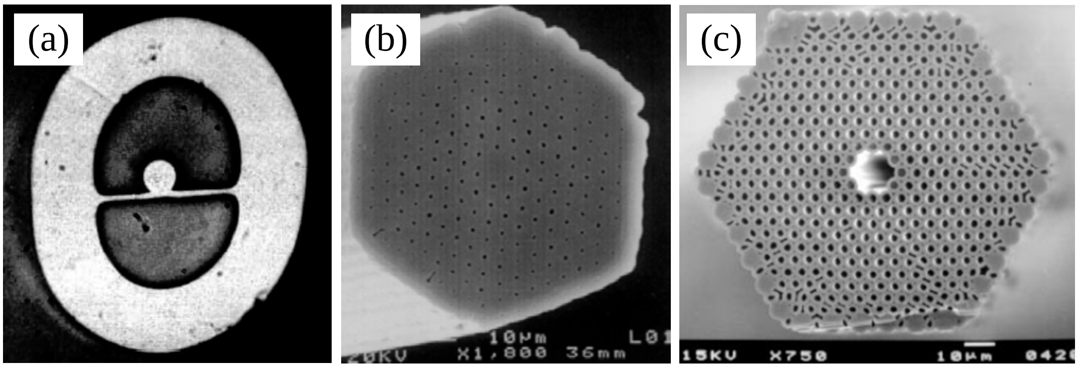

Figure 2.1 Cross-sectional micrographs of the first published SCF (a) [7], PCF (a) [8], and PBGF (b) [9]

At the end of nineteen nineties, the progress of fabrication techniqes and researches on photonic crystal (PC) structure enabled the booming studies on the fibers with complex interior structure such as PCFs and PBGFs. Both the PCF and the PBGF (Figure 2.1 (b) and (c)) have the cladding with two-dimensional (2D) photonic crystal (PC) structure which is constructed by the small air-columns with different size and distribution. The fiber cores of the PCF and PBGF are generated by the purposely introduced structural defects inside the PC structure region, normally at center of fibers. The defects of the PCFs are typically a solid region produced by introducing missing air hole(s) [10]. Differently, the defects of PBGFs are a larger holey region produced by the absence of many air-columns [9]. So, the PCF and the PBGF, respectively, have solid core and hollow core. It worth to mention that the PBGF in this thesis is adopted as the abbreviation of the hollow core PBGF, actually the photonic band gap guidance is possible for solid core fibers as well. [10]

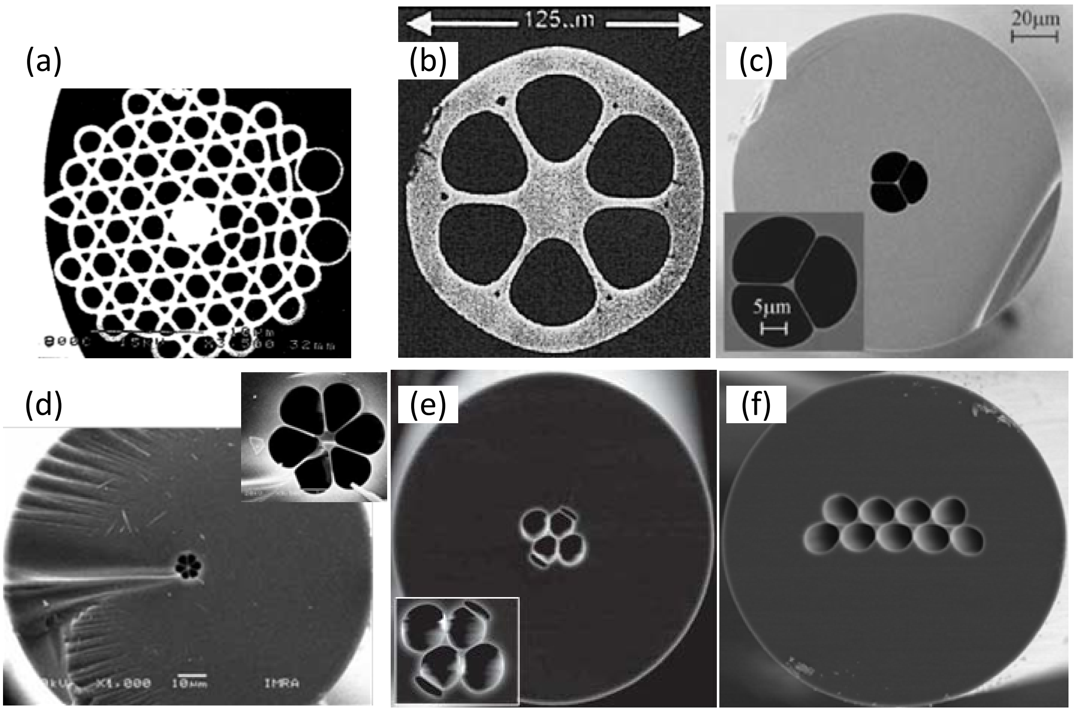

Figure 2.2 Cross-sectional micrographs of some typical suspended core fibers containing (a) periodical cladding [11], (b) six holes [12], (c) three holes [13], (d) six holes and a micro-scale core [14], (e) four holes and two cores [15], (f) nine holes and seven cores [16]

With the development of MOFs, more and more researches have been conducted on the fibers with suspended core(s) structures, i.e. the SCFs, for their potential applications in evanscent filed sensing, fiber nonlinearity, spectroscopy etc. The cross-sectional micrographs of some SCFs reported in recently articles are shown in Figure 2.2. Compare to the antecedent of SCF in Figure 2.1 (a), the recent SCFs have core(s) suspended by more struts, which would equivalent the surface tension in fabrication and guarantee the round symmetrical shape of fiber cross-section.

The SCF in Figure 2.2 (a) has a extraordinary 2D periodical cladding structure which is similar to that of a PCF except the larger size holes. Actually, when transverse dimention of the air-columns in a PCF becomes much larger than the operation wavelengh, the light propagating in the fiber can be effectively confined by only the innermost ring of air-columns [17]. Therefore the SCF of Figure 2.2 (a) can be simplified to the equivalent structure in Figure 2.2 (d). There are many names for the SCFs, for examples, the three holes SCF in Figure 2.2 (c) is sometimes called steering-wheel fiber [18], the SCF in Figure 2.2 (b) is called Grapefruit Fiber [19] etc. To highlight the features, the SCFs in Figure 2.2 are prefixed with hole and core numbers for their name in this dissertation.

Due to the large refractive index (RI) differences between core and cladding, the dimention of SCFs is typically smaller than 3 microns to minizied the supporting modes of fibers. To achieve the single mode (SM) operation, sub-micro sized core is required. However, the extremely small core size brings large insertion loss in splicing to other fibers. An alternative methode for SM operation is to dope the fiber core. Figure 2.2 (b) demonstrates a SCF with ~8 μm core region doped with germanium (Ge). The principle of this fiber is similar to conventional SM fiber (SMF). Strictly speaking, part of the cladding of this fiber is also suspended. However, nearly all the energy of the guided light exists in the solid region. This feature greatly limit application of the fiber in light-matter interaction.

Figure 2.2 (c)-(f) are the micrographs of four single material SCFs with different structures. Compare to the six holes structure, the three holes structure is preferred in fabricating SCFs with small core-size [20]. Figure 2.2 (e) and (f) are, respectively, the twin-core SCF and the multi-core SCF which can be applied in buiding in-fiber interfererometers [15, 16].

The SCFs can be consider as one or few small solid silica rod(s) suspended in the air, which is similar to the structure of the the conventional Micro- or Nano fibers (MNF) fabricated by tapering a SMF in many aspects, such as large evanscent field, air cladding, and high nonlinearity. However the MNFs are fragile, which makes them difficult to handle, and fully exposed to the conventional optics laboratory environment would lead to contamination and very fast degradation [21]. The problem does not exist in SCFs due to the existance of jacket tube and struts. Furthermore, the cells in SCF provide the isolated spaces which can reach part of the core-surface. Nevertheless, the MNFs is still superior to the SCFs for their low loss connection to the SMFs.

Although the product of SCFs is rare in market, the PCFs and PBGFs have been commercially available for years. Figure 2.3 (a) and (b), respectively, are the cross-sectional micrographs of the LMA-10 PCF and the HC-1550 PBGF from NKT Co., which have good compatibility to current SMF system.

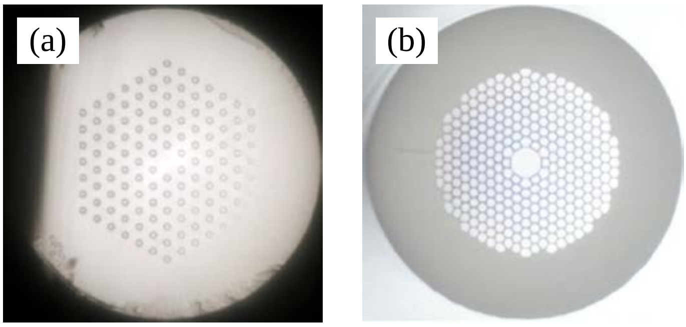

Figure 2.3 Cross-sectional micrographs of the LMA-10 PCF (a), and the HC-1550 PBGF (b)

The PCFs of the NKT LMA series have similar hexagonal holes distribution, but with different hole diameter d_h and pitch Λ (center-center spacing between holes). To facilitate the comparison, the structure parameters of SMF (corning SMF-28), PCFs (NKT LMA-10 & ESM-12) and PBGF (NKT HC-1550) are listed in Table

2.1. The LMA-10 and ESM-12 are the two PCF models used in my study. Compared with the ESM-12, which is specially designed for low-loss connection to SMF, the LMA-10 have a smaller solid core and lower attenuation in low wavelength region, although the connection loss between LMA-10 and SMF is slightly higher than that between ESM-12 and SMF.

Table 2.1 Structural parameters of conventional SMF Corning SMF-28, PBGF NKT HC-1550, and some PCFs (NKT LMA-10 and ESM-12) [22-24]

Fiber Name	Diameter			Pitch Λ	d_h/Λ
	Core d	Holes d_h	Clading D		
	μm	μm	μm	μm	
SMF-28	8.2	-	125 ±0.7	-	-
HC-1550	11 ±1	3.77	121 ±2	3.88	~ 97 %
LMA-10	10.1 ±0.5	3.38	125 ±2	7.2	~ 48 %
ESM-12	12 ±0.5	3.5	125 ±2	7.7	~ 46%

Stack-and-draw technique is widely used in fabricating PCFs [25], PBGFs [9] and SCFs [3]. The schematic of the multi-step fabrication process is provided in Figure 2.4. At first, large silica tubes and rods are drawn down to capillaries and small rods with diameter 1 - 2 mm using the drawing tower. Then the silica capillaries and small rods are manually stacked to an array with designed patterns. Defects are introduced to the pattern by replacing or removing elements in the center, for example, one capillary in the center is replaced by rod in fabricating PCFs and SCFs, several capillaries in the center removed in fabricating PBGFs. In the next step the air space between capillaries and rods is removed by drawing under the condition of high temperature and high vacuum. A preform generated in last step is inset in a cover tube and continue to draw down to the fiber.

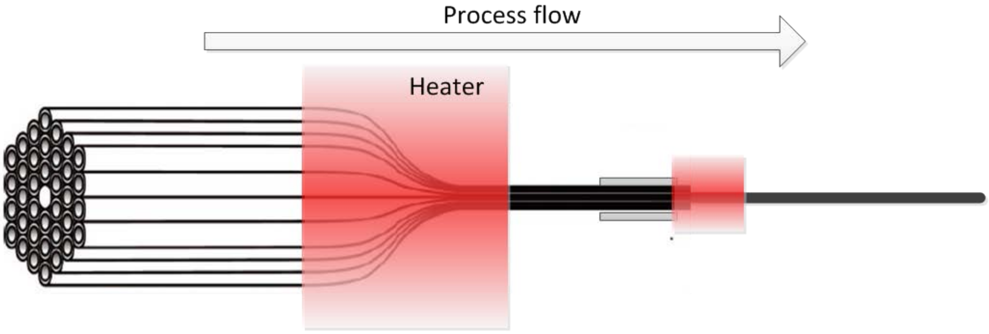

Figure 2.4 Schematic of the stack and draw technique [25]

Extrusion technique is another frequently used technique in MOFs fabrication, especially in SCFs fabrication. One distinct advantage of the technique is that non-cylindrical air-columns can be produced [26]. There are three steps in the technique. Firstly, as illustrated in Figure 2.5, the structured preform and jacket tube are extruded through a die structure by pushing the optical materials in bulk billet. The billet is heated to a temperature where the material is sufficiently soft. Secondly, the preform is drawn down to a 'cane' of about 1 mm diameter with a fiber drawing tower, and then the cane is inserted into a suitable jacket tube. Finally, the assembly of cane and tube is drawn down to the fiber [27].

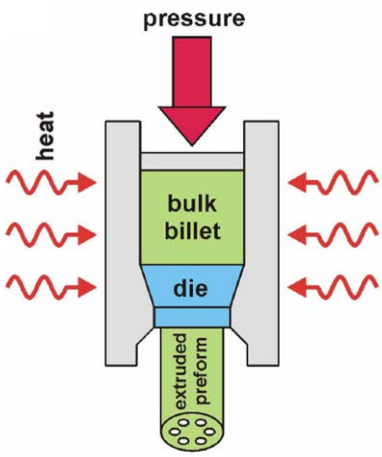

Figure 2.5 Schematic of the extrusion process [26]

There are also some other techniques can be applied in MOF fabrication, such as sol-gel casting [28] and ultrasonic preform drilling [29]. All of the aforementioned techniques exhibit difference advantages and tradeoffs in the aspects of fabrication convenience, cost, design flexibility, material, precision etc.

2.1.2 Guidance mechanisms and properties

The guidance mechanism of a MOF is greatly dependent on its interior structures. The PCFs, PBGFs, and SCFs which are three major subclass of MOFs work on three distinct guidance mechanisms, that is, the modified total internal reflection (TIR), the photonic band gap (PBG) guidance, and the TIR respectively.

The modified TIR mechanism and the TIR mechanism are intrinsic index guiding, which happens when the condition $n_{co} > n_{cl}$ is satisfied. The n_{co} is RI of fiber core, and the n_{cl} represents (effective) RI of fiber cladding. The conventional SMFs can be also cataloged in index guiding fiber based on TIR mechanism. Nevertheless, different to SCFs, the SMFs have a much lower RI difference $\Delta = (n_{co} - n_{cl}) / n_{cl}$ ~0.4% between core and cladding to guarantee single mode operation. The mechanism of PBG guidance allows guiding light in the fibers with negative core-cladding RI differences, that is, $n_{co} < n_{cl}$.

These mechanisms can be explained with the aid of propagation diagrams in Figure 2.6. The horizontal axis of the figures is the normalized propagation constant '$\beta\Lambda$' which represents axial wave-vector component 'β' multiplies inter-hole spacing 'Λ' of a PCFs or PBGFs (for step index fiber $\Lambda=1$). The vertical axis is the normalized frequency $\omega\Lambda/c= k\Lambda$, where ω, c, k represent, respectively, the angular frequency, speed, and wave-vector of a light in free space. In the black regions, propagation of light is forbidden.

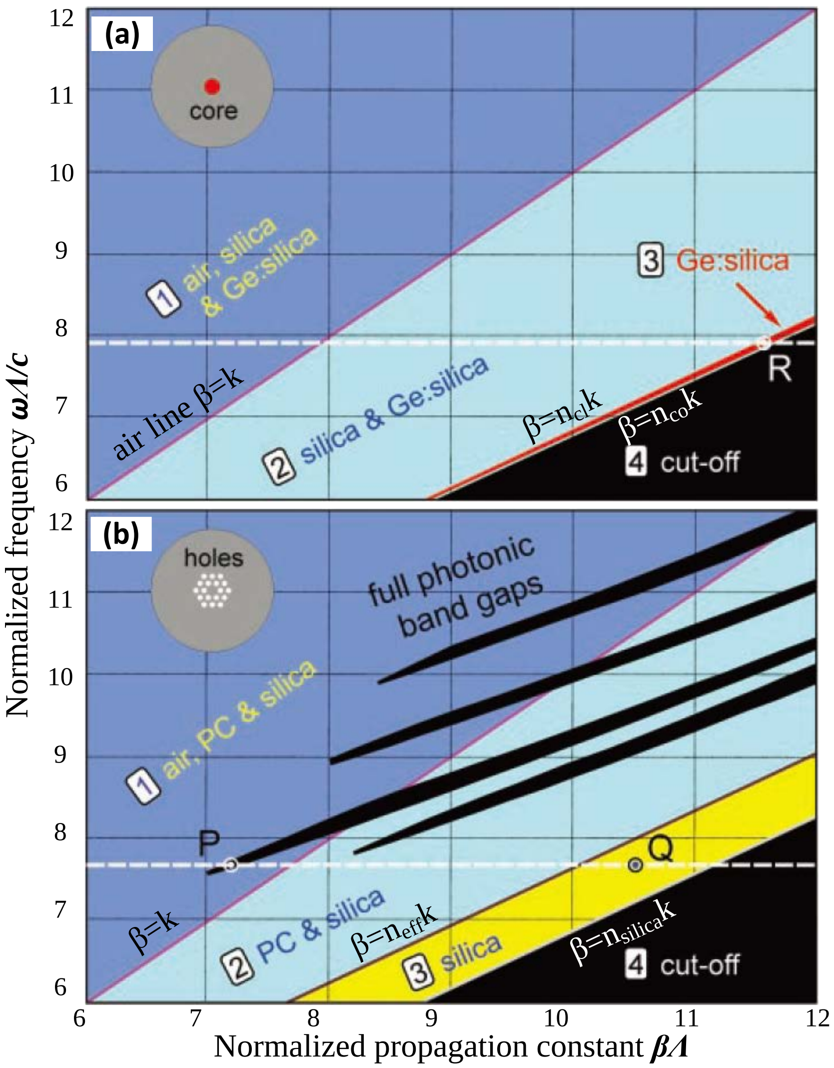

Figure 2.6 Propagation diagrams for (a) SMFs, (b) PCFs and PBGFs [25]

Figure 2.6(a) depicts the propagation condition of SMFs based on TIR guidance mechanism. The propagable region of the fibers is divided into three parts according to RI of the materials under consideration, which are air, cladding material, and core material. Propagation is supported in the core when β located in region$\boxed{3}$ where $kn_{co} > \beta > kn_{cl}$. The region $\boxed{3}$ is narrow because of lower RI difference between core and cladding. For the SCFs, only the silica core and air cladding are considered. The propagation condition is $kn_{silica} > \beta > k$, which corresponding to a region equal to $\boxed{2} + \boxed{3}$ in Figure 2.6(a).

Figure 2.6(b) depicts the propagation condition of PCFs and PBGFs. By introducing PC structure in fiber, the silica region in figure (b) is divided to two parts. A new region $\boxed{2}$ is generated. The PC region is smaller than silica region. This may be understood by the effective RI of PC region is decreased due to the existence of air-columns. Consequently, for a fixed k value, some β values are evanescent in PC structure, and hence can only propagate in the silica (core) region. The effective cladding index '$n_{(cl),eff}$' of PCF can be defined as $n_{eff} = \beta_{FSM}/k$, where β_{FSM} represents the propagation constant of fundamental space-filling mode (FSM) which is defined as the fundamental mode supported in an infinite PC cladding [30]. The propagation condition can be summarized as $kn_{silica} > \beta > kn_{eff}$, which is similar to the TIR mechanism descripted in last paragraph. Different to the TIR of SMFs and SCFs, the RI differences of PCFs are based on the cladding structures rather than materials. So the guidance mechanism of PCFs is also call modified TIR.

By adjusting the pitch and air-filling fraction $d_{h/}\Lambda$, 2-D Photonic Band Gaps (PBG) can be formed in the fiber. In the propagation diagram, extra cutoff regions (the black 'fingers') are generated, and extend to the $\beta < k$ region. Therefore, for a fiber with PBG structure cladding, the light with β located in cutoff region will be confined in the core region, no matter how small the core RI is. This property makes it possible to build fibers with hollow core, i.e. PBGFs [25].

The PCFs, PBGFs and SCFs contain many more unique properties than conventional fibers. The guided modes in standard fibers are determined by the normalized frequency 'V', which depends on the core radius 'r', wavelength 'λ' and Numerical Aperture NA:

$$V = k \cdot r \cdot NA = k \cdot r \cdot (n_{co}^2 - n_{cl}^2)^{1/2} \tag{2.1}$$

The propagation constant β of the possible modes in fiber can be calculated by solving the dispersion equations [31]. The results are presented in Figure 2.7. The supported modes are decreased by reducing the V value. The fiber become single mode when $V < 2.405$.

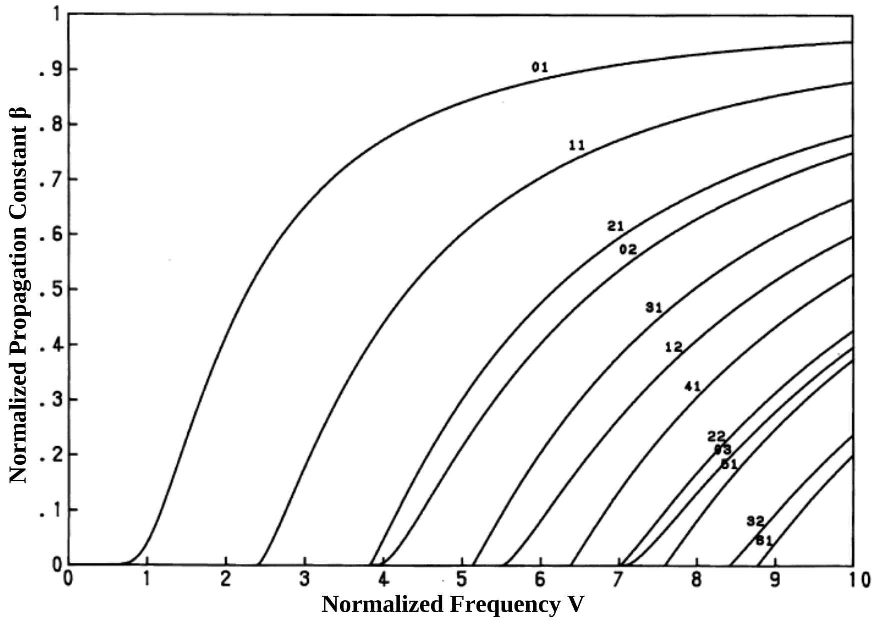

Figure 2.7 Dispersion diagram of LP modes in circular step-index fiber [31]

Similar to the step-index fibers, an effective normalized frequency 'V_{eff}' can be defined by applying the effective RI of cladding region [30]:

$$V_{eff} = k \cdot \Lambda \cdot NA = k \cdot \Lambda \cdot (n_{co}^2 - n_{eff}^2)^{1/2} \tag{2.2}$$

The inter-hole spacing Λ approximately equal to radius of the PCF when holes are not too large [30]. As illustrated in Figure 2.8, there is a critical d/Λ value, below which the V_{eff} of fiber cannot reach the cutoff value of single mode operation. That is, by optimizing the d/Λ value, it is possible to fabricate the PCF in which the second mode is never guided at all frequencies. Numerical modeling shows that the critical relative hole size is ~0.43. This is the ESM property of PCFs [32].

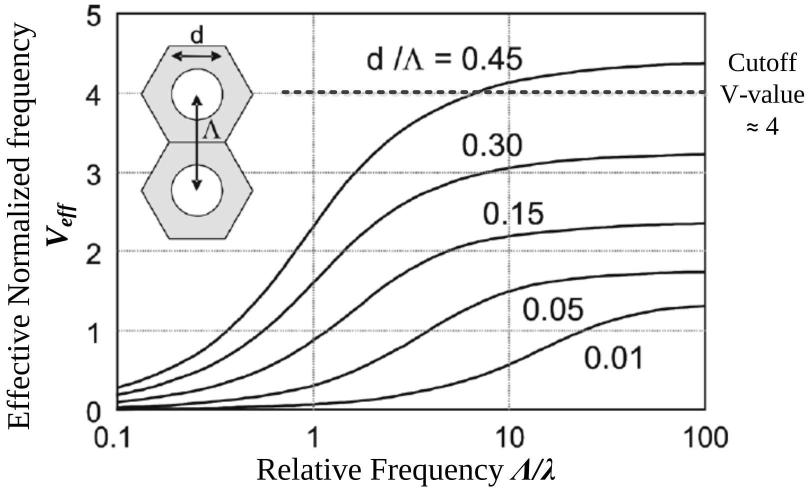

Figure 2.8 The variation of V_{eff} in PCF with Λ/λ for different d/Λ[32]; The dashed line marks the cutoff V-value

Since the operation of ESM PCF is independent to the absolute size of structure, a larger-mode-area (LMA) single-mode PCF can be fabricated. As early as 1998, a single-mode PCF with ~22 μm core diameter at 458 nm was reported [33]. The LMA property allows higher power can be carried in PCFs before the onset of intensity related nonlinearities or damage.

The core of SCFs is isolated from the other part of fiber by extremely thin struts. The large RI difference between core and cladding makes SCFs commonly possess high numerical aperture, and the propagating modes are strongly confined in the solid core region. The cores of SCFs are always made very small to enlarge the evanescent field in holes, and to enhance the non-linearity effect. [14, 27]

The guided mode of PBGFs can be classified as the core mode with similar profile with conversion fiber, and the surface mode with most energy located around the interface between core and cladding [2]. Single mode propagation PBGF can be realized by reducing the size of hollow core. (Figure 2.9)

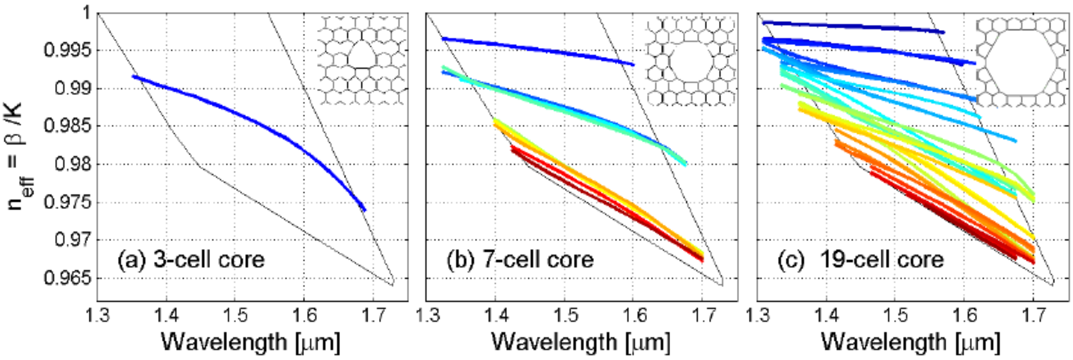

Figure 2.9 Calculated effective RI of PBGFs with 3-, 7-, and 19 cell core [34]

Some other properties of PCFs, PBGFs and SCFs are highly dependent on the structure of fibers. For examples, the zero dispersion point, mode field diameter, non-linearity, birefringence of PCFs and SCFs can be designed in a large region by varying the relative hole-size d/Λ, core shape and size. [14, 25, 34] In conclusion, a plenty of new properties have been endued to optical fibers by introduce various micro-structures. The MOFs have greatly extended the possibility of fibers.

2.2 Fiber Tapering Techniques

Fiber tapering is a powerful post-process technique widely used in fabricating optical fiber micro- or nano-wires with outstanding optical and mechanical properties, such as large evanescent fields, high nonlinearity, perfect surface smoothness, and low loss interconnection with standard fibers. The tapered fiber can be applied in making many all-fiber devices, such as spectral filters, couplers and nonlinear optical elements [35, 36].

In this section, a review of current fiber tapering techniques is presented, with particular emphasis on the application of fiber tapering techniques on MOFs post-process.

2.2.1 Principles

Three major methods are widely used in fiber tapering: 1. The flame brushing technique; 2. The modified flame brushing techniques, in which the flame is replaced by other heat sources such as CO_2 laser [37], microheater [38]; 3. The sapphire rod assisted tapering [39]. The basic principle for all these fiber tapering techniques could be concluded as "Heat and pull": a fiber is locally heated and then axially stretched. The fiber in the hot region would experience a diameter decrease due to the mass and volume conservation. Two transitions in the fiber are formed at the edges of the hot region. Basic setups for fiber tapering are provided by Figure 2.10.

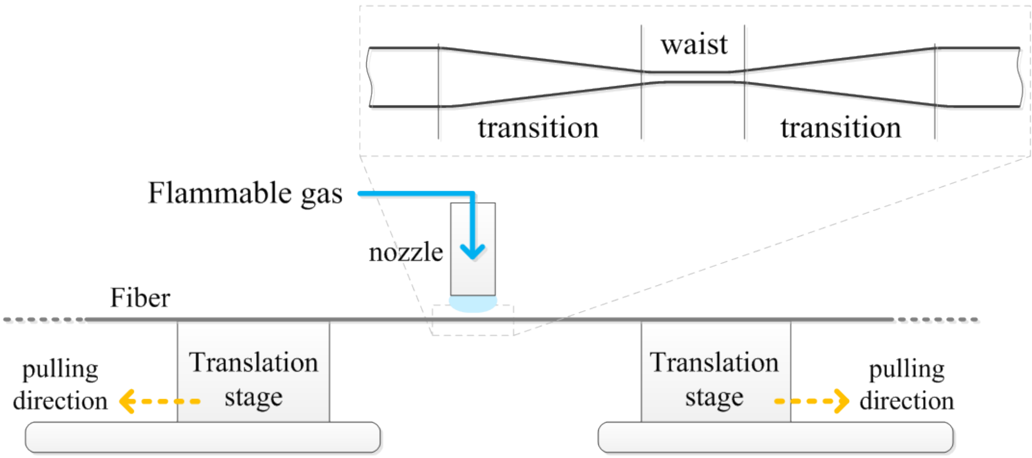

Figure 2.10 The basic setup of a brushing flame tapering system

Many heat sources are feasible for fiber taper applications. Such as CO_2 lasers, flammable gas (Hydrogen, butane and oxybutane mixture et al.). Both of them can be used to fabricate fiber tapers with low loss (<0.1 dB/mm) and submicron waist dimensions. The fuel (flammable gas) and the oxidizer (oxygen in air) can be mixed before or after the combustion process. Although premix flame is superior to non-premix ones in the aspect of controlling the combustion by setting the fuel ratio, the non-premix flames are mostly used in applications for safety considerations [40]. Figure 2.11 (a) indicates that the laminar gas flow of the flame becomes turbulence, and the flow-type transition interface becomes closer to nozzle exit with higher fuel flow rate. In the fiber tapering process, the laminar flow region is preferred to minimize the disturbance to the tapered fiber with micron /sub-micron transverse scale. Therefore, the flow rate of the fuel should not be too high, and the fiber should be located near to the nozzle.

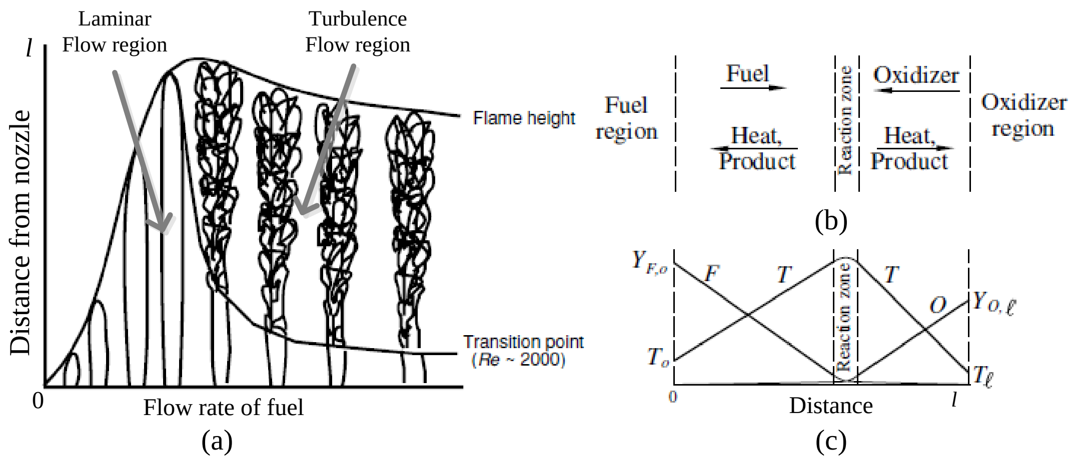

Figure 2.11 Physical configuration of a typical pure diffusional non-premixed jet flame (a) The laminar flow to turbulence flow transition [40], p189; (b) Flow of reactants and heat. (c) Temperature and concentration profiles [41], p211

Figure 2.11 (b) shows the flow of reactants flow, heat and production of a typical combustion process. The fuel and oxidizer are transported toward each other through convective motion of system and the diffusion. In the procedure, the reactants are heated and eventually mixed within the reaction zone. Figure 2.11 (c) shows the one-dimensional profiles of temperature ‘*T*’ and mass fraction ‘Y’ of fuel ‘F’ and oxidizer ‘O’ from flame center towards oxidizer. The reaction zone with the highest temperature of flame is a suitable place for fiber tapering.

In fiber tapering, the processing parameters significantly influence the final taper morphology, which determines both optical and mechanical properties. As illustrated in Figure 2.12 (b), a fiber taper typically includes two transitions and a waist. To correlate process parameters and taper shape, two fundamental equations drawn from the "volume law" (conservation of mass) and the "distance law" (conservation of length) can be used: [35]

$$dr_w / dx = -r_w / 2L(x) \tag{2.3}$$

$$2z_0 + L(x) = x + L_0 \tag{2.4}$$

where r_w is the radius of the waist. As in Figure 2.12, x is the total extension of fiber at time t. L_0 is the length of hot-zone (the region fiber are heated) at the beginning of process. $L(x)$ is the length of taper waist which is a function of fiber extension is x. z_0 is the width of transition region.

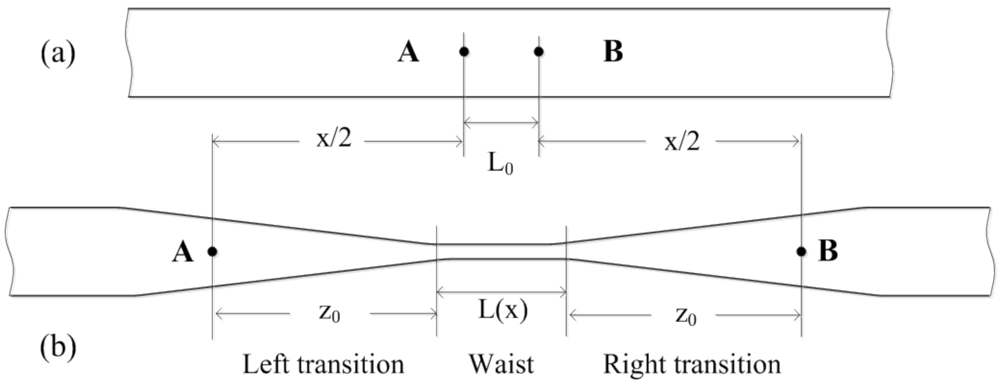

Figure 2.12 (a) The initial status of optical fiber; (b) The fiber in tapering at the moment "t"

The model can be generalized by allowing the variation of hot-zone:

$$L(x) = L_0 + \alpha x \tag{2.5}$$

In equation(2.5), the hot-zone length L is linearly related to fiber extension x with the coefficient α, which determine the contour of the taper transition region z.

From equation (2.3)(2.4)(2.5), the complete shape of fiber can be found:

$$r_w(x) = r_0 e^{-x/2L_0} \tag{2.6}$$

$$r(z) = r_0 \left[1 + \frac{2\alpha z}{(1-\alpha)L_0} \right]^{-1/2\alpha} \tag{2.7}$$

Equation (2.7) predicts the possibility of fabricating fiber taper with linear transition. As Figure 2.13 (a) show, When $\alpha = -0.5$ and $r(z) = r_0\left[1 + 2z/3L_0\right]$, the radius of transition region changes with z linearly. Figure 2.13 (b) demonstrates an experimental profile of the linear-transition taper fabricated with brushing flames. The profiles of most taper transitions are non-linear.

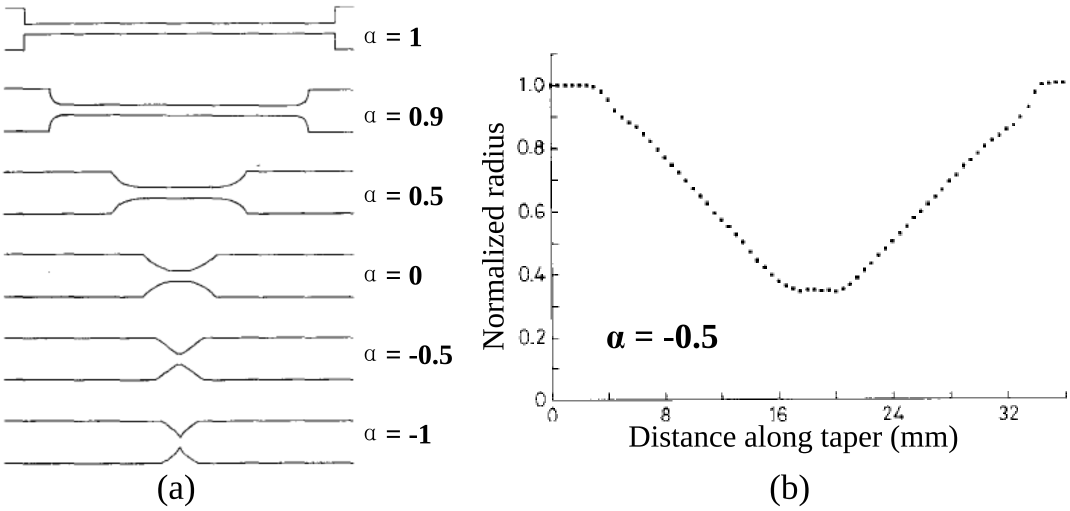

Figure 2.13 (a) The contours of the taper transition region with different α values [35]; (b) experiment result of the taper with linear transition region [42]

The brushing flame technique with constant scanning range is usually used in the practical tapering process for simple control of hot zone L(x) as elongation proceeds. The process is depicted in Figure 2.14. When the nozzle's scanning speed is larger than the speed of fiber elongation d*x*/d*t*, the length of hot-zone is approximately equal to travelling distance of nozzle ($L(x) = L_0$). The transition is always exponential in shape corresponding to the one with α = 0 in Figure 2.13 (a). The shape can be described by [42]:

$$r(z) = r_0 \exp[-z/L_0] \tag{2.8}$$

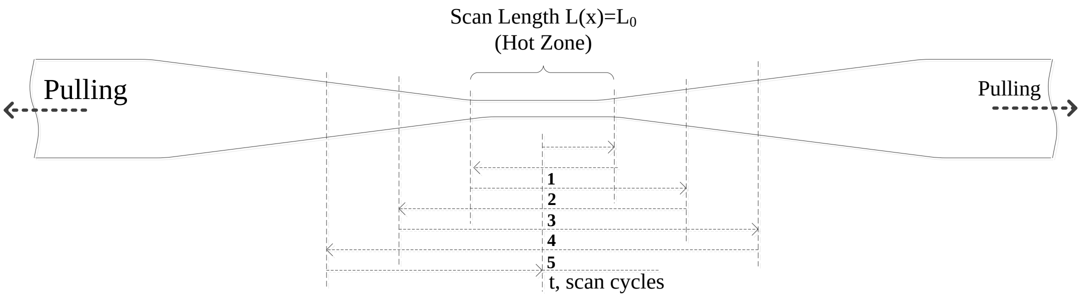

Figure 2.14 The Brush-flame tapering with a fixed scan length L_0

Taper techniques for MOFs

The conventional fiber tapering technique can also be used on MOFs with similar process but different parameters. The technique is effective in locally modifying the properties of the MOFs. Slight changes on the relative hole-size d/Λ of MOF will greatly influence the properties of the fibers.

Due to the surface tension of the softened silica, hole-collapsing always happens when tapering MOFs. The collapses always introduce large insertion loss to the fiber due to disappearance of transvers confinement. Tow method can effectively avoid the problem: pressure the air-columns and pulling MOFs with a higher speed.

With pressured air-columns in MOF, whether the hole in MOFs shrink or expand depended on the pressure different at the interface of silica and gas. The equivalent pressure P_s of silica due to the surface tension γ at the interface can be expressed by applying Young–Laplace equation on the surface:

$$P_s = \gamma\left(\frac{1}{R_x} + \frac{1}{R_y}\right) = \frac{2\gamma}{d} \tag{2.9}$$

where R_x, R_y are the curvature radius of two orthogonal curves on the surface. For the circular air-columns in MOF, $R_x = \infty$, $R_y = d/2$. d is the diameter of air-column. Given $\gamma \approx 0.3\ J/m^2$ for fused silica at the temperature around the softening point of 1700°C [43], equation (2.9) becomes:

$$P_s\ (Bar) = 6 / d\ (\mu m) \tag{2.10}$$

The equivalent pressure P_s is about 1.7 Bar for NKT ESM-12 with the hole-diameter of 3.5 μm (Table 2.1).

The collapse rate of the holes in MOF would also be reduced by increasing the axial material flow which is mainly governed by the pulling speed of tapering machine [44]. Micrographs in Figure 2.15 show the cross-section of two PCF tapers at waist region. The tapers are fabricated from the same PCF mode, and to the similar waist dimension, but with different pulling speed. The pulling speed of the taper in figure (a) is about two times faster than that of (b). The collapsing of holey region is more serious for the fiber tapered with slower pulling speed.

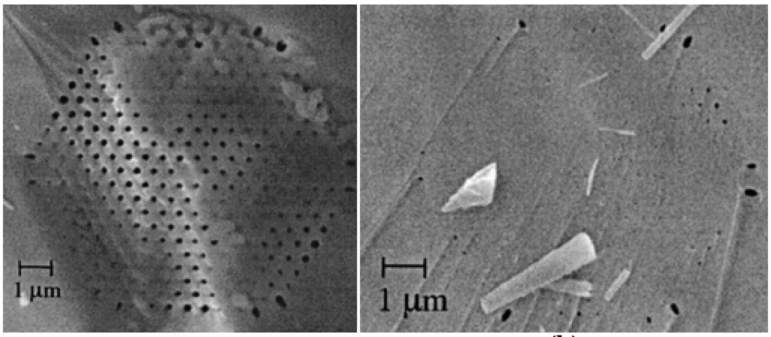

(a) **(b)**

Figure 2.15 The cross-section photos of PCF tapers fabricated with same fiber type but different pulling speed; (a) Taper with OD = 44.5 μm, Λ ≈ 510 nm, d/Λ ≈ 0.35 with pulling speed 5mm/min; (b) Taper with OD = 43.2 μm; Λ ≈ 430 nm, d/Λ ≈ 0.07–0.14 with pulling speed 2.2 mm/min [44]

Many other process parameters also influence the collapsing rate of MFOs, for example, flame temperature, scanning speed of nozzle, etc. Since the viscosity of silica changes rapidly with the temperature close to the softening point of ~1700 °C, tapering with a “cold” flame can decrease the mobility of silica, and reduce the collapsing rate of air-column in MOFs. [43, 45]

2.2.2 Adiabatic criteria

The insertion loss of an optical fiber taper device is associated with the taper angle of transitions. The power loss from the fundamental core mode happens due to the departure of translational invariance in the fiber. This power is coupled to the lossy higher order modes in the fiber.

Intuitively, the coupling of the propagating core mode with the lossy higher order mode would be weak with transient angle. However, the taper angle cannot be arbitrarily small in practical tapering. There is always a limit on the taper angle for low loss transition. A taper is called adiabatic taper if the local angle along the transition is small enough to ensure that negligible power is coupled out from the propagating core mode [46].

The taper transition can be divided into small regions (slices) with identical radius along the propagation direction z. Each small region supports its own "local modes" with propagation constants $\beta_j(z)$. This new model would be very accurate if the length of the section δz is much smaller than the length scale of the taper transition [47]. When light propagate through different small regions, more or less, there are some light power coupling from one local mode to another one. However, the coupling of local modes is negligible if the fiber transition is sufficiently flattened.

Figure 2.16 shows some definitions of a taper transition of fiber core. A widely used length-scale adiabatic criterion proposes that the coupling of local modes m and n is negligible if the local taper length z_l is much larger than the coupling length of the two modes.

$$\tan\Omega = \left|\frac{dr}{dz}\right| \le \frac{r(\beta_m - \beta_n)}{2\pi} \tag{2.11}$$

where Ω is local taper angle, r is the local core radius, β_m, β_n are the propagation constant of local mode m and n respectively.

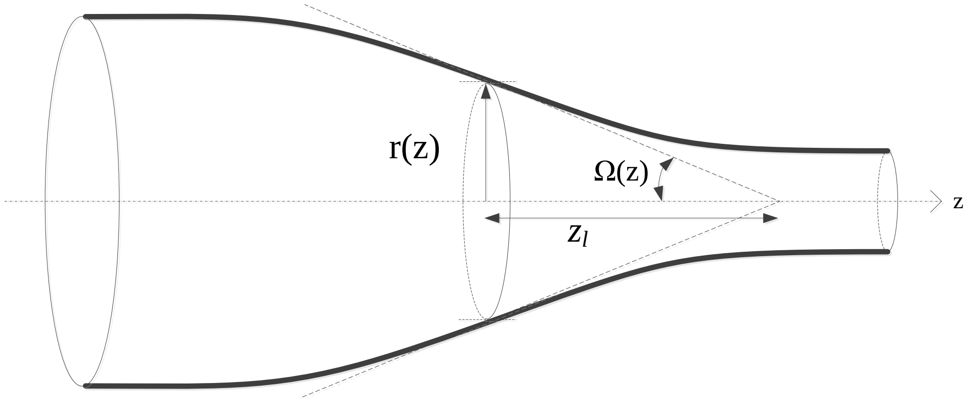

Figure 2.16 Diagram of tapered fiber core transition

The adiabatic criteria can be used for step index fiber and MOFs as well. [46, 48] In practice a measurement of loss and/or purity of the mode at the fiber output can indicate whether a transition is adiabatic or not.

2.2.3 Holes inflation of MOFs

In tapered all-solid fibers, the structure of fiber deforms proportionally during the process. However, extra degree of freedom can be introduced into the process for MOFs by changing the pressure in the air-column running along the length of MOFs. Micrographs in Figure 2.17 are the cross-section results of the PCF tapered at different pressure from 6 to 10Bar. The size of air-columns in PCF is greatly increased, while the core dimension decreases significantly.

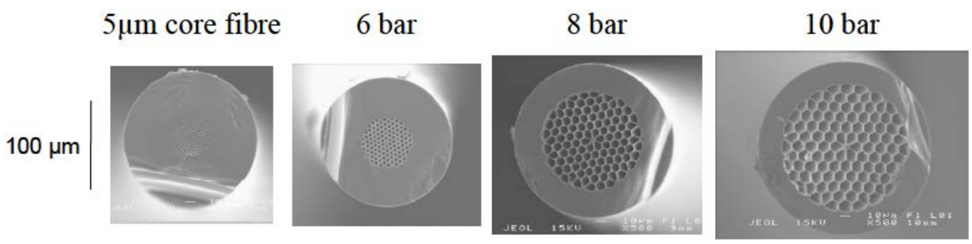

Figure 2.17 SEMs of the cross-section of ESM PCF processed with the same tapering condition but at different pressures from 6 to 10 bar [45]

The inflation and tapering process was firstly reported by Wadsworth, et al to produce small core MOFs with potential applications in super-continuum spectra generation. As illustrated in Figure 2.18, the PCF is locally inflated to expand the size of all air-columns, and then drawn down to shrink the size of core.

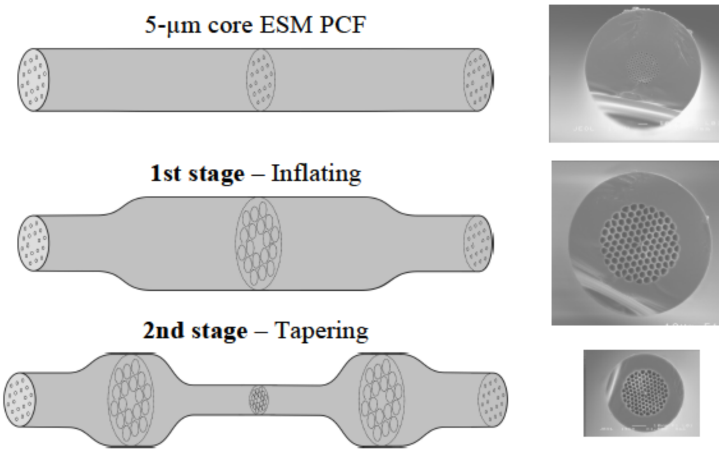

Figure 2.18 The stages of inflation and tapering process for producing PCF with small core [45]

The parameters for the tapering MOFs with hole-inflation are actually the opposite of those MOFs tapering without pressure. To prevent the collapse of air-columns under surface tension when the MOFs are tapered without pressure, a ‘fast and cold’ process is always adopted. That is, tapering the fiber with a relatively low temperature flame to minimize the rate of collapse, and stretching as quickly as possible to minimize the processing time. In contrast, for hole-inflation tapering, the ‘slow and hot’ process uses a relatively hot flame for rapid hole-inflation and stretching slowly to increase the processing time. The inflation of the holes can be controlled by using different nitrogen pressures. When a section of fiber with inflated air-columns is ready, the fiber can be tapered again in a conventional ‘fast and cold’ process to reduce the core diameter with little changing in air filling fraction.

Selective Inflation of MOF Holes

By combining the techniques of fiber tapering, holes selection and inflation, more complicated holes and core patterns can be realized in MOFs. [45, 49, 50]. As illustrated in Figure 2.19 (a), one side of a MOF is selectively plugged by the method of selective filling or selective opening. The other side of the fiber is totally plugged. Then high gas pressure is applied to the selectively processed end, obviously, the pressure of the up-plugged air-columns will vary with pressure load while the other columns remain unchanged. By conducting the "slow and hot" tapering on the MOFs, the pressured air-columns inflate on heating, while the plugged holes collapse to adjacent structures. Two gradual transitions are formed along the fiber.

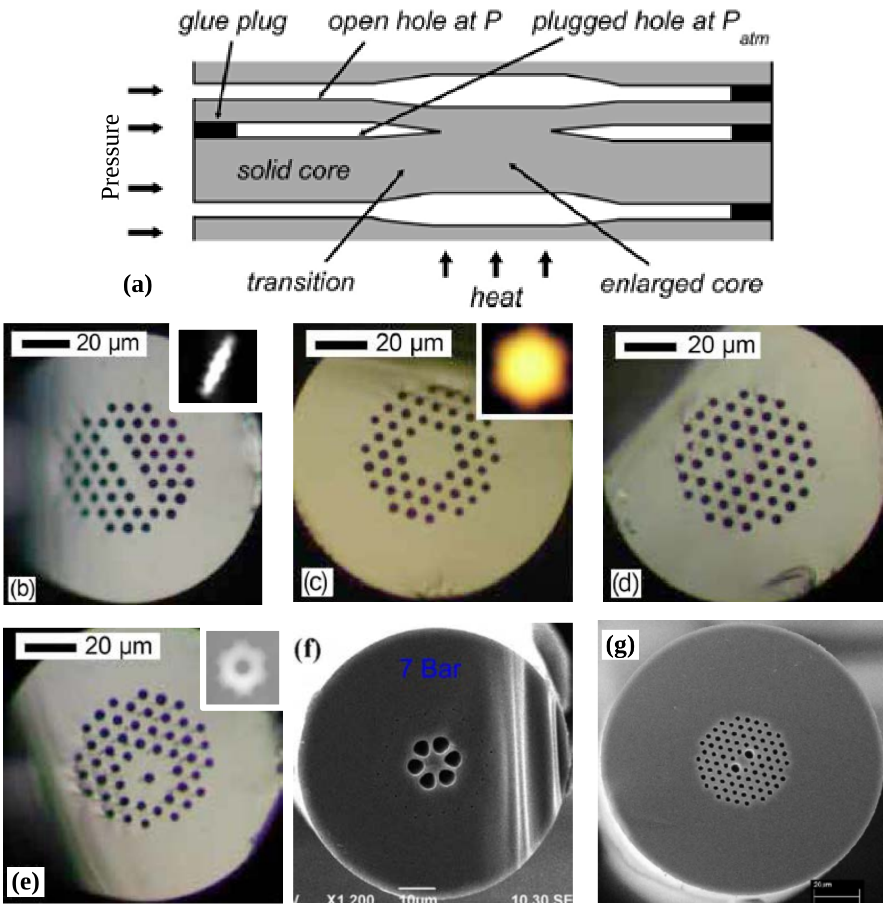

Figure 2.19 (a) Schematic for the selective holes inflation technique; (b-g) The transverse cross-section micrographs of processed MOFs [50, 51]

The air-column structure can be modified with high freedom by applying different pressures to the different column sets. This method can locally change the structure of MOFs and generate fluent transitions between the processed region and intact region.

2.3 Femtosecond Laser Micromachining

Fs laser assisted machining is another technique widely used in post-processing optical fibers. The technique possesses many distinct advantages, such as non-contact, high speed, quality in operation, and less contamination.

2.3.1 Basics of fs laser

The first fs-level pulse laser based on passive mode-locking of organic dye material was demonstrated by Fork et al. from Bell Tel. Lab in 1981 [52]. However, the complicated structure and large volume of the laser limits its practical application.

Until later 1980s, the emergence of solid gain materials such as Titanium-Al_2O_3 (Ti:sapphire) crystal greatly promoted of ultra-short laser technique in near-infrared spectral region. The broad gain bandwidth of the crystal especially fit for ultra-short pulses generation and amplification. Based on the self-focusing effect occurring in the Ti:sapphire medium, the Kerr lens mode locking (KLM) techniques can realize intra-cavity mode locking with few elements. However, the KLM laser does not spontaneously start and require a critical cavity alignment. The application of semiconductor saturable absorber mirrors (SESAMs) can solve the self-starting problem of KLM technique, and enable KLM lasers to work stably for long time. [53, 54]

To generate a high peak power, the chirped pulse amplification (CPA) technique is applied in most fs lasers. As illustrated in Figure 2.20, the fs pulse from the ultra-short pulse mode locked laser oscillator is stretched to about ns pulses and recompressed back to the pulse with fs duration after the amplification process. The stretch and compression of the pulses can be achieved by diffraction gratings, fiber gratings or pairs of prisms arrangement. The CPA technique separates the ultra-short pulse generation process from the amplification process to avoid very high peak powers in the laser amplification process [55, 56]. By using multi-stage hybrid CPA technique, a peta-watt (PW) peak power fs laser can be built. [57]

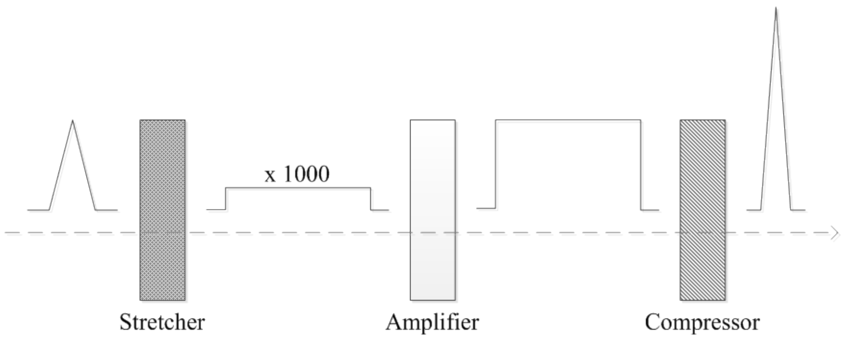

Figure 2.20 Schematic of the chirped pulse amplification (CPA) technique

Many new features will arise when the pulse duration of laser decreases to a level of fs. The thermal diffusion and shock wave emission outside the focal region is minimized, which greatly increases the precision of the method. Modifying the structure in dimension below the diffraction limit (sub-micron) is possible by enabling the power of peak region of laser pulse exceed the material damage threshold [58]. In addition, the ultra-short pulse duration enable the pulse energy of fs laser can reach ultra-high peak power beyond the material ablation threshold with relatively low energy assumption. From a practical point of view, fs lasers are capable to machining all materials and the peak power is currently constrained by the damage threshold of the laser chain components [59].

Furthermore, fs laser micromachining can realize elaborate 3D structure inside transparent materials while leaving the surface unaffected. In transparent material, there is nearly no linear absorption to fs laser beams. However, around focus point of beam where the intensity of fs laser beam is greatly increased, the nonlinear absorption in material is enhanced, more and more electrons in material are excited to higher energy level. The density of excited electrons continue to increase by avalanche ionization until local plasma generated, the remaining pulse energy would be absorbed by the plasma. The material undergoes a local phase (RI) or structural modification after the whole procedure. The fs laser 3D micromachining can reach a volumes as small as 0.008 μm^3 [60].

Based on these unique advantages, the fs laser has found uniquely applied in optical storage [60], microelectronics [61], microstructure photonic devices and optical waveguide fabrications [62-66], biomedical applications [67] etc.

2.3.2 Fs laser micromachining system

A typical fs laser micromachining system is given in Figure 2.21. fs laser is core of the system. Some ancillary instruments for adjusting beam spatial property, pulse energy, and sample position are also inevitable. There are four main parts in an fs laser machining system: (1) A two stages fs laser system. (2) Optical elements in the optical path to remove the aberrations of laser beam and continuously adjust the pulse energy. (3) A microscope system which focus the fs laser pulse. (4) A sample platform with accurate 3D motion controlling.

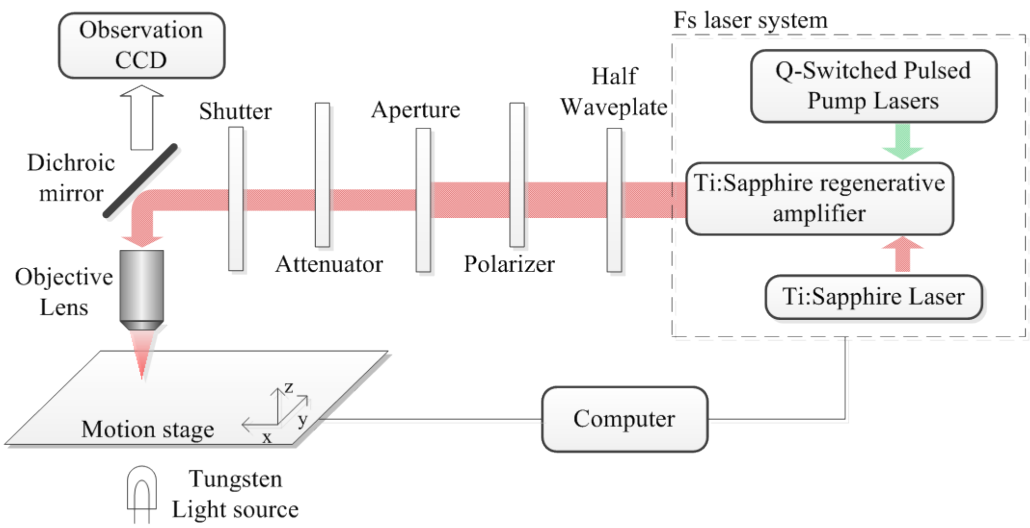

Figure 2.21 Schematic of fs laser micro-machining system

The fs laser system used in our experiments is the Spectra-Physics Ltd.'s Ti: Sapphire laser system which contains a Ti: Sapphire oscillator (Mai Tai^{TM}), a Ti: Sapphire ultrafast amplifier (Spitefire^{TM} Pro), and a Q-Switched 527 nm pump lasers (Empower^{TM}). The output from the fs laser system is a Gaussian shape, linear polarized light with central wavelength at 800nm, pulse duration of 120 fs, repetition rate of 1 kHz, beam diameter ~3mm and maximum single pulse energy of ~1 mJ.

The combination of the half waveplate and the polarizer (Glan prism) can change the transmitted pulse energy continuously from 1 μJ to 1 mJ by adjusting the relative angle between the optical axes of them. The small aperture trim the laser beam spatially to ensures a good beam quality. The attenuator and shutter can provide a fast reducing the pulse energy by fixed ratio (combination of 4x, 8x, and16x) and block the light beam. The dichroic mirror reflects the near infrared fs laser to the lens, and is transparent to the visible light. Therefore, the image around the focal plane of the lens can be recorded by the charge-coupled device (CCD) camera.

The parameters of objective lens directly determine the focusing condition of fs laser pulse in micromachining. There are three main parameters of objection lens: magnification, numerical aperture (NA), and working distance (WD). Typically the lens with larger magnification have smaller WD and larger NA, which means the light is more tightly converged at a closer focus to the exit pupil. Table 2.2 tabulates the parameters of four microscope objective lens from Nikon Co.

Based on the Gaussian beam assumption, the focus diameter D (waist size) and depth Z_R (Rayleigh length) of fs laser beam can be calculated by the equations (2.12) and (2.13) [68].

$$D = 2w \approx 2\lambda f / \pi w_0 \approx 1.22\lambda / NA \tag{2.12}$$

$$Z_R = \pi w^2 / \lambda \tag{2.13}$$

where λ is wavelength, f is the focal length, ω_0 is the width of the incident beam. The focal parameters D and Z_R are both proportional to the wavelength of beam, and inverse proportion with the NA and NA^2 respectively. The higher NA lens has a smaller focal size D, and hence a higher laser intensity at focus. In fs laser micromachining, the pulse energy requirement is low for high NA lens. The Rayleigh length Z_R corresponding to a distance from the beam waist, where the beam radius is $\sqrt{2}Z_R$ and the mode area is doubled at this point for a circular beam. Therefore, the intensity of an fs laser beam with smaller Z_R value decrease faster after the focus position and hence has a swallow micromachining depth.

The calculated focal parameters for the fs laser system introduced in the paragraph after Figure 2.1 are provided in Table 2.2. The $I_{1\mu J}$ is the calculated peak intensity of a 1μJ pulse from the same fs laser system.

Table 2.2 Parameters of the objective lens and the fs laser focus for the micromachining system used

Magnification		**4x**	**10x**	**20x**	**40x**
NA	-	0.1	0.25	0.5	0.75
WD	mm	30	7	2.1	0.66

D	μm	9.8	3.9	1.95	1.3
$\mathbf{I_{1\mu J}}$	10^{17} W/m^2	2.2	14.1	55.8	125.6
$\mathbf{z_R}$	μm	93.5	15	3.7	1.7

2.3.3 Fiber post-processing by fs laser

Based on the mechanism of nonlinear light-matter interaction, a powerful fs laser pulse can be used to either remove or change the properties of both opaque and transparent materials. In this part, the applications of fs laser machining on optical fiber are reviewed.

The optical fibers are produced involves a great number of types with various compositions, such as the widely used silica, lead silicate [69], tellurite [70], and bismuth silicate [14]. However, in the glass family, the intensity requirements for fs laser micromachining have little difference. Figure 2.22 shows the threshold of various glasses in fs laser micromachining. Because of the low dependence of the threshold values on the materials' energy bandgap, the fs laser can be used in a broad range of glass material. To the fused silica (FS), the threshold intensity is ~3.5 x10^{17} W/m^2.

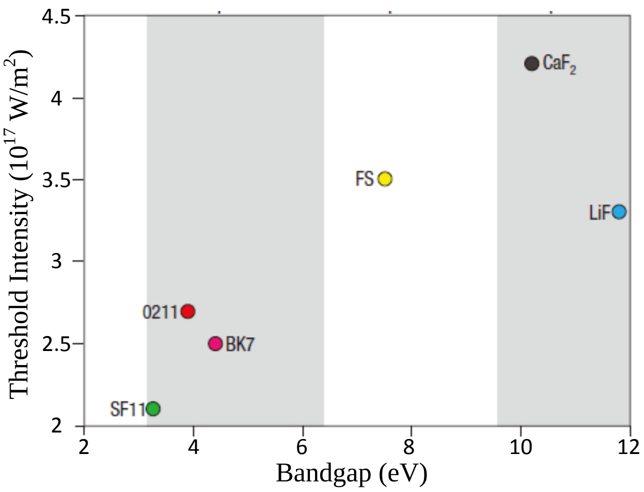

Figure 2.22 Threshold of various glasses for fs laser micromachining [71]

When fs laser pulse energy reaches the threshold value, the nonlinear absorption produces an RI change localized to the focal volume. Magnitude of the RI change varies in different materials, and related with fs laser parameters. Several mechanisms such as stress-induced changes, densification, and color center formation contribute differently for the RI change [65, 72, 73]. When the pulse energy increases beyond the threshold, density of the excited electrons plasma continuously increases. As the plasma energy increases, ionic shielding is reduced causing Coulomb repulsion between ions. A surge of Coulomb repulsion between ions with sufficient energy leads to permanent damage formation [72].

Based on the induced RI change or damage, fs laser micromachining has been used in post-processing optical fiber to building functional micro-structures, such as grating with long or short period, fiber top structure, micro void, and micro-fluidic channel.

For the grating inscription with fs laser pulses, there are two major techniques: the phase-mask-scanning technique and the direct-write technique. The first grating directly inscribed on conventional SM fiber by infrared fs radiation was a LPG reported by Y Kondo et al. Compared with the phase-mask-scanning technique, the direct-write techniques are flexible and cost-saving because no phase mask is required and the setup can be suitable for inscribing various gratings. However, the phase mask technique is commonly used in building short period grating, such as FBG, the high requirement to the positioning accuracy of translation stages constrain the application of the direct-write technique.

The principle and setup of phase-mask-scanning technique is similar to the conventional UV laser-based technique. Both type-I (by RI change) and type-II (by damaging) gratings can be fabricated by this technique [74]. The first FBG inscribed by infrared fs radiation on conventional SM fiber was reported by SJ Mihailov et al. a type-I grating with index modulation 1.9 x10^{-3} was achieved with peak fs intensity 1.2 x 10^{17} W/m^2. [75] Different to the FBG on SM fiber fabricated by UV laser, fiber sensitization (H_2 load) and annealing processes are not required for gratings inscribed by fs laser. Sooner after the first study are published, a type-II FBG by fs radiation with peak intensity of 4 x 10^{17} W/m^2 is realized on a SMF. Compared it with a type-I one, as illustrated in Figure 2.23, the type-II FBG exhibits highly insensitive to temperature. This may be the result of the two RI changes being written simultaneously during type-II FBG fabrication. [74]

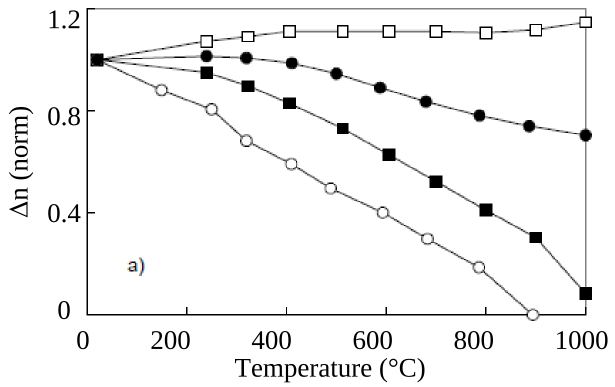

Figure 2.23 The RI modulations at different temperatures of various FBGs [74]; The white-square, black-circle, black-square, and white-circle represent the grating of Type-II IR fs, ps IR, Type-I IR fs, and type-I UV respectively.

The direct-write techniques do not need a costly phase mask in grating fabrication and hence flexible in both FBG and LPG grating fabrication. Three techniques can be cataloged into the direct-write technique. The point-by-point (PbP) technique might be the most widely used one in all three techniques. [76, 77] In this technique, the fs laser beam is focused on the core of a fiber and inscribe each points of the grating by exposure. However, the scattering losses introduced by this technique are more significant than the grating inscribed by the phase-mask-scanning technique. [78] The recent line-by-line (LbL) technique and continuous scanning technique illustrated in Figure 2.24 can solve the scattering loss problem by scanning fs laser focus across the fiber core rather than inscribing points in the core. The broadband transmission loss can be reduced to 0.1 dB which is comparable to the result of phase-mask-scanning technique.

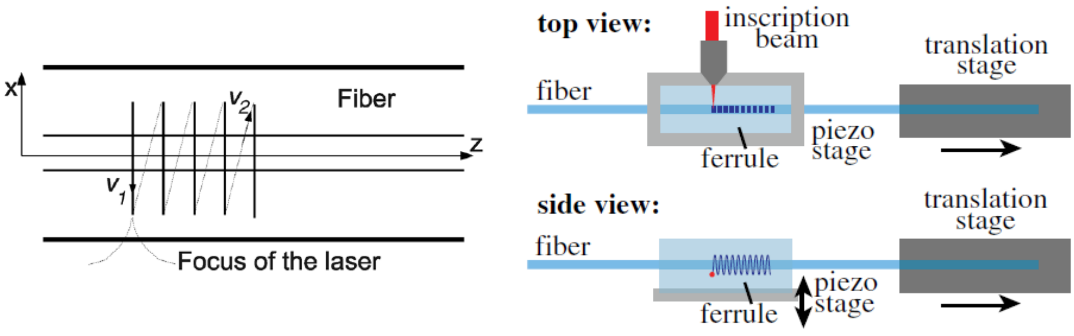

(a) (b)

Figure 2.24 (a) The line-by-line technique [79]; (b) The continuous scanning technique [80]

The multi-photon excitation property in fs laser micromachining allows inscribing gratings in non-photosensitive waveguide, such as fluoride fibers [81], sapphire fiber [82], and pure silica MOFs [83, 84], with techniques introduced in previous paragraphs. Benefit from high melting temperature (~2050°C) of sapphire fiber, the operation temperature of gratings written on this fiber can reach up to 2000°C. The gratings inscribed in MOFs enable the new generation fiber to be applied in sensing applications. The structured cladding is the major constrain of the grating fabrication in MOFs, because of the serious scattering to fs laser beam [84]. Normally, a long exposure time or high fs pulse energy is required in grating writing.

Many other devices can be fabricated in optical fibers with direct fs laser ablation. T. Wei and his colleague report a miniaturized in-line Fabry-Perot (FP) interferometer fabricated on a conventional SMF with fs laser. As illustrated in Figure 2.25 (a), the fiber is notched deeply from the surface of fiber. A FP cavity is formed in the notch by removing a section of fiber core. Advantages of the structure are the all-fiber structure and the accessible cavity which would be useful in high temperature sensing, and biochemical sensor based on RI measurement. [85] Figure 2.25 (b) are the cross-sectional SEM micrograph of an in-line Mach-Zehnder (MZ) interferometer reported by Y. Wang. Different to the FP structure, the fiber core is just partially removed with fs laser. The micro-cavity created by fs laser micromachining and the remnant of the fiber core are the two arms of the MZ interferometer. A high RI sensitivity of -9370 nm/RIU was achieved by a device with such a structure [86]. However, the background loss of these devices is high due to the scattering from machining surface with poor roughness. And the mechanical strength is poor of these types of device.

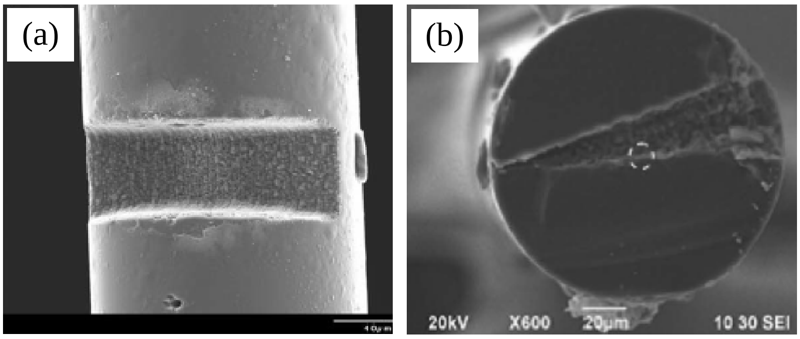

Figure 2.25 Micrographs of the optical fiber devices fabricated by direct fs laser ablation. (a) In-line FP interferometer [85]; (b) In-line MZ interferometer. The dashed white circle represents the location of core [86]

There are more possibilities in building optical fiber devices if the fs laser micromachining is applied together with other technique, such as etching, fusion splicing, and tapering. It is possible to produce micro-structure with high aspect-ratio in fiber by combining fs laser micromachining and chemical etching. As result of Si-O-Si bond angle changing with fs laser radiation, the treated regions exhibit a remarkably high etching rate, which is about 200 times faster than the non-affected region, in hydrofluoric (HF) acid solution [87]. Figure 2.26 (a) demonstrates a ~4 μm diameter micro-fluidic channel fabricated by HF acid etching the fiber with fs laser induced structure. The transmission power of the device exhibits a linear response to the RI of the channel between RI of 1.333 to 1.407 with sensitivity 56 dB/RIU. Figure 2.26 (b) is the micrograph of a micro-cantilever carved by fs laser and then etched with HF acid. Chemical etching is adopted in process to accelerate the generation of the structure. The small displacement of the cantilever can be calculated from the changing of interference signal.

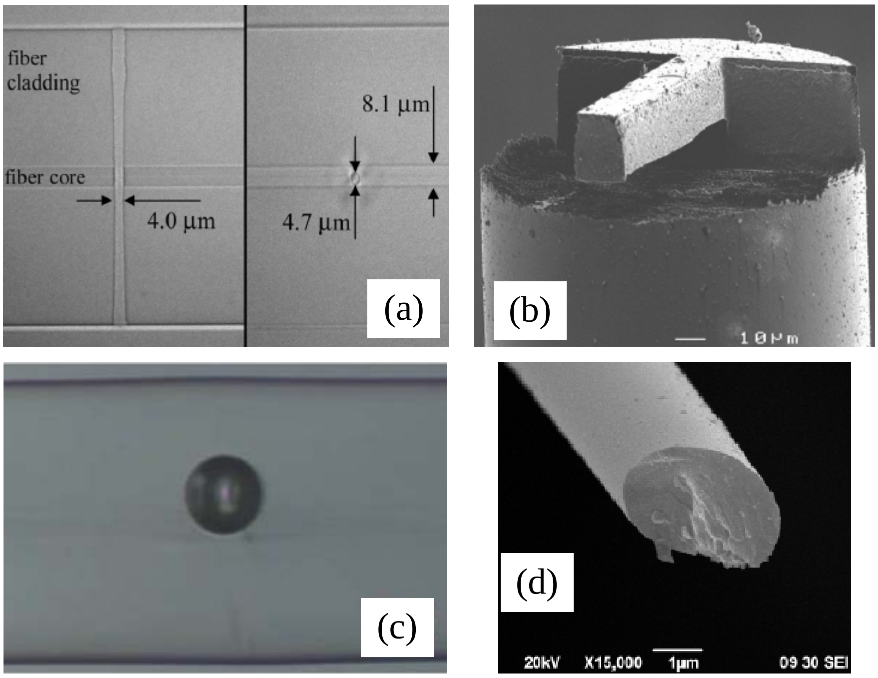

Figure 2.26 (a) Side view <left> and top view <right> of micro-channel [88]; (b) Fiber-top cantilever [89]; (c) In-line MZ interferometer [90]; (d) Highly birefringent microfibers [91]

Figure 2.26 (c) is a fiber in-line MZ interferometer constructed by an air void adjacent to the fiber core. The micro-void is fabricated in two steps. At first, a small hole is drilled on fiber top of a SMF. Then the fiber is fusion spliced to an unprocessed SMF. The device exhibits high temperature sensitivity of ~43.2 pm/°C, up to 1000°C. [90] Figure 2.26 (d) shows the local SEM micrograph of an air-clad microfiber with high birefringence up to 10^{-2} RIU, and small dimension. The highly birefringence microfiber is fabricated by tapering a processed SMF which is pared on both side with fs Laser. [91]

2.4 Summary

In this chapter, the structural features of some typical MOFs are reviewed. Two widely used fabrication techniques are also introduced. In addition, two widely used techniques for fiber post-processing, that is the fiber tapering and the fs laser micro-machining, are presented in detail.

2.5 References

[1]. P. J. s. Russell, "Photonic crystal fiber: finding the holey grail," Optics and photonics news **18**, 26-31 (2007).

[2]. W. Jin, H. Xuan, and H. Ho, "Sensing with hollow-core photonic bandgap fibers," Measurement Science and Technology **21**, 094014 (2010).

[3]. O. Frazão, R. M. Silva, M. S. Ferreira, J. L. Santos, and A. B. L. Ribeiro, "Suspended-core fibers for sensing applications," Photonic Sensors **2**, 118-126 (2012).

[4]. J. Canning, "Diffraction-free mode generation and propagation in optical waveguides," Optics Communications **207**, 35-39 (2002).

[5]. C. Martelli, J. Canning, K. Lyytikainen, and N. Groothoff, "Water-core Fresnel fiber," Opt. Express **13**, 3890-3895 (2005).

[6]. G. R. Hadley, J. G. Fleming, and S.-Y. Lin, "Bragg fiber design for linear polarization," Optics Letters **29**, 809-811 (2004).

[7]. P. Kaiser, E. A. J. Marcatili, and S. E. Miller, "A New Optical Fiber," The Bell System Technical Journal **52**, 265-269 (1973).

[8]. J. Knight, T. Birks, P. S. J. Russell, and D. Atkin, "All-silica single-mode optical fiber with photonic crystal cladding," Optics Letters **21**, 1547-1549 (1996).

[9]. R. Cregan, B. Mangan, J. Knight, T. Birks, P. S. J. Russell, P. Roberts, and D. Allan, "Single-mode photonic band gap guidance of light in air," Science **285**,

1537-1539 (1999).

[10]. J. Knight, J. Broeng, T. Birks, and P. S. J. Russell, "Photonic band gap guidance in optical fibers," Science **282**, 1476-1478 (1998).

[11]. P. Bennett, T. Monro, and D. Richardson, "A robust, large air fill fraction holey fibre," in *Lasers and Electro-Optics, 1999. CLEO'99. Summaries of Papers Presented at the Conference on*(IEEE, 1999), p. 293.

[12]. P. Westbrook, B. Eggleton, R. Windeler, A. Hale, T. Strasser, and G. Burdge, "Cladding-mode resonances in hybrid polymer-silica microstructured optical fiber gratings," Photonics Technology Letters, IEEE **12**, 495-497 (2000).

[13]. L. Fu, B. K. Thomas, and L. Dong, "Efficient supercontinuum generations in silica suspended core fibers," Optics Express **16**, 19629-19642 (2008).

[14]. H. Ebendorff-Heidepriem, P. Petropoulos, S. Asimakis, V. Finazzi, R. Moore, K. Frampton, F. Koizumi, D. Richardson, and T. Monro, "Bismuth glass holey fibers with high nonlinearity," Optics Express **12**, 5082-5087 (2004).

[15]. O. Frazão, R. M. Silva, J. Kobelke, and K. Schuster, "Temperature-and strain-independent torsion sensor using a fiber loop mirror based on suspended twin-core fiber," Optics Letters **35**, 2777-2779 (2010).

[16]. R. Silva, M. Ferreira, J. Kobelke, K. Schuster, and O. Frazão, "Simultaneous measurement of curvature and strain using a suspended multicore fiber," Optics Letters **36**, 3939-3941 (2011).

[17]. T. M. Monro, W. Belardi, K. Furusawa, J. C. Baggett, N. G. Broderick, and D. J. Richardson, "Sensing with microstructured optical fibres," Measurement Science and Technology **12**, 854 (2001).

[18]. Y. Zhu, H. Du, and R. Bise, "Design of solid-core microstructured optical fiber with steering-wheel air cladding for optimal evanescent-field sensing," Optics Express **14**, 3541-3546 (2006).

[19]. E. Mägi, H. Nguyen, and B. Eggleton, "Air-hole collapse and mode

transitions in microstructured fiber photonic wires," Optics Express **13**, 453 (2005).

[20]. M. Liao, C. Chaudhari, X. Yan, G. Qin, C. Kito, T. Suzuki, and Y. Ohishi, "A suspended core nanofiber with unprecedented large diameter ratio of holey region to core," Optics Express **18**, 9088-9097 (2010).

[21]. G. Brambilla, F. Xu, and X. Feng, "Fabrication of optical fibre nanowires and their optical and mechanical characterisation," Electronics Letters **42**, 517-519 (2006).

[22]. K. Zamani Aghaie, M. J. Digonnet, and S. Fan, "Experimental assessment of the accuracy of an advanced photonic-bandgap-fiber model," Journal of Lightwave Technology **31**, 1015-1022 (2013).

[23]. C. Markos, S. N. Yannopoulos, and K. Vlachos, "Chalcogenide glass layers in silica photonic crystal fibers," Optics Express **20**, 14814-14824 (2012).

[24]. S. Liu, L. Jin, W. Jin, D. Wang, C. Liao, and Y. Wang, "Structural long period gratings made by drilling micro-holes in photonic crystal fibers with a femtosecond infrared laser," Optics Express **18**, 5496-5503 (2010).

[25]. P. J. s. Russell, "Photonic crystal fibers," Science **299**, 358-362 (2003).

[26]. H. Ebendorff-Heidepriem, and T. M. Monro, "Extrusion of complex preforms for microstructured optical fibers," Optics Express **15**, 15086-15092 (2007).

[27]. H. Ebendorff-Heidepriem, S. C. Warren-Smith, and T. M. Monro, "Suspended nanowires: fabrication, design and characterization of fibers with nanoscale cores," Optics Express **17**, 2646-2657 (2009).

[28]. R. T. Bise, and D. J. Trevor, "Sol-gel derived microstructured fiber: Fabrication and characterization," in *Proc. OFC*(2005), pp. 1-3.

[29]. A. S. Webb, F. Poletti, D. J. Richardson, and J. K. Sahu, "Suspended-core holey fiber for evanescent-field sensing," Optical Engineering **46**, 010503-010503-010503 (2007).

[30]. T. Birks, J. Knight, and P. S. J. Russell, "Endlessly single-mode photonic crystal fiber," Optics Letters **22**, 961-963 (1997).

[31]. K. Okamoto, *Fundamentals of Optical Waveguides* (Academic Press, 2006).

[32]. P. S. J. Russell, "Photonic-crystal fibers," Journal of Lightwave Technology **24**, 4729-4749 (2006).

[33]. J. Knight, T. Birks, R. Cregan, P. S. J. Russell, and P. De Sandro, "Large mode area photonic crystal fibre," Electronics Letters **34**, 1347-1348 (1998).

[34]. M. N. Petrovich, F. Poletti, A. van Brakel, and D. J. Richardson, "Robustly single mode hollow core photonic bandgap fiber," in *Optical Fiber communication/National Fiber Optic Engineers Conference, 2008. OFC/NFOEC 2008. Conference on*(IEEE, 2008), pp. 1-3.

[35]. T. A. Birks, and Y. W. Li, "The Shape of Fiber Tapers," Journal of Lightwave Technology **10**, 432-438 (1992).

[36]. S. Leon-Saval, T. Birks, W. Wadsworth, P. St J Russell, and M. Mason, "Supercontinuum generation in submicron fibre waveguides," Optics Express **12**, 2864-2869 (2004).

[37]. J. M. Ward, D. G. OShea, B. J. Shortt, M. J. Morrissey, K. Deasy, and S. G. Nic Chormaic, "Heat-and-pull rig for fiber taper fabrication," Review of scientific instruments **77**, 083105-083105-083105 (2006).

[38]. G. Brambilla, E. Koizumi, X. Feng, and D. J. Richardson, "Compound-glass optical nanowires," Electronics Letters **41**, 400-402 (2005).

[39]. L. Tong, R. R. Gattass, J. B. Ashcom, S. He, J. Lou, M. Shen, I. Maxwell, and E. Mazur, "Subwavelength-diameter silica wires for low-loss optical wave guiding," Nature **426**, 816-819 (2003).

[40]. J. Warnatz, U. Maas, and R. W. Dibble, *Combustion: physical and chemical fundamentals, modeling and simulation, experiments, pollutant formation*

(Springer, 2006).

[41]. C. K. Law, *Combustion physics* (Cambridge University Press, 2006).

[42]. T. Birks, and K. Oakley, "Control of optical fibre taper shape," Electronics Letters **27**, 1654-1656 (1991).

[43]. K. Boyd, H. Ebendorff-Heidepriem, T. M. Monro, and J. Munch, "Surface tension and viscosity measurement of optical glasses using a scanning CO2 laser," Optical Materials Express **2**, 1101-1110 (2012).

[44]. E. Magi, P. Steinvurzel, and B. Eggleton, "Transverse characterization of tapered photonic crystal fibers," Journal of Applied Physics **96**, 3976-3982 (2004).

[45]. W. Wadsworth, A. Witkowska, S. Leon-Saval, and T. A. Birks, "Hole inflation and tapering of stock photonic crystal fibres," Optics Express **13**, 6541-6549 (2005).

[46]. J. Love, W. Henry, W. Stewart, R. Black, S. Lacroix, and F. Gonthier, "Tapered single-mode fibres and devices. Part 1: Adiabaticity criteria," IEE Proceedings J (Optoelectronics) **138**, 343-354 (1991).

[47]. A. W. Snyder, and J. Love, *Optical waveguide theory* (Springer, 1983).

[48]. H. C. Nguyen, B. T. Kuhlmey, M. J. Steel, C. L. Smith, E. C. Mägi, R. C. McPhedran, and B. J. Eggleton, "Leakage of the fundamental mode in photonic crystal fiber tapers," Optics Letters **30**, 1123-1125 (2005).

[49]. K. Lai, A. Witkowska, S. G. Leon-Saval, W. J. Wadsworth, and T. A. Birks, "Fibre core shape transitions for optical interfacing," in *Optical Fiber Communication Conference*(Optical Society of America, 2006).

[50]. J. Ju, H. F. Xuan, W. Jin, S. Liu, and H. L. Ho, "Selective opening of airholes in photonic crystal fiber," Optics Letters **35**, 3886-3888 (2010).

[51]. A. Witkowska, K. Lai, S. Leon-Saval, W. Wadsworth, and T. Birks, "All-fiber anamorphic core-shape transitions," Optics Letters **31**, 2672-2674 (2006).

[52]. R. Fork, B. Greene, and C. Shank, "Generation of optical pulses shorter

than 0.1 psec by colliding pulse mode locking," Applied Physics Letters **38**, 671 (1981).

[53]. I. D. Jung, F. X. Kärtner, N. l. Matuschek, D. H. Sutter, F. Morier-Genoud, G. Zhang, U. Keller, V. Scheuer, M. Tilsch, and T. Tschudi, "Self-starting 6.5-fs pulses from a Ti:sapphire laser," Optics Letters **22**, 1009-1011 (1997).

[54]. G. Cerullo, S. D. Silvestri, and V. Magni, "Self-starting Kerr-lens mode locking of a Ti: sapphire laser," Optics Letters **19**, 1040-1042 (1994).

[55]. P. Maine, D. Strickland, P. Bado, M. Pessot, and G. Mourou, "Generation of ultrahigh peak power pulses by chirped pulse amplification," Quantum Electronics, IEEE Journal of **24**, 398-403 (1988).

[56]. D. Strickland, and G. Mourou, "Compression of amplified chirped optical pulses," Optics Communications **55**, 447-449 (1985).

[57]. E. W. Gaul, M. Martinez, J. Blakeney, A. Jochmann, M. Ringuette, D. Hammond, T. Borger, R. Escamilla, S. Douglas, and W. Henderson, "Demonstration of a 1.1 petawatt laser based on a hybrid optical parametric chirped pulse amplification/mixed Nd: glass amplifier," Applied Optics **49**, 1676-1681 (2010).

[58]. C. B. Schaffer, A. Brodeur, and E. Mazur, "Laser-induced breakdown and damage in bulk transparent materials induced by tightly focused femtosecond laser pulses," Measurement Science and Technology **12**, 1784 (2001).

[59]. M. D. Perry, and G. Mourou, "Terawatt to petawatt subpicosecond lasers," Science **264**, 917-924 (1994).

[60]. E. Glezer, M. Milosavljevic, L. Huang, R. Finlay, T.-H. Her, J. P. Callan, and E. Mazur, "Three-dimensional optical storage inside transparent materials," Optics Letters **21**, 2023-2025 (1996).

[61]. K. Venkatakrishnan, B. Ngoi, P. Stanley, L. Lim, B. Tan, and N. Sivakumar, "Laser writing techniques for photomask fabrication using a femtosecond laser," Applied Physics A **74**, 493-496 (2002).

[62]. K. Miura, J. Qiu, H. Inouye, T. Mitsuyu, and K. Hirao, "Photowritten optical waveguides in various glasses with ultrashort pulse laser," Applied Physics Letters **71**, 3329 (1997).

[63]. K. M. Davis, K. Miura, N. Sugimoto, and K. Hirao, "Writing waveguides in glass with a femtosecond laser," Optics Letters **21**, 1729-1731 (1996).

[64]. Y. Cheng, K. Sugioka, and K. Midorikawa, "Microfluidic laser embedded in glass by three-dimensional femtosecond laser microprocessing," Optics Letters **29**, 2007-2009 (2004).

[65]. J. Chan, T. Huser, S. Risbud, and D. Krol, "Structural changes in fused silica after exposure to focused femtosecond laser pulses," Optics Letters **26**, 1726-1728 (2001).

[66]. X. Fang, C. Liao, and D. Wang, "Femtosecond laser fabricated fiber Bragg grating in microfiber for refractive index sensing," Optics Letters **35**, 1007-1009 (2010).

[67]. T. Juhasz, F. H. Loesel, R. M. Kurtz, C. Horvath, J. F. Bille, and G. Mourou, "Corneal refractive surgery with femtosecond lasers," Selected Topics in Quantum Electronics, IEEE Journal of **5**, 902-910 (1999).

[68]. Y. Li, C. Liao, D. Wang, T. Sun, and K. Grattan, "Study of spectral and annealing properties of fiber Bragg gratings written in H2-free and H2-loaded fibers by use of femtosecond laser pulses," Optics Express **16**, 21239-21247 (2008).

[69]. K. Kiang, K. Frampton, T. M. Monro, R. Moore, J. Tucknott, D. Hewak, D. J. Richardson, and H. Rutt, "Extruded singlemode non-silica glass holey optical fibres," Electronics Letters **38**, 546-547 (2002).

[70]. V. Kumar, A. George, J. C. Knight, and P. s. J. Russell, "Tellurite photonic crystal fiber," Optics Express **11**, 2641-2645 (2003).

[71]. R. R. Gattass, and E. Mazur, "Femtosecond laser micromachining in transparent materials," Nature photonics **2**, 219-225 (2008).

[72]. E. N. Glezer, and E. Mazur, "Ultrafast-laser driven micro-explosions in transparent materials," Applied Physics Letters **71**, 882-884 (1997).

[73]. C. B. Schaffer, J. F. García, and E. Mazur, "Bulk heating of transparent materials using a high-repetition-rate femtosecond laser," Applied Physics A **76**, 351-354 (2003).

[74]. C. W. Smelser, S. J. Mihailov, and D. Grobnic, "Formation of Type I-IR and Type II-IR gratings with an ultrafast IR laser and a phase mask," Optics Express **13**, 5377-5386 (2005).

[75]. S. J. Mihailov, C. W. Smelser, P. Lu, R. B. Walker, D. Grobnic, H. Ding, G. Henderson, and J. Unruh, "Fiber Bragg gratings made with a phase mask and 800-nm femtosecond radiation," Optics Letters **28**, 995-997 (2003).

[76]. Y. Kondo, K. Nouchi, T. Mitsuyu, M. Watanabe, P. G. Kazansky, and K. Hirao, "Fabrication of long-period fiber gratings by focused irradiation of infrared femtosecond laser pulses," Optics Letters **24**, 646-648 (1999).

[77]. A. Martinez, Y. Lai, M. Dubov, I. Khrushchev, and I. Bennion, "Vector bending sensors based on fibre Bragg gratings inscribed by infrared femtosecond laser," Electronics Letters **41**, 472-474 (2005).

[78]. M. L. Åslund, N. Nemanja, N. Groothoff, J. Canning, G. D. Marshall, S. D. Jackson, A. Fuerbach, and M. J. Withford, "Optical loss mechanisms in femtosecond laser-written point-by-point fibre Bragg gratings," Opt. Express **16**, 14248-14254 (2008).

[79]. K. Zhou, M. Dubov, C. Mou, L. Zhang, V. K. Mezentsev, and I. Bennion, "Line-by-line fiber Bragg grating made by femtosecond laser," Photonics Technology Letters, IEEE **22**, 1190-1192 (2010).

[80]. R. J. Williams, R. G. Krämer, S. Nolte, and M. J. Withford, "Femtosecond direct-writing of low-loss fiber Bragg gratings using a continuous core-scanning technique," Optics Letters **38**, 1918-1920 (2013).

[81]. S. J. Mihailov, C. W. Smelser, D. Grobnic, R. B. Walker, P. Lu, H. Ding, and J. Unruh, "Bragg gratings written in all-SiO2 and Ge-doped core fibers with 800-nm femtosecond radiation and a phase mask," Journal of Lightwave Technology **22**, 94 (2004).

[82]. D. Grobnic, S. J. Mihailov, C. W. Smelser, and H. Ding, "Sapphire fiber Bragg grating sensor made using femtosecond laser radiation for ultrahigh temperature applications," Photonics Technology Letters, IEEE **16**, 2505-2507 (2004).

[83]. A. Cusano, D. Paladino, and A. Iadicicco, "Microstructured fiber Bragg gratings," Journal of Lightwave Technology **27**, 1663-1697 (2009).

[84]. J. Canning, N. Groothoff, K. Cook, C. Martelli, A. Pohl, J. Holdsworth, S. Bandyopadhyay, and M. Stevenson, "Gratings in structured optical fibres," Laser Chemistry **2008** (2008).

[85]. T. Wei, Y. Han, H.-L. Tsai, and H. Xiao, "Miniaturized fiber inline Fabry-Perot interferometer fabricated with a femtosecond laser," Optics Letters **33**, 536-538 (2008).

[86]. Y. Wang, M. Yang, D. Wang, S. Liu, and P. Lu, "Fiber in-line Mach-Zehnder interferometer fabricated by femtosecond laser micromachining for refractive index measurement with high sensitivity," JOSA B **27**, 370-374 (2010).

[87]. Y. Bellouard, A. Said, M. Dugan, and P. Bado, "Fabrication of high-aspect ratio, micro-fluidic channels and tunnels using femtosecond laser pulses and chemical etching," Optics Express **12**, 2120-2129 (2004).

[88]. Y. Lai, K. Zhou, L. Zhang, and I. Bennion, "Microchannels in conventional single-mode fibers," Optics Letters **31**, 2559-2561 (2006).

[89]. A. Said, M. Dugan, S. de Man, and D. Iannuzzi, "Carving fiber-top cantilevers with femtosecond laser micromachining," Journal of Micromechanics and Microengineering **18**, 035005 (2008).

[90]. T. Hu, Y. Wang, C. Liao, and D. Wang, "Miniaturized fiber in-line Mach–Zehnder interferometer based on inner air cavity for high-temperature sensing," Optics Letters **37**, 5082-5084 (2012).

[91]. H. F. Xuan, J. Ju, and W. Jin, "Highly birefringent optical microfibers," Optics Express **18**, 3828-3839 (2010).

Chapter 3 : Fabrication of the Suspended Core (SC) Microcells

In this chapter, a modified selective inflation technique for fabricating suspended core (SC) microcell is introduced. The technique contains two steps, which are the selective opening air-columns of a PCF, and then the pressurizing and inflating the processed PCF. Details of the two steps are introduced in section 3.1 and 3.2. By use of the technique, six types of microcells with different structures are realized. The structural and optical properties of three types of the microcells are discussed in section 3.3.

3.1 Selective opening of PCF

The purpose of first step, selective opening, is to create channels to some purposely chosen air-columns of a PCF. The channels will serve as the inlet of high pressure gas in the next step; it can also be used in applications where the selectively infiltrate fluid in PCF is required. The main instruments used in this step include femtosecond (fs) laser, micro-machining platform, and fusion splicer.

Figure 3.1 shows the outcome of this step. Some air-columns of the PCF are opened at their left end, while, at the same end, the remaining air-columns in fiber are blocked. Right end of the PCF is spliced to a SMF to block all holes at this end. Therefore, only the chosen air-columns of the PCF are open to the environment via the openings, the other columns are hermetically sealed.

Figure 3.1 Selective openings on a PCF

Many hole-selection techniques have been proposed in recent years. According to the range of selection region, the techniques can be divided into sectional selection and one-by-one selection. As name implies, the one-by-one techniques can select each air-column in MOFs. Techniques in this group are suitable for SC microcell fabrication and will be discussed in this section. The sectional selection techniques are also useful in some applications where infiltration a number of air-columns is required [1, 2].

The schemes of some widely used hole-selection techniques are summarized in Figure 3.2. The technique depicted in figure (a) applying a capillary with similar bore-size to air-columns of a MOF to align target air-column. After fusion splicing process, one air-column is selectively opened [3]. Micrograph in figure (b) shows a borosilicate glass probe with submicron scale tip. The probe can be used for selecting holes of most MOFs with the aid of microscope and accurate displacement platform [4]. A similar technique is also provided in article [5] by use of a micro-pipette (with outer diameter of ~1 μm). In figure (c), the cleaved end of a MOF is deposited with photoresist SU-8 firstly. Then the chosen holes are illuminated with focused Ti:Sapphire fs laser beam. Due to two-photon absorption phenomenon, the polymerized SU-8 finally blocks the exposed holes. By hardback and developing process, the un-polymerized photoresist can be removed and open to the environment [6]. The fs laser assisted hole-selection technique in figure (d) is developed by our team [7, 8]. In the technique, firstly, a MOF is spliced with a SMF to seal all holes. Then the SMF is cut by fs laser at a position near to the splicing point (marked by the line in figure (d)). After cutting, the holes on the PCF end are visible from the direction towards the fiber end face. The direction is indicated by the arrow in figure (b). From the same direction, the fs laser pulses are focused on the plane I of at the position aligned to the target holes. As a result, micro-channel will come into being in the SMF remnant with only few seconds fs laser exposure.

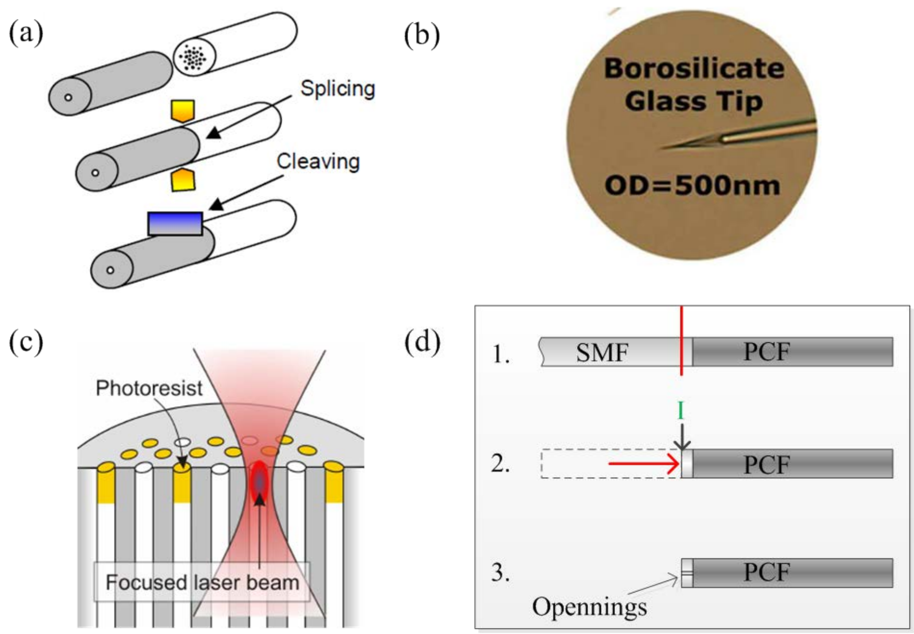

Figure 3.2 The one-by-on hole-selection techniques of (a) Capillary assisted selectively opening [3]; (b) submicron tip selectively blocking [4]; (c) selectively blocking by two-photon polymerization [6]; (d) fs laser assisted selectively opening

The techniques in figure (b) and (c) can be further classified as selective-filling; and the techniques in figure (a) and (d) can be classified as selective-opening. The former techniques are suitable to open majority of holes of MOF end, and the latter ones are suitable to open few holes.

In SC microcell fabrication, only few holes are required for pressurization. The selective opening techniques should be a better choice. Compared with the technique (a) in Figure 3.2, technique (d) are more convenient in locating each hole by microscopy system. Accordingly, the fs laser assisted technique is adopted in fabricating SC microcells. Details of applying the technique can be explained with the aid of Figure 3.3.

The splicing current in step 1 is typically low to minimize the collapse of PCF holes. The splicing point hence is fragile compare with SMF-SMF splicing. The shock of conventional mechanical cutting may cause the splicing point broken. This is the reason why fs laser is used to cut the SMF. The energy of fs laser pulses used in fiber cutting is about 1 μJ with a 40x object lens. The cutline in step 1 is about 15 μm apart from the splicing point. Note that the distance should not be too large for the reason of facilitating observation and drilling in step 2.

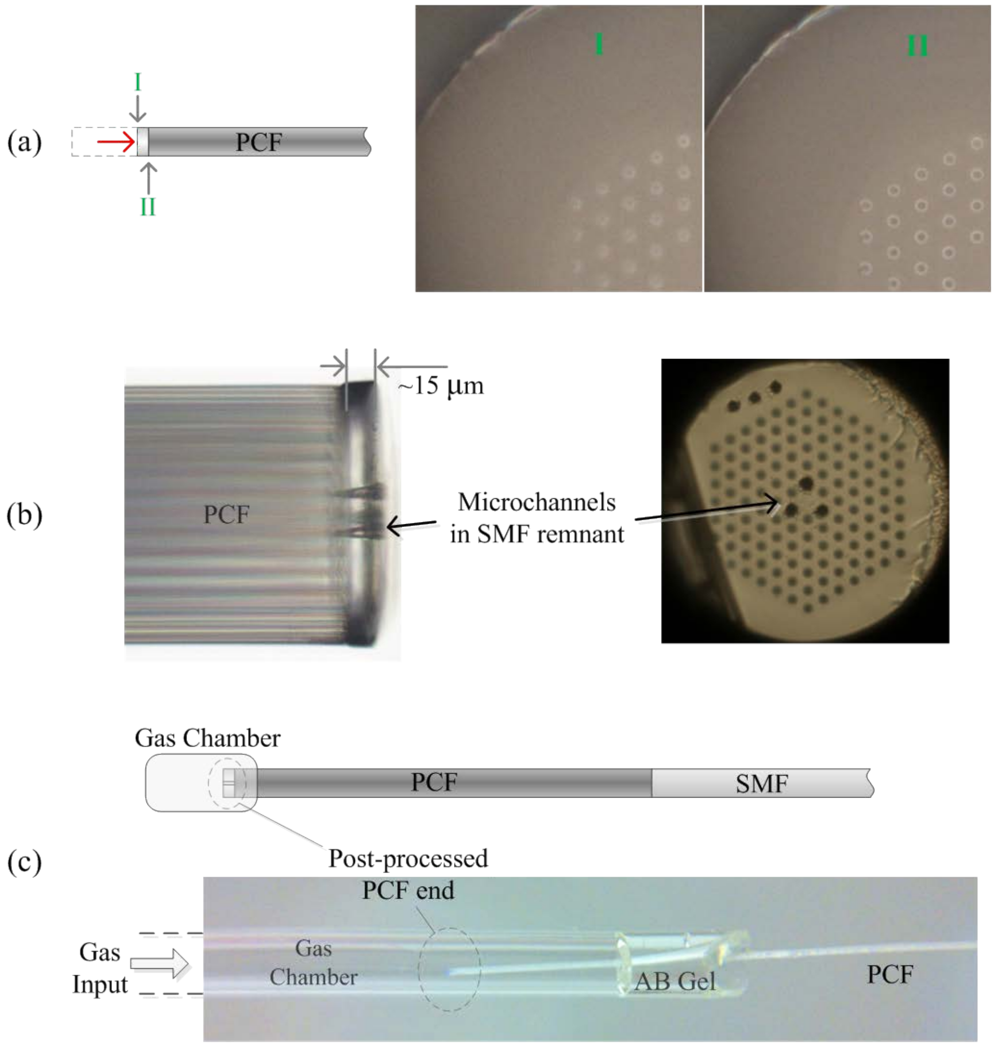

Figure 3.3 (a) Micrographs of a sealed fiber top with focal at position I & II; (b)Micrographs of side-view (left) and top-view (right) of a PCF with selective openings; (c) encapsulation of the processed PCF end in a gas chamber

The micrographs of a sealed PCF top are given in Figure 3.3 (a). The holes position can be clearly located when the lens focus on plane II. To perforate the SMF remnant, the exposure time and energy of fs laser pulses are set to 1-2 second and about 1.6 μJ respectively with a 40x object lens. From the micrographs in Figure 3.3 (b), micro-channels in SMF remnant can be clearly observed.

Finally, as illustrated in Figure 3.3 (c), the processed PCF end with micro-channels is inserted into a glass tube, and then sealed with AB glue. The versatile assembly can be used to infiltrate various fluidic materials into the selected air-columns of PCFs. In my experiments, high pressure gas is applied to the glass tube, which is also called gas chamber in this application, to pressurize the selected air-columns for the next inflation process.

3.2 Pressurization and Inflation Processes

In second step, that is pressurization and inflation process, the selective opened PCF are pressurized, and then locally heated up to the temperature around softening point of silica. The flow of softened silica in heat region causes a gradual change of the fiber's PC structure. Finally a local new structure is generated in the PCF under the combined action of pressure in air-columns, surface tension of silica, gravity of fiber etc. Schematic of the process is given in Figure 3.4. The main instruments used in this step are gas cylinder, and heat source such as fiber tapering machine, fusion splicer.

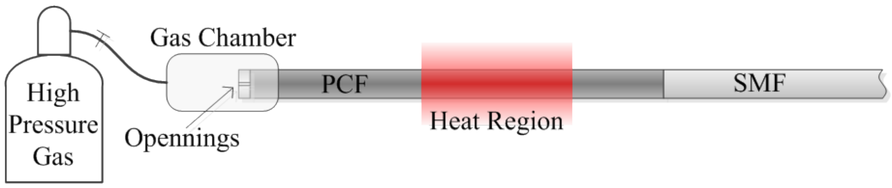

Figure 3.4 Schematic of the pressurization and inflation process

3.2.1 Theory of gas pressurization

Due to the wall effect, the delivering of gas pressure exerted by particle collisions is constrained in capillary with small bore size. The transfer rate of pressure decreases dramatically with the dimension of gas channel. Previous experiments by tracing gas detection show that the diffusion coefficient of gas molecules in the MOFs' air-columns is ~5.4% (PCF) and ~1.25% (PBGF) smaller than the standard value. [9, 10]. When positive pressure is applied to the gas chamber, a period of time is required before the pressures in the selected PCF air-columns become balanced. How long shall it take to achieve balance is a practical problem may be encounter in the PCF pressurization process. In this part, the temporal response of the pressure in air-columns will be studied.

The pressure in PCFs is set up by the nitrogen flow driven by the pressure gradient in the air-columns. The characters of a gas flow are determined by the Knudsen number defined as:

$$K_n \equiv \bar{\lambda} / d \tag{3.1}$$

where $\bar{\lambda}$ is the mean free path between intermolecular collisions, d is the diameter of air-column. A number of different flow regimes can be roughly defined in terms of K_n. The gas flow with $K_n >> 1$ is called free molecular flow and described by kinetic gas theory. In this regime the intermolecular collision is rare comparing to the molecular-wall collision. The gas flow with $K_n << 1$ is essentially hydrodynamic and described by the Navier-Stokes equations. The transition with $K_n \approx 1$ between two flow statuses is called slip flow. [11]

Based on the ideal gas assumption, the mean free path of homogeneous gas can be calculated by: [12]

$$\bar{\lambda} = \frac{RT}{\sqrt{2}\pi d_m^2 N_A P} \tag{3.2}$$

where R ≈8.314 J/(mol·K) is the gas constant, N_A ≈6.022 x10^{23} /mol is the Avogadro's number. T, d_m, P are the temperature in K, molecular diameter in meter and gas pressure in Pascal respectively. The nitrogen molecules is assumed to be hard spheres with diameter $d_m \approx 0.375$nm (from [13], page 26). Table 3.1 lists the mean free paths of nitrogen gas at 20°C with pressure from 1-9 Bar, and corresponding Knudsen number in the air-columns of LMA-10 and ESM-12.

Table 3.1 Mean free path and Knudsen number of Nitrogen at 20°C

Pressure P	bar	1	3	5	7	9
Mean free path $\bar{\lambda}$	nm	63.8	21.3	12.8	9.1	7.1
$\boldsymbol{K_{n,\,\mathrm{LMA\text{-}10}}}$	x10^{-3}	18.9	6.3	3.8	2.7	2.1
$\boldsymbol{K_{n,\,\mathrm{ESM\text{-}12}}}$	x10^{-3}	18.2	6.1	3.7	2.6	2

Since K_n <<1, the theory for hydrodynamic flow would be feasible for describing the pressurization procedure of PCF. The transportation equation for the gas flows through the smooth tube (little turbulence) takes the form for Poiseuille flow: [14]

$$\Phi = \frac{n}{A}\cdot\frac{\pi d^4}{128\eta}\cdot\frac{\partial p}{\partial x} \tag{3.3}$$

where Φ is the flux of gas molecules, η is the dynamic viscosity; n is the numbers of gas molecules; p, d, A are, respectively, the gas pressure, inner diameter and cross-section of the tube. Using the ideal gas law, equation (3.3) can be rewrite as:

$$\frac{\partial p}{\partial t} = \frac{d^2}{32\eta}\cdot\frac{\partial}{\partial x}\left(p\frac{\partial p}{\partial x}\right) \tag{3.4}$$

To get a more general relation for the relation among the pressure p, position x and time t, the dimensionless parameters in (3.5) are introduced:

$$\frac{p}{p_0} = \kappa; \quad \frac{x}{L} = \xi \tag{3.5}$$

where p_0 represents the applying pressure to the tube with length L.

Since the L, d, p_0 are all constant for the pressurization process, to simplify the equation, a dimensionless time τ is used. τ is related to the real time t by (3.6).

$$t = \frac{32\eta L^2}{d^2 p_0}\tau \tag{3.6}$$

By applying the normalized or dimensionless parameters, equation (3.4) can be simplified to the form of equation (3.7)

$$\frac{\partial \kappa}{\partial \tau}=\frac{\partial}{\partial \xi}\left(\kappa \frac{\partial \kappa}{\partial \xi}\right) \tag{3.7}$$

To simulate the pressurization process in our experiment, the boundary conditions (3.8) are applied to the differential equation (3.7).

$$\kappa(\xi,\tau)\big|_{\xi=0,\tau=0}=p_i/p_0;\quad \kappa(\xi,\tau)\big|_{\tau=\infty}=1;\quad \kappa_\xi(\xi,\tau)\big|_{\xi=1}=0 \tag{3.8}$$

where the constant p_i is the initial pressure in air-column. The first condition in (3.8) represents the initial pressure status in the tube. The second one represents the final equilibrium status. The third one represents the pressure continuum at the sealed end.

The venting process of the air-column can also be simulated by use of equation (3.7) with different boundary conditions. In practice, the gas in air-columns is released by opening both sides of the PCF to the air. This venting process is described by the conditions:

$$\kappa(\xi,\tau)\big|_{\xi=0,\tau=0}=1;\quad \kappa(\xi,\tau)\big|_{\tau=\infty}=p_i/p_0;\quad \kappa(\xi,\tau)\big|_{\xi=1}=p_i/p_0 \tag{3.9}$$

Equation (3.7) was solved numerically by Matlab software for both the pressurization and the venting process. The results are presented in Figure 3.5. Variation of the gas pressure at particular position of air-column decreases with the time growth. Therefore the pressure equilibrium in air-columns is a deceleration process for both the pressurization and the venting.

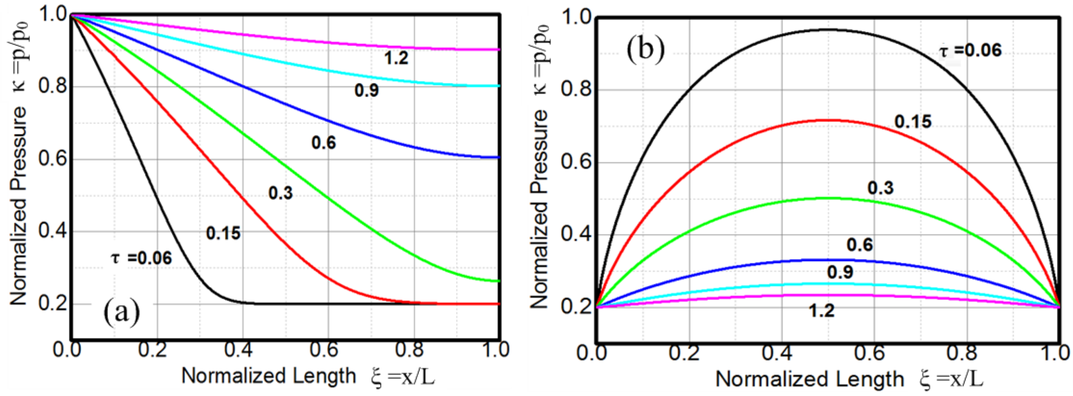

Figure 3.5 Development of normalized pressure ξ along gas channel (a) Pressurization process (p_0 = 5 bar, one port); (b) Venting process with two outlets

The pressurization procedure of LMA-10 and ESM-12 PCF can be simulated with the theory. Sizes of the air-columns in the PCFs are given in Table 2.1. the dynamic viscosity of nitrogen at 25°C is about 17.9 μPa·s [15]. In the simulation, one port of the fiber is set to 5 Bar pressure, and the other port is sealed.

Figure 3.6 (a) shows the development of pressures in the air-columns of 1-, 3- and 5-meter LMA-10 (solid line) and ESM-12 (dash line) PCF at the sealed fiber end. The pressure settling time increases significantly with length of fiber. For 1-meter PCF, about five minutes are required for the pressure in fiber to achieve stable. But for 3-meter PCF, at least 30mintus are needed. And for 5-meter PCF, the settling time becomes longer. Figure 3.6 (b) shows the calculated results of pressure growing at sealed end of a 3 meters length LMA-10 PCF. The fiber is pressurized with different gas pressure for each curve in figure. The settling time becomes shorter when higher pressure is imposed.

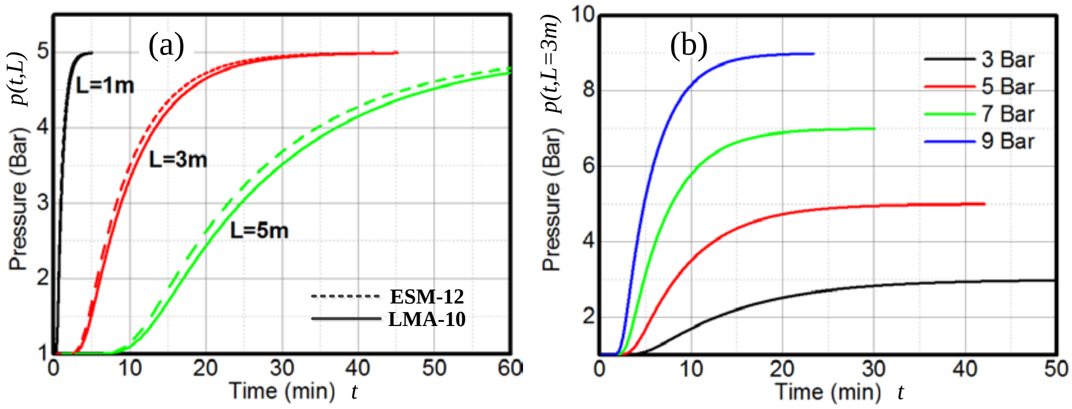

Figure 3.6 The development of gas pressures in PCFs during pressurization process with (a) different length of fibers (p_0=5 Bar), and (b) different applying pressure on LMA-10

These results are useful guidance for the pressurization process. They indicate that the shorter length and higher pressure are helpful to decrease the settling time of pressure in PCFs. The approximate setting time can also be calculated by the theory. However, in experiment, the entrance flow to the air-column of PCF is constrained by the bore size of cone-shaped micro-channel drilled by fs laser pulse. Although the hole-size at the SMF-PCF interface can be optimized to match the column diameter by adjusting the fs laser pulse energy, the sizes for each channel won't be identical. The difference would influence the symmetrical characteristic of structure produced in the following steps. So, the practical settling time in our experiment is slightly longer than the calculated value to guarantee the pressure of all chosen columns reaching the applied value.

3.2.2 Holes inflation and tapering

To expand the holes in PCF, two conditions must be satisfied. Firstly the pressure in air-columns must exceed that set by equation (2.10), and secondly the fiber must be sufficiently heated, that is long enough and hot enough, to allow the expansion to take place. In this part, a slow-and-hot fiber tapering technique is used to heat the selectively pressurized PCF. Inflation of the selected air-columns eventually brings up a local SC structure in fiber. Two different heating methods are adopted to fabricate long and short SC regions.

Tapering with Brushing Oxy-hydrogen Flame

The first method adopts flame-brush as heat source. Figure 3.7 depicts the fabrication platform, where a conventional fiber tapering rig is included. The selectively pressurized PCF is fixed on the translation stages. After the pressure in PCF reach equilibrium, the fiber is tapped with constant flame conditions and pulling rate. During the process, slightly drawing is required to keep fiber straight.

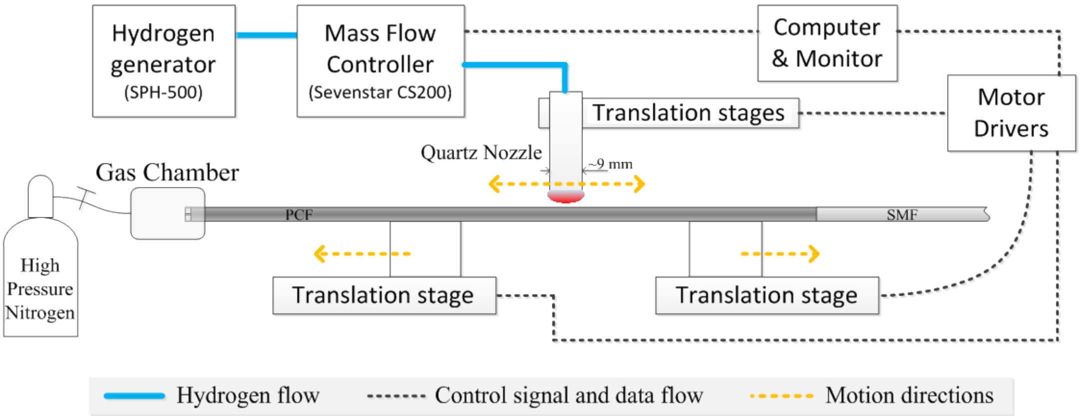

Figure 3.7 Setup for inflation and tapering PCF with brushing flame

The flame temperature is controlled through the hydrogen gas flow rate and nozzle position, which should be adjusted to a moderate level near the fiber's softening point (~1700°C). Because the viscosity of silica changes exponentially at high temperature [16], overheating a pressurized PCF will cause the fiber blow up rapidly. When the flow rate and nozzle position have been defined by experiment, the scanning speed and range of nozzle can fine tune the softening status of fiber by changing the average heating time of the scan region.

As introduced in section 2.2, the collapsing speed of the air-columns in PCF is also dependent on fiber elongation speed during fabrication. With a higher elongation speed, the material flow in transverse direction will decrease [17], and hence the collapse procedure will be slow. Although the unpressurized columns will totally collapse eventually under the combined action of surface tension and pressure from expanding columns, they play important roles in decreasing the confinement loss in transition region.

The expending procedure of the pressurized air-columns in a PCF is more complicated than the unpressurized ones. Generally speaking, the expansion of air-columns is accelerated with the increasing of bore size during the tapering process. The expansion rate of the selected air-columns would be determined by the operation temperature, the axial elongation speed and the gas pressure; and finally impacts on the confinement loss of the transition region. To explain the action of the expansion rate in process, three pieces of PCFs with selective pressurization in air-columns were tapered with same parameters but different pressure, as a result, the expansion of selected air-columns in transition were different.

Figure 3.8 demonstrates the experiment results of the ESM-12 with 3 holes of the innermost ring are pressurized (as (a)). The side view and cross-section micrographs of the microcell transitions are provided from the experiments with 2.5, 3.5 and 6 Bar pressure respectively. The cross-section photos with label 1, 2 and 3 are taken from the corresponding label positions in the side view photos. The positions were purposely chosen at the points where the unpressurized air-columns are completely collapsed (collapse end-point). The sample with a higher pressure applied had a larger hole-expansion at the collapse end-point. Insertion loss of each sample is ~20, ~5 and ~0.2 dB respectively. This could be explained as follow: When a higher pressure is applied, thin struts are formed before the confinement of the collapsing columns become weak. In such a condition, the confinement loss of the transitions can be minimized. Therefore, increasing the pressure in selected air-column can effectively decrease the confinement loss of transitions. However, high pressure may cause the boom the expansion rate, and also challenge the tightness of the pressurization jigs. A pressure of 6-9 Bar is commonly used in my experiments. Increasing the elongation speed is also helpful to decrease the collapsing speed of the unpressurized columns. Meanwhile, the expansion speed will be decreased as well.

More cross-sectional micrographs of the 6Bar sample's transition are provided in figure (b) and (c). These micrographs may represent the development of pressurized holes in fabrication equivalently.

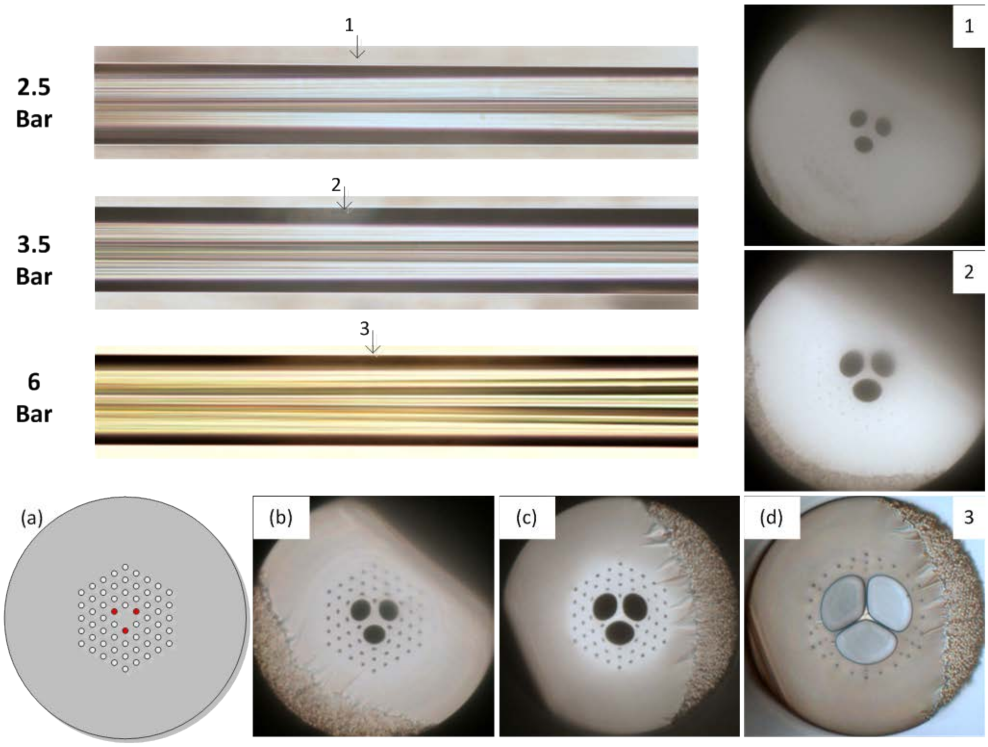

Figure 3.8 Samples of 3-hole cell produced under the pressure 2.5, 3.5 and 6 Bar. The number 1, 2 and 3 represent the positions of corresponding cross-section photos. The shadowed holes in (a) represent the selectively opened PCF holes for pressurization. (b), (c), and (d) are the cross-section photos from a same sample (the 6-Bar one) but different positions

The whole graph of the 6 Bar sample is given in Figure 3.9. The microcell is spindle-shaped due to the difference in heating intervals of each part. At the center of the spindle, the jacket tube has the smallest thickness. However, the transversal dimension of the core in microcell waist region is uniform due to the balanced pressure on the core in all directions. The scan span and speed of nozzle in experiment is 7 mm and 1.5 mm/s respectively. The transmission spectrum of the sample indicates that the transitions are adiabatic. Longer microcells can be made with wider nozzle scan spans. Figure 3.9 (b) is the cross-sectional photo of the microcell at the position near the center of the microcell. At the center position of the microcell, the jacket tube has a smallest thickness. Based on the conservation of material, the thickness is determined by the expansion and the elongation of the cell which are results of the combine effect of pressure, flame temperature, and drawing speed. The highest diameter of the SC region is ~300μm and the smallest thickness of the jacket tube is ~15 μm.

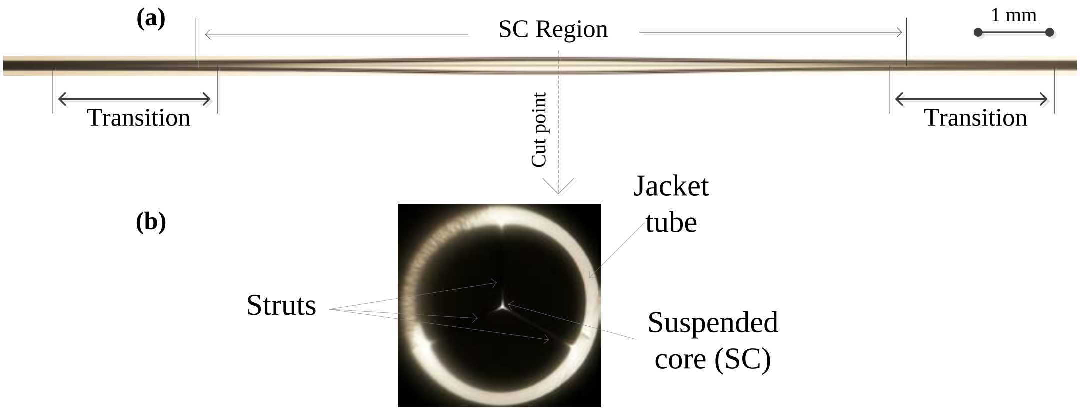

Figure 3.9 (a) Side view photo of a SC microcell produced by brushing flame. (b) The cross-section photo at the position near the maximum

In previous paragraphs, the fabrication of centimeter-level length SC microcells based on brushing flame technique is demonstrated. In the next part, the techniques to fabricate short length microcells will be introduced.

Tapering with electrical arc discharge

The second method adopts electrical arc discharge as heat source. Different to the brushing flame, the heat region of discharge can be restricted in small region while generate a high temperature. By the use of this heat sources, it is possible to produce SC structure region with sub-millimeter length. A programmable fusion splicer Ericsson FSU-975 is used in my experiments to generate electrical discharges. Procedure of this method can be explained with the aid of Figure 3.10. A selectively pressurized PCF is fixed on the fiber clamps of the splicer and then pressurized with dry nitrogen at up to 9Bar pressure. After the pressure in PCF reach equilibrium, the fiber is tapped with constant discharge current and pulling speeds.

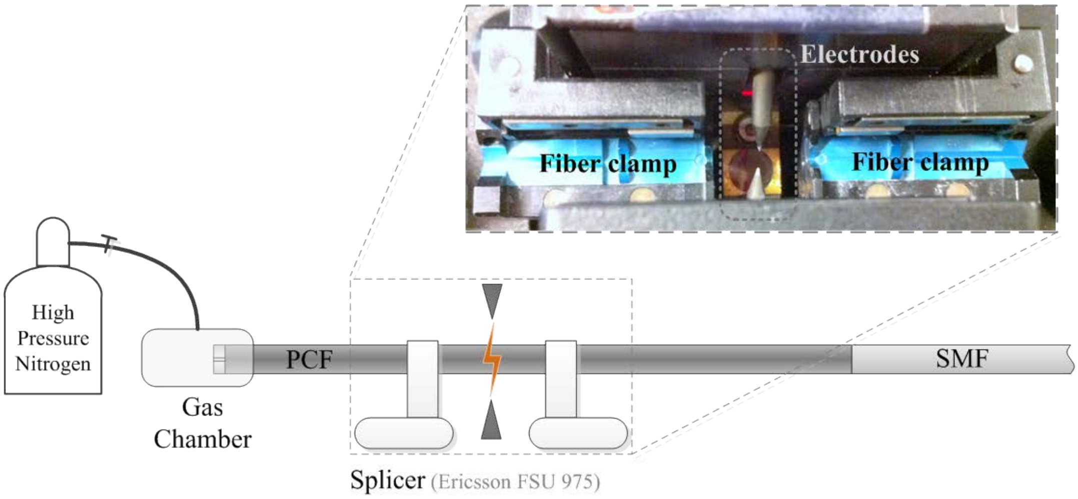

Figure 3.10 Setup for inflating and tapering PCF with electrical arc discharge

The discharges produced by the splicer modify the PCF by thermal effect. Since it operates with milliamp level current, the arcs produced by splicer are located in the glow discharge region. The Current flow between electrodes heats the surroundings via thermal radiation and convection.

The heating profile of the glow discharge between two pairs of electrodes has been analyzed by measuring the optical intensity of the discharge [18]. Based on the measurement results, the equation of current density of discharge is generalized as (3.10)

$$\begin{aligned} i(r,z) &= \frac{I_{tot}}{2\pi\sigma_d^2(z)}\exp\left(-\frac{r^2}{2\sigma_d^2(z)}\right), \\ \sigma_d(z) &= \sigma_0(1+Cz^2)^{-1/3} \end{aligned} \tag{3.10}$$

where z is the direction along the axis of two electrodes, $r=(x^2+y^2)^{1/2}$. I_{tot} is the total current of discharge, $\sigma_d(z)$ and σ_0 are the Gaussian characteristic width at position z and z=0 respectively. C is a constant represent the variation of the radiative intensity in the z-direction. The distribution at x-z plan is provided in Figure 3.11. The discharge arc is hottest at the electrode tips. The 3D distribution of current density is circular symmetry about the z-axis, so for arbitrary x-y plan along the z-axis, the arc is hottest at the point r = 0. Actually temperature in a discharge region is proportional to the square of current density, so the temperature between the electrodes features a similar distribution described by equation(3.10). [19]

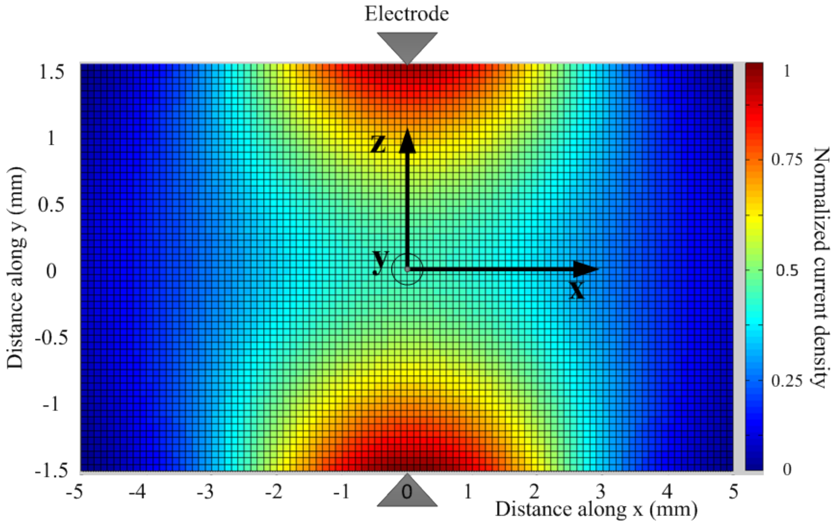

Figure 3.11 The current density distribution of between discharging electrodes

In my experiment, the PCF is placed along the x axis, where the profile of temperature distribution is Gaussian. Compared to brushing flame technique, the electrical discharge has a much small heat region and a large temperature gradient. These features enable the possibility of producing microcells with length as small as 600µm by use of electrical discharge. It also brings difficulties in controlling the temperature because the viscosity of silica changes greatly after softening point.

The discharge parameters given in Table 3.2 are the typical values used in tapering ESM-12 PCF with 5 Bar pressure applied to the 3 columns of innermost ring (as illustrated in Figure 3.8(a)). When core columns are pressurized, the discharge time, current at step 2, which is the major step for heating, should be slightly decreased to avoid a fast expansion.

Table 3.2 The typical discharge parameters in FSU975 for SC microcell fabrication on ESM-12 with 5Bar applying pressure

Pre-discharge	Step 1	Step 2	Step 3	Re-discharge

time	currents	time	Currents	time	currents	time	currents	
s	mA	s	mA	s	mA	s	mA	times
0.1	9	0.2	10	0.3	11.6	0.3	10	5

Based on the parameters in Table 3.2, the SC microcell with ~300 μm SC region and ~200 μm transitions can be fabricated (Figure 3.12).

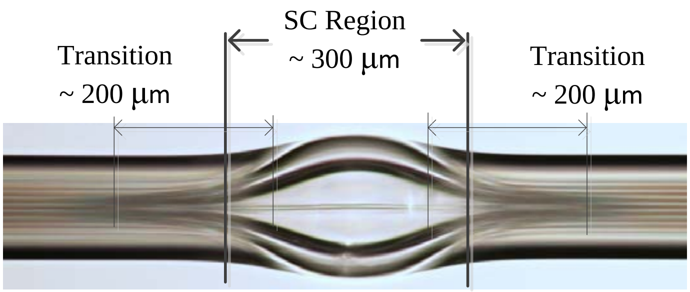

Figure 3.12   Side-view photo of a SC microcell produced by electrical discharges

3.2.3 Transverse pressurization

With the method introduced in previous text for microcell fabrication, one end of the PCF is used as the entrance for gas, thus the optical transmission properties of the microcells in fabrication can only be measured by cutting and splicing the entrance-end of PCF to a SMF when the whole process is finished. However, the quality variance of splicing points would influence the measurement accuracy of the microcell. An in-situ measurement during the process would be practically useful in accurately measuring the properties of microcell and efficiently screen out the optimal fabrication parameters.

To realized the real-time measurement, the transversely pressurization method was proposed and adopted in fabrication the microcells. The method contains following steps, at first, a microcell is produced near one end of a long PCF. The expansion of the cell is high to minimize the thickness of jacket tube. Then, small holes are drilled on the jacket tube towards each chamber of the microcell by focused fs laser pulses. All air-columns except the pressurized ones are collapse in the SC region of cell. The new channels in the jacket tube will not impede the light transmission in the core, and serve as the entrances of gas pressure in duplicating the initial microcell.

The experimental setup is given in Figure 3.13. Three micro-holes (5μm diameter) were opened on the SC microcell with only ~0.1 dB loss at wavelength of ~1550nm. The loss would arise from the scattering caused by the debris attached near the microcell's core. To minimize debris, which is the byproduct of fs laser drilling, the microcells are recommended to be expanded larger to form a thin jacket tube. The processed cell was then sealed in a three ports gas chamber and gas pressure was imposed to the chamber from one port.

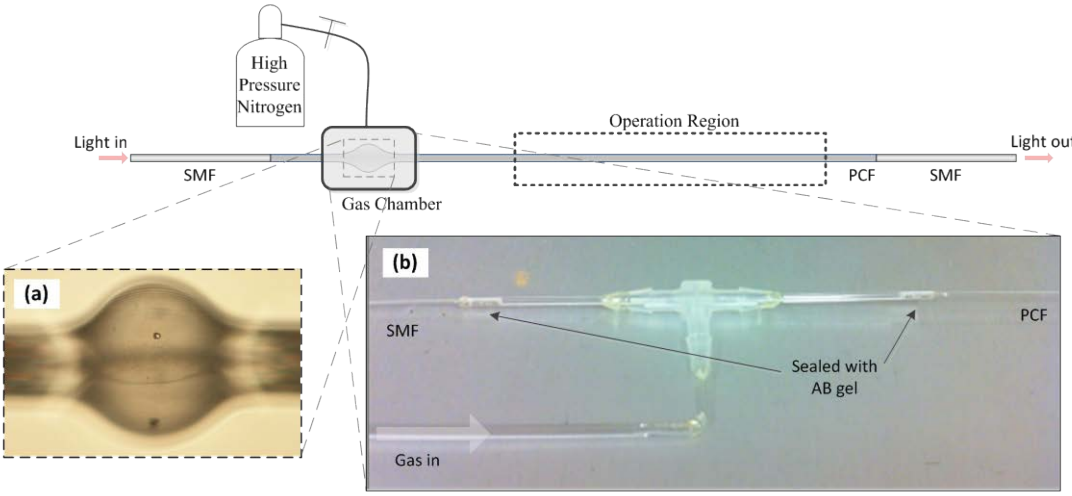

Figure 3.13 Experimental setup for selectively transverse pressurization. (a) Micrograph of the microcell with side holes opened by fs laser; (b) 3-port Gas chamber for pressurization

The transverse pressurization technique provides a method to access each chamber in the microcell from its lateral direction. The feature would be useful for fast-response fiber sensing and in selective infiltration applications. Compared with other side-opening techniques for solid core MOFs [20-22], this technique is highly dynamic in accessing the interior structure of fiber with very low insertion loss. In the applications of microcells discussed in Chapter 5 and 6, this technique will be used in infiltrating RI index oil and laser dye solution into microcell.

3.2.4 PCF Splicing with holes in alignment

After the fabrication of each microcell, the sample is cut from the other part of the PCF, so the initial pressurized PCF from which the microcell is made will be used up ultimately. Extending the pressurized PCF would be useful to avoid repeating the selective opening and sealing processes.

The splicing between two identical PCFs can be realized with similar parameters for PCF-SMF splicing. The optimized splicing parameters used in my experiments with splicer Ericsson FSU-975 are given in Table 3.3. For the PCF-to-PCF splicing, slightly decreasing the offset and fusion time is required to minimize the holes deformation in Fiber 1. The typical insertion loss of each splicing point is ~0.5 dB at wavelength around 1550nm.

Table 3.3 Optimized parameters for splicing between SMF-28 and LMA-10

Fusion type			SMF-SMF	SMF-PCF	PCF-PCF
Fiber 1			SMF-28	SMF-28 [23]	LMA-10
Fiber 2			SMF-28	LMA-10	LMA-10
Per fusion	Time	s	0.2	0.2	0.2
	current	mA	10	5	5
Fusion 1	Time	s	0.3	0	0
	current	mA	10.5	-	-
Fusion 2	Time	s	2	0.3	0.2
	current	mA	16.3	12	12
Fusion 3	Time	s	2	0	0
	current	mA	12.5	-	-
Gap		μm	50	50	50
Overlap		μm	10	5	5
Offset		μm	0	50	45

In a normal splicing between PCFs, the adjustment on fibers in the azimuthal direction is unnecessary because of the degeneracy of the fundamental mode. [24]

however, in my experiment, the purpose of the splicing is not only mechanical and optical connection, but also to extend the pressure channels from the processed PCF to a normal PCF segment with the same pattern. Thus the PCFs must be spliced with holes, at least the selectively opened holes, in alignment. The 'hole-to-hole' splicing can be realized by adjusting the azimuthal angle of PCFs during splicing. As demonstrated in Figure 3.14, the azimuthal deviation should be limited in a range to realize the hole-to-hole splicing.

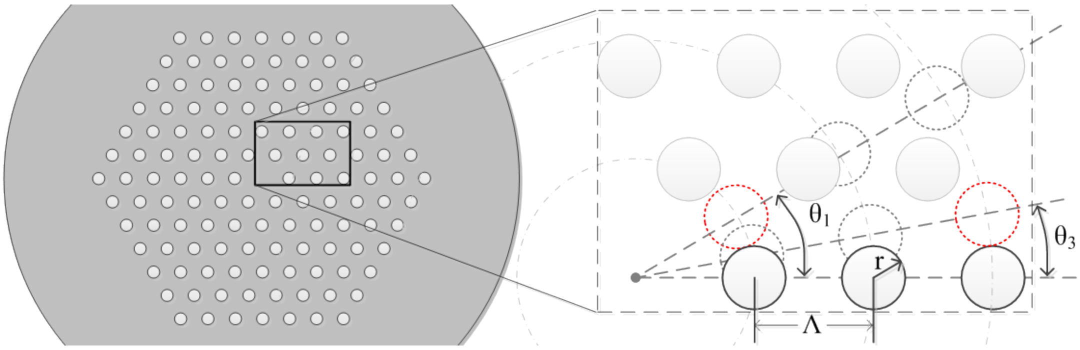

Figure 3.14 The maximum deviation angles for the PCF splicing with holes of different layers in alignment. The solid circles refer to the air holes of one PCF end, and the dash circles refer to the air holes of the other PCF end

According to the simple geometry relation between holes in the PCFs, the maximum deviation angles θ_n could be calculated by equation (3.11) for each layer of the holes.

$$\theta_n = 2\arcsin(r / n\Lambda) \tag{3.11}$$

where r and Λ are the radius and pitch of the holes in PCF, n represent the layer where the holes located. The maximum deviation angles of LMA-10 and ESM-12 are calculated. The results are listed in Table 3.4.

Table 3.4 The maximum deviation angles for the holes of each layer in PCF LMA-10 and ESM-12

Fiber	Λ	r	θ_1	θ_2	θ_3	θ_4	θ_5	θ_6
	μm		degree					

LMA-10	7.2	1.69	27.2	13.5	9	6.7	5.4	4.5
ESM-12	7.5	1.75	27	13.4	8.9	6.7	5.3	4.5

The widely used accurate azimuthal alignment with power meter feedback for splicing high birefringence (HiBi) fibers might not be feasible for PCF hole-to-hole splicing, because the 6-fold symmetrical PCFs are degenerate and there are no power variation while rotating the fiber.

The side scattering techniques could be used to estimate the azimuthal status of fiber during the splicing process. In this technique, the fiber is illuminated transversely from one side. The light passing through the fiber would be scattered when encountered the interior structure of fiber. At the other side of fiber, a detector is located with a fixed angle towards the light source to measure the intensity of the scattered light. Rotation of fiber will cause the intensity variance at detector. The technique has been used to probe the interior structure of step index fibers, HiBi fibers, and MOFs. [25-27]

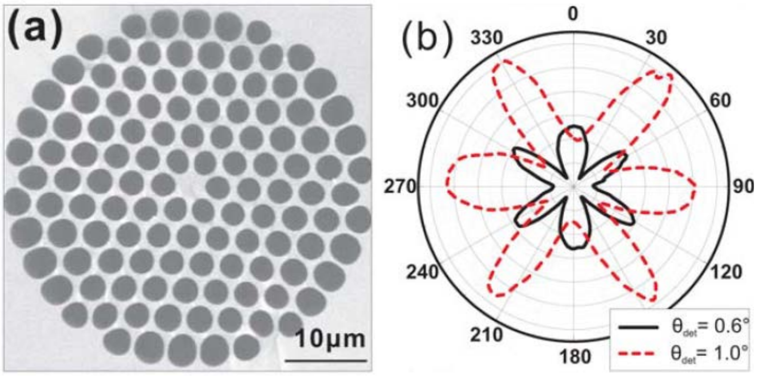

Figure 3.15 (a) SEM micrograph of a solid core PCF; (b) The scattering patterns with different detection angles for the PCF [26]

Figure 3.15 (b) shows the pattern of the scattered light intensity recorded by a detector when a PCF is rotated a circle. The θ_{det} represents the angle of detector towards the incident light and perpendicular to the fiber axis. The PCF possess a 6-fold symmetrical structure as given in Figure 3.15 (a). In the detection pattern, the six high intensity peaks corresponding to the six-fold symmetrical structure can be found in a whole circle rotation. The interval of each peak is ~60° and the signal will decay rapidly with ~10° after each peak. The results indicate that the technique can accurately orient the azimuthal angle of a PCF, and could be applied in the hole-to-hole splicing between PCFs.

In the most fiber fusion splicer, there are two pairs of cameras and light source located in perpendicular to each other to observe the angle of fiber-ends. When a PCF is put into the field of either camera and rotated then. Bright lines can be observed at some rotation angles. The bright line corresponds to the intensity peak in Figure 3.15 (b). When a bright line is observed in PCF located in the splicer from one camera, the PCF must be dark from the other camera. However in the most fusion splicers, the intensity can only estimate from the image captured by the cameras, this limits the accuracy of the fiber azimuthal orientation to ~10°. Compared to the calculation result in Table 3.4, the accuracy is enough for the PCF splicing with holes of the two layers closest to the core in alignment. More accurate hole-to-hole fusion splicing can be realized by marking the fiber under optical microscope.

Figure 3.16 (a) is the result of hole-to-hole splicing in LMA-10 by visual inspection. As demonstrated in Figure 3.16 (b), the connectivity of the air-columns can be checked by selectively pressurizing the innermost 3 holes of the right PCF as Figure 3.16 (c), and then conducting electrical discharges on the other PCF. To facilitate the comparison, we conducted discharges on both sides of the splicing point. The identical microcells on both sides indicate that the hole-to-hole splicing is successful.

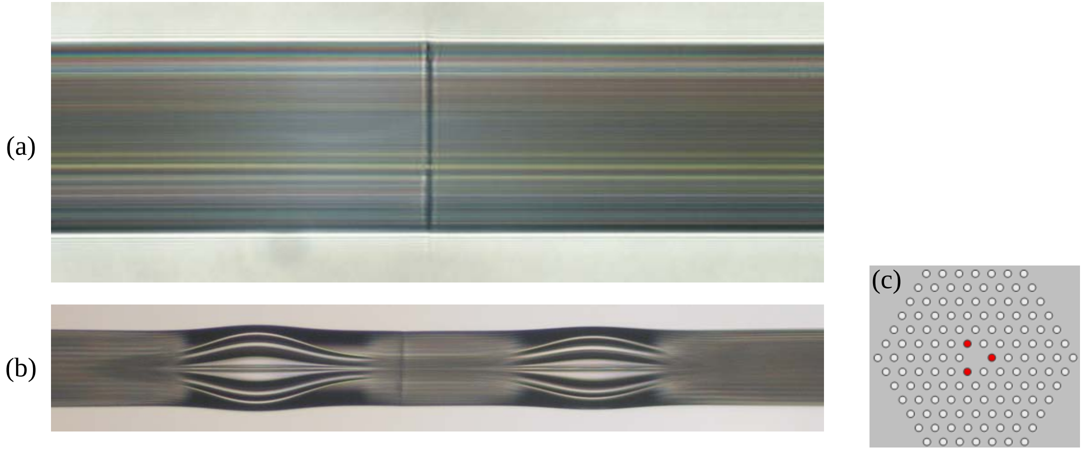

Figure 3.16 (a) The result of a successful hole-to-hole splicing; (b) Verification the result of the hole-to-hole splicing by locally discharging the PCF on both sides of the splicing point; (c) The pressurization pattern of the PCF in (b)

3.3 SC Microcells

By selecting different holes combination in fabrication, SC microcells with different internal structure have been experimentally realized. In this section, six types of microcells will be demonstrated, and three of them will be simulated and discussed in detail.

3.3.1 Cross-section morphology

The longitudinal shape of SC microcell has been demonstrated in section 3.2.2. The length of microcell is majorly controlled by the heater size, the scanning length with some slight adjustment on the other tapering parameters. In this part, the discussion is majorly conducted on the microcells’ cross-sectional morphology which would determine their optical properties, such as mode distribution, birefringence, and evanescent field.

The cross-sectional morphology of a microcell is the result of the combined action of pressurized air-columns to the other portions of a PCF under high temperature. Therefore the selection of air-columns in fabrication is the key in building microcells with different structures. The chosen air-columns in PCF must be symmetrical to the fiber axis to guarantee that pressure forces on the core are balanced in all direction. As a result, the modified fiber core will be suspended in cell with thin struts connecting to the jacket tube, while the other portions will be pushed apart from the center. Figure 3.17 demonstrate the cross-section micrographs of the microcells fabricated by inflating air-columns located at the innermost circles in PCF. The first column in Figure 3.17 is the diagrams of holes-selection on PCF. The dark holes represent the pressurized holes in fabrication. The second column is the micrographs of the selective opened PCF end which are used as the gas entrances for selective pressurization. The third and fourth columns are the cross-section micrographs of transition regions and SC regions of the microcells.

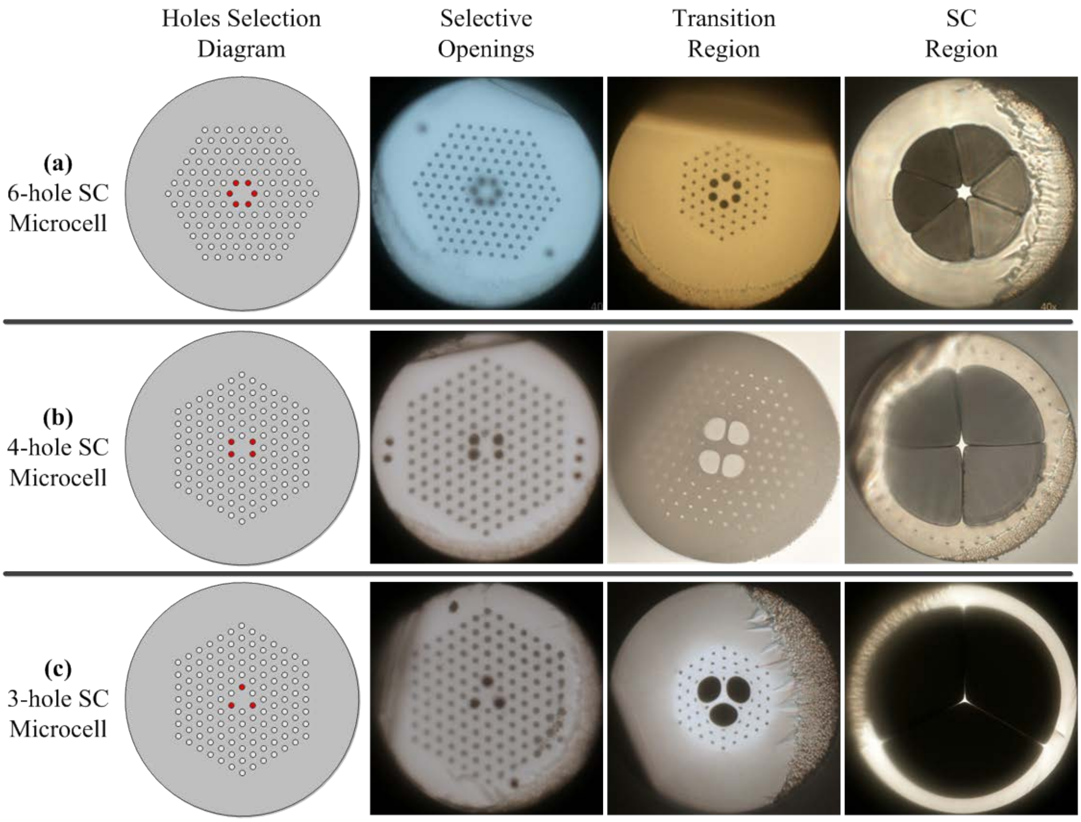

Figure 3.17 Diagrams and micrographs of the 6-, 4- and 3-hole microcell

samples inflation air-columns of the 1st layers from the center in PCF

In Figure 3.17 (a), the innermost 6 holes are selectively opened and pressurized in the process. The final structure of SC region is similar to the grapefruit fiber in geometry. Differently, The grapefruit fiber typically contains a Ge-doped core to ensure efficient coupling to standard SMFs [28], while this type of SC microcell have an all silica core. The connection problem is solved automatically by the transition regions. In Figure 3.17 (b), all air-columns except two opposite ones in the innermost layer are selectively inflated. In the transition regions the gradually collapsing air-columns which are not pressurized will automatically suppress the confinement losses until the generation of thin struts. The final structure of SC region is similar to the four holes SCF developed by IPHT in ~2010 [29]. However, the core of microcell possesses much a higher length-width ratio. As a result, the birefringence of the microcell is very high. In Figure 3.17 (c), three holes of the innermost layer are symmetrically selected and inflated. The final structure of SC region is similar to the steering-wheel fiber [30]. To make a clear discussion, in following sections, the SC microcell with cross-section structure of as Figure 3.17 (a), (b) and (c) will be named as the 6-hole, 4-hole and 3-hole SC microcell respectively. Further discussion on the properties and applications of these three kinds of SC microcell will be conducted in the next section and Chapter 4, 5 and 6.

By additional opening the air-columns of the second layer, more interesting microcell structures can be produced. Figure 3.18 provide three examples of such kind of microcells.

In Figure 3.18 (a), two additional holes besides the ones of the innermost ring are selected. Compared to the 6-hole microcell in Figure 3.17 (a), the microcell fabricated with this hole-selection pattern has a two-fold symmetrical core and two additional cores along a length of the fiber. The distances between the cores are a fixed value of ~10 μm. An inline interferometer could be formed by closing the cores with additional tapering process. Figure 3.18 (b) proposes the microcell with 3 uniform cores. A similar structure can be found in [31]. Figure 3.18 (c) exhibits the microcell with larger scale core by selectively inflation all air-columns in the second layer.

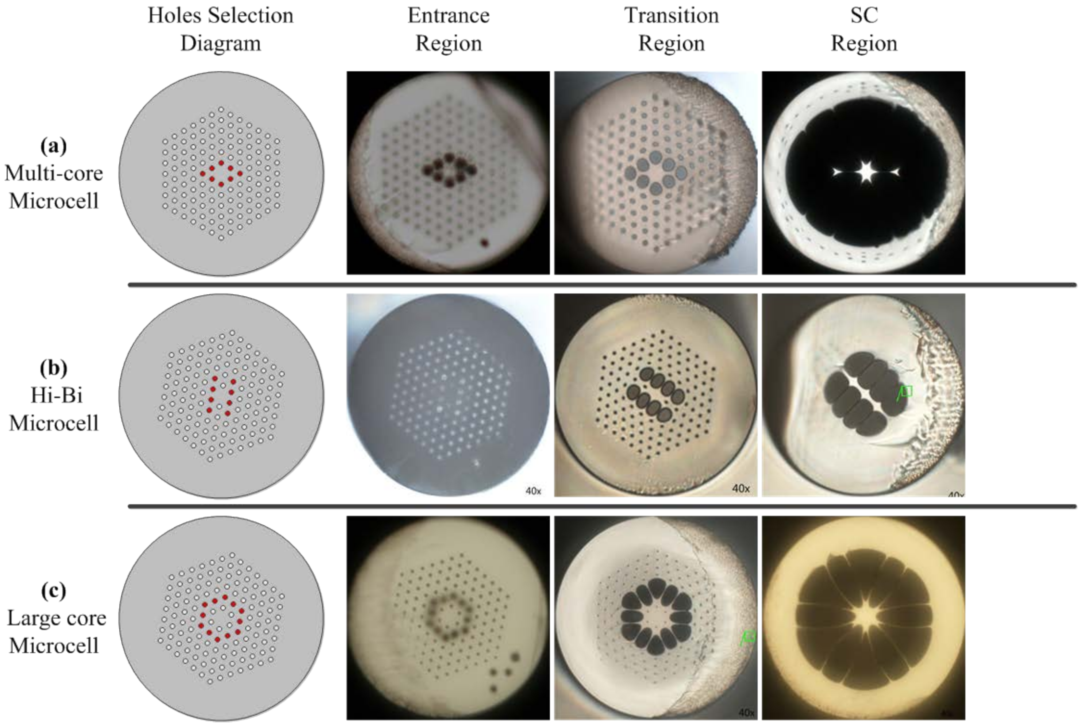

Figure 3.18 Diagrams and micrographs of the microcell samples by selective inflating the air-columns of the 1st and 2nd layers in PCF

Six types of SC microcells fabricated by selective inflating air-columns located at the first or second layer of a PCF are demonstrated in previous paragraphs. There are still more possibilities on microcells structure by choosing different air-columns in PCF. Compared to the fibers with SC structures produced by other method, such as stack and draw, extrusion, the SC microcells possess unique properties of large holey region and thin jacket tube. The diameter ratio of holey region to core (DRHC) of microcell can reach a value up to ~80. These properties are hard to be realized with usual MOF fabrication methods, because, for the stack and draw method, it means that the capillaries used in fabrication should have an impractical thin sidewall; for the extrusion or ultrasonic drilling method, realizing a cane with thin jacket tube as well as long enough for the large holey region is still difficult so far. Although, SCF with DRHC ≈ 62, which is close to the value of microcell, can be produced with a modified fiber-drawing technique, [32] the jacket tube thickness (~40 μm) of the fiber is still thicker than microcell's (~15 μm).

The large holey region and thin jacket tube are important to SCF for the following reasons. Firstly, the cutoff wavelength of SCF is shifted to longer wavelength with the increase of DRHC. So the fiber with large DRHC can propagate light in a wider wavelength range. Secondly, large holey region is significant for the fiber's applications in evanescent field sensing because of the large light-matter interaction region. [32] Thirdly, the material infiltration into the holey region from fiber-top SCF is easier for a larger entrance. Additionally, the thin jacket tube facilitates side-accessing fiber interior structure with physical or mechanical methods, such as fs laser machining, FIB milling, HF etching, and polishing. Some interesting applications of the SC microcells in optical sensing and building photonic devices have been found and will be introduced in Chapter 4, 5, and 6.

It is worth noting that, with current facilities in our laboratory, the minimum core size of the microcells can be achieved is ~1.6 μm in diameter. Further decreasing on the core diameter might be restricted by nozzle size and scanning trajectory in current fiber taper system. The possible methods to overcome the constraints have been investigated, and some suggestions have been proposed in the future works section. In the next two parts, properties of the microcells fabricated by selectively inflating the air-columns of PCF innermost ring will be discussed base on the simulation results.

3.3.2 Modal properties

The modes in optical fiber are the EM field distributions of the guided light ray with discrete propagation angles. The mode fields can be determined by solving the wave equations derived from Maxwell's equation with different boundary conditions. The modes in an optical fiber consists of the TE modes with $E_z=0$, the TM modes with $H_z=0$ and the hybrid modes $E_z \neq 0$, $H_z \neq 0$, where E_z, H_z represent the electric and magnetic field in the propagation direction respectively.

For the conventional SMF with cylinder waveguide and step-index RI distribution, the proper solutions for mode fields in the core and cladding are the 0th-order Bessel function and the modified Bessel functions of the second kind respectively. The propagation constant β of each mode in a fiber can be determined from its geometry and material properties (normally represented by the V-value) by solving the dispersion equation which is a combination of wave equations for the core and the cladding region under the continuity condition of both electric and magnetic fields at the core-cladding boundary. [33]

The intensity and field distributions of fundamental mode and some nearest high-order modes in SMF are given in Figure 3.19. The LP modes are approximate modes classified by the eigenvalues of dispersion equation under the weakly guide approximation ($n_{core} \approx n_{cladding}$).The dispersion diagram of some low-order modes of a SMF has been provided in Figure 2.7.

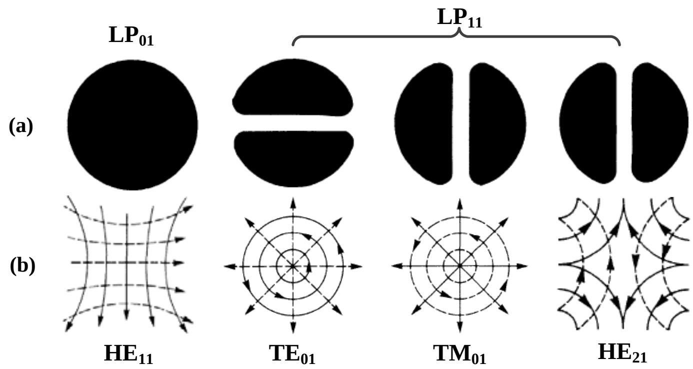

Figure 3.19 Intensity and field distribution of the LP_{01} and LP_{11} modes in conventional step-index fibers. (a) intensity of E_x, and (b) electric (solid line) and magnetic (dash line) field vectors [34]

For the SCFs, the cladding region is constructed by the struts and the surrounded air region. The weak guide assumption is violated in the fiber due to the large RI differences between the dominant air regions and the core material (pure silica). Also, the irregular core-cladding boundary in the SCFs makes the dispersion relation calculation of the SCFs more complicated than that of the SMFs. It's hard to find the analytic solutions for the dispersion equation of the SCFs. Normally, the propagation constant of the modes in SCFs are solved with some numerical methods, such as finite element method (FEM) [35], finite difference method (FDM) [36]. The FEM is adopted in calculating the propagation constants and the field distributions of the supported modes in SC microcells.

Before conducting the FEM simulation, several models have been set up for the microcells based on the micrographs. As illustrated in Figure 3.20, the core of 6-hole microcell is modeled by the gray region surrounded by six identical circles with ~300 nm spacing between each two of them. To reflect the action of the corners of the irregular core, an effective radius r_{eff} is always adopted to represent the core radius of SCFs [37]. Area of circle with radius r_{eff} is same to that of irregular core region. The calculated scale relation between fiber core and its equivalent circle is given by (3.12).

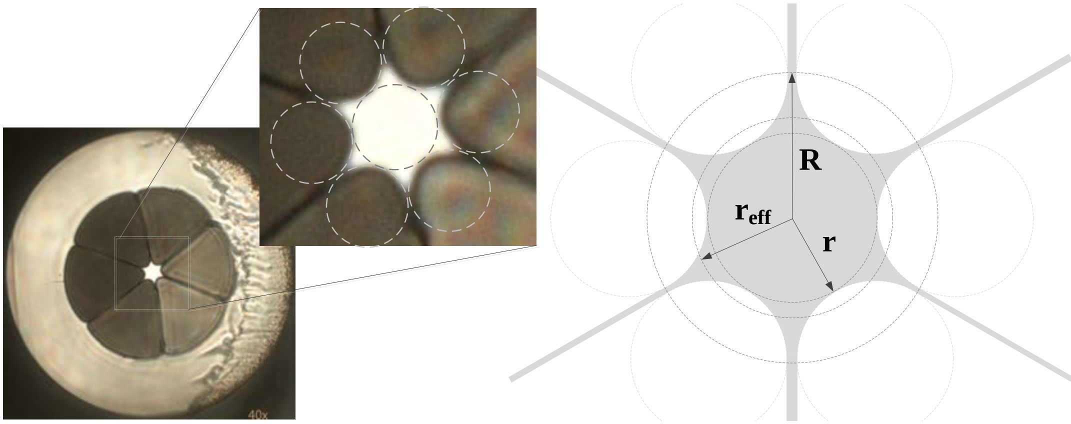

Figure 3.20 Model of the 6-holes SC microcell's core region

$$R \approx 1.463 r_{eff} \tag{3.12}$$

where R is radius of a circle perpendicular to the six identical circles. The circle with radius R defines the boundary of core region. r_{eff} is radius of the equivalent circle.

As illustrated in Figure 3.21, the core of 4-hole microcell is modeled by the gray region surrounded by four identical ellipses with the ~300 nm spacing which represents the strut region. From the micrograph in Figure 3.21, the long axis length A of the rhombus-like core is ~ 2.1 times longer than the length of short axis B, i.e. $A \simeq 2.1B$. The ratio is almost fixed for all 4-hole microcells. Similar to the 6-hole microcell, an equivalent ellipse may be defined to represent the solid region of fiber core. The calculated relation between fiber core and its equivalent ellipse is given by (3.13).

$$A \approx 1.772 a_{eff}, \quad B \approx 1.772 b_{eff} \tag{3.13}$$

where a_{eff} and b_{eff} are the length of major semi-axis and minor semi-axis respectively. An effective radius $r_{eff} = \sqrt{a_{eff} \times b_{eff}}$ is defined to represent the equivalent dimension of the core.

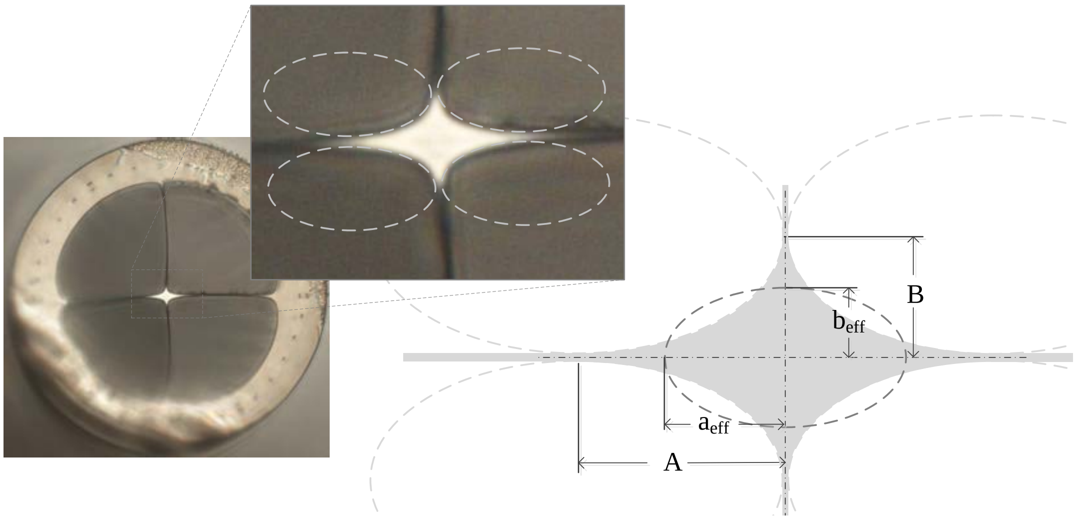

Figure 3.21 Model of the 4-holes SC microcell's core region

As illustrated in Figure 3.22, the core of 3-hole microcell is modeled by the region surrounded by three identical circles with the ~300nm spacing. An equivalent circle is defined to represent the solid region of fiber core. The calculated relation between fiber core and its equivalent is given by(3.14).

$$R \approx 2.339r_{eff} \tag{3.14}$$

where R is radius of a circle perpendicular to the three identical circles. The circle with radius R defines the boundary of core region. r_{eff} is radius of the equivalent circle.

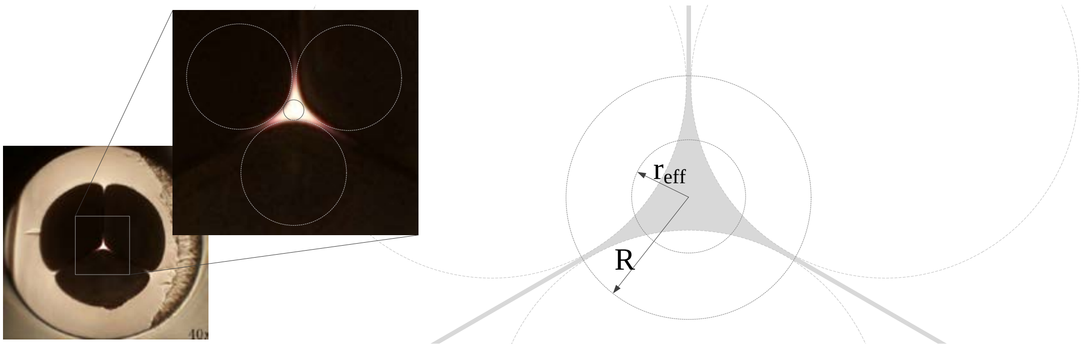

Figure 3.22 Model of the 3-holes SC microcell's core region

Since the Maxwell's equations are independent of the relative size of fiber core to the wavelength λ. The dimension of the core region, for example r, can be normalized as r/λ (normalized frequency), which would provide more information about wider class of structure. [38] Due to the small longitudinal scale of the microcells, neither material dispersion nor material attenuation is taken into consideration.

Figure 3.23 shows the fundamental modes of the 6-, 4- and 3-hole SC microcells, which are calculated by FEM with λ = 1550 nm, $r_{eff} \approx 3\mu m$ are provided in Figure 3.23. The colors in the fiber core represent the time average strength of power flow at axial direction. Most of the power is confined in the silica region for the microcells in this scale. The arrows represent the electric field vectors. Since the 6- and 3-hole microcell contain the 6- and 3- folds rotational symmetrical structures, the distributions in row (a) are the perfect rotation of corresponding distributions in row (b), i.e. the fundamental modes are degenerate in 6 and 3-hole microcell. [24] For the 4-hole microcell which possesses the 2-fold rotational symmetrical structures, existence of birefringence in the core can be predicted.

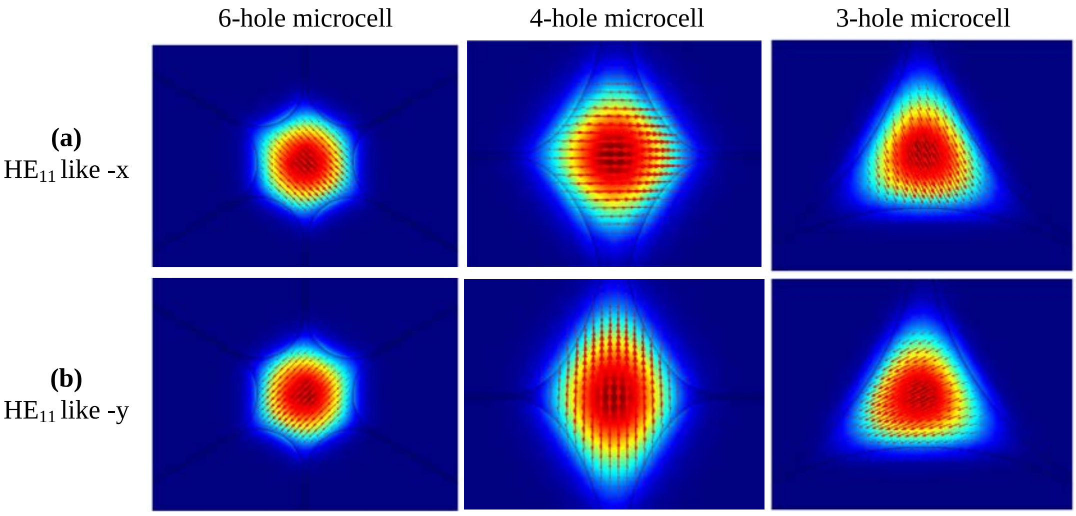

Figure 3.23 Simulated fundamental mode profiles and electric field vectors distributions of the 6-, 4- and 3-hole SC microcells

Figure 3.24 shows some high order modes closest to the fundamental mode in SC microcells. Following the name of modes in SMF, they are named TE_{01}, TM_{01},

HE_{21}-like respectively. Due to the similar field distribution, they could be classified into LP_{11}-like group. Obviously, the LP_{11}-like modes are not degenerate even for 6- and 3-hole microcells.

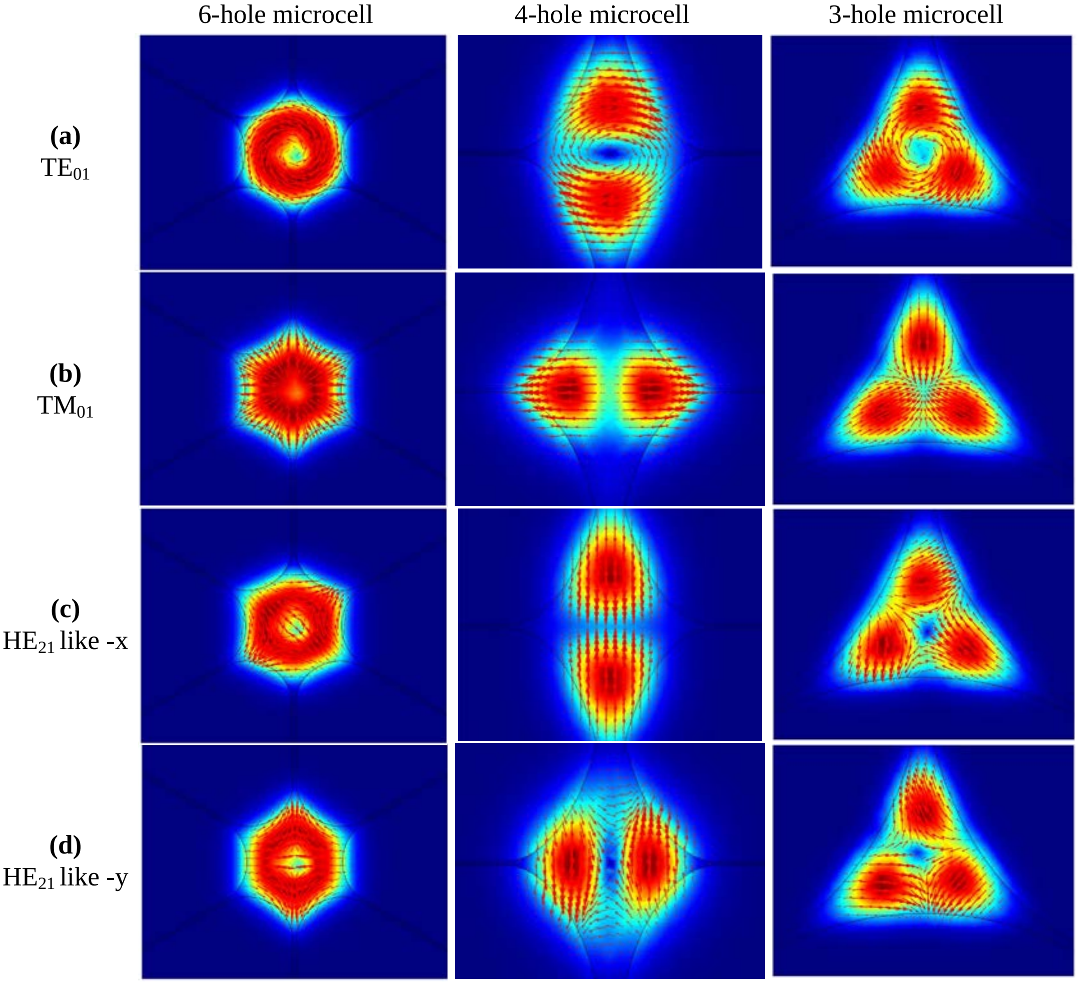

Figure 3.24 Simulated LP_{11}-like mode profiles and electric field vectors distributions of the 6-, 4-, and 3-hole SC microcells

In order to obtain a better visualization of the mode degeneration, birefringence and cutoff condition that occur in the microcell, the normalized propagation constant β_N given by equation (3.15), is introduced based on the definition in standard fiber techniques.

$$\beta_N = \frac{(\beta_{eff} / k_0) - n_{cl}}{n_{co} - n_{cl}} = \frac{n_{eff} - n_{cl}}{n_{co} - n_{cl}} \tag{3.15}$$

where β_{eff}, k_0 represent the effective propagation constant and the vacuum wavenumber of the mode respectively. The n_{co} = 1.44462 is the RI of the core was assumed to be a constant value. n_{cl} = 1 is the RI of the cladding region. The impact from struts is neglected because of the relative small scale to the holey region. n_{eff} is the effective RI calculated by the FEM software. Figure 3.25 provide the simulated dispersion curves of the 6-, 4- and 3-hole SC microcells respectively. The split of the LP_{11} like modes can be clearly observed. In Figure 3.25 (b) the separation in β_N between two polarization states of the fundamental mode, i.e. the birefringence can be obtained quantitatively. The birefringence tends to vanish while the normalized frequency approaches the cutoff value. Further discussion on the birefringence and its applications of 4-hole microcell will be conducted in Chapter 5. The cutoff frequencies of the fundamental mode /LP_{11}-like modes for each microcell are ~0.1/0.3 (6-hole microcell), ~0.1/0.18 (4-hole microcell) and ~0.12/0.32 (3-hole microcell).

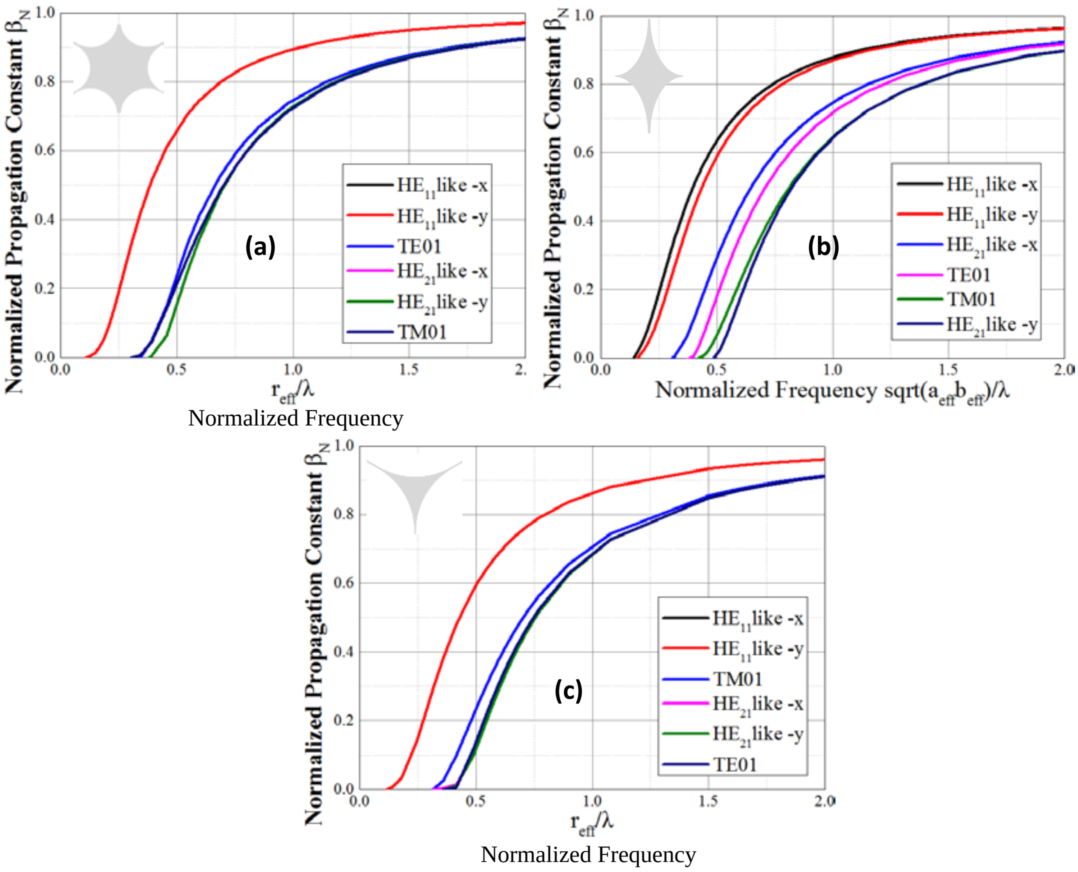

Figure 3.25 Dispersion curves of the (a) 6-hole, (b) 4-hole, (c) 3-holes SC microcells

3.3.3 The fraction of power in the air-columns

The curves of normalized propagation constant in Figure 3.25 tend to be zero with decreasing normalized frequency. As a result, the modes will be weakly bound to the fiber core and more and more power propagates in the evanescent field. The fraction of the propagating power inside the air-columns could be obtained from the surface integrals of Poynting component in the propagation direction S_z over difference region in fiber cross-section.

$$\eta_H = \frac{P_{hole}}{P_{all}} \times 100\% = \frac{\iint_{A_{hole}} S_z dA}{\iint_{A_{core}} S_z dA + \iint_{A_{strut}} S_z dA + \iint_{A_{hole}} S_z dA} \times 100\% \quad (3.16)$$

where A_{core}, A_{strut}, A_{hole} represent the surface of core, struts and holes in cross-section respectively. The time average of the power flow through the area A is given by equation (3.17).

$$\begin{aligned} P &= \iint_A \langle S_z \rangle dA = \iint_A \frac{1}{2}\mathrm{Re}\left\{\left(E\times H^*\right)\cdot u_z\right\} dA \\ &= \iint_A \frac{1}{2}\mathrm{Re}\left\{\left(E_x H_y^* - E_y H_x^*\right)\cdot u_z\right\} dxdy \end{aligned} \tag{3.17}$$

where < >, * denote the time average on expression and the complex conjugate respectively. u_z is the unit vector along the power flow direction. In the analysis of optical waveguides, u_z is the axial direction of fiber. E and H are the complex magnitude of the electric and magnetic field.

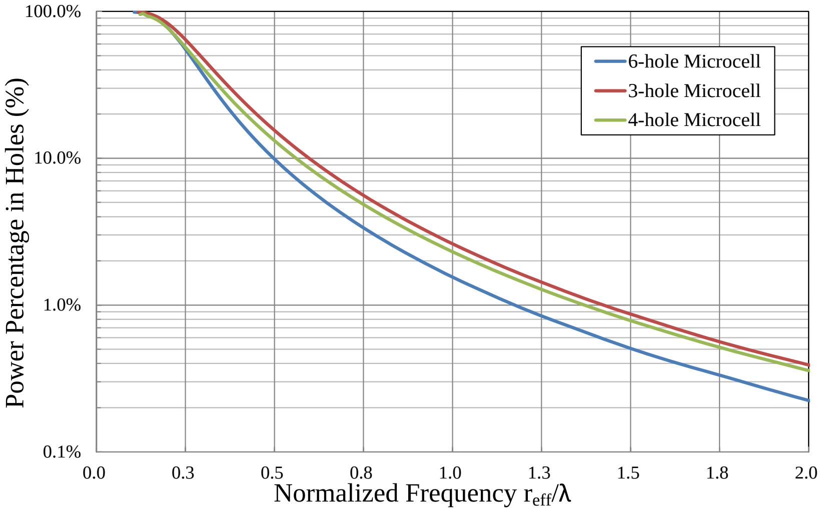

Figure 3.26 Power fraction of the fundamental mode located in the holey region of three different SC microcells

As shown in Figure 3.26, the fraction of power in the holy region of microcells increases with the decrease of the normalized frequency. As a result, microcells with smaller core dimension would enhance the performance in applications of light-matter interaction based on evanescent field.

3.4 Summary

In this Chapter, the fabrication of a novel in-fiber cell by post-processing a commercial PCF has been discussed with details of the critical steps. Six types of low-loss SC in-line structures with small core, large air filling fraction and thin jacket tube are reported for the first time. Based on its structure, the in-fiber cell is named as SC microcell. The SC microcell is diverse in structure and features a number of outstanding optical and mechanical properties, such as low-loss interconnection to standard fiber system, strong confinement, large evanescent fields and robust structures. Three types of microcells have been modeled and numerically analyzed.

3.5 References

[1]. J. Canning, M. Stevenson, T. Yip, S. Lim, and C. Martelli, "White light sources based on multiple precision selective micro-filling of structured optical waveguides," Optics Express **16**, 15700-15708 (2008).

[2]. Y. Wang, S. Liu, X. Tan, and W. Jin, "Selective-fluid-filling technique of microstructured optical fibers," Journal of Lightwave Technology **28**, 3193-3196 (2010).

[3]. C. Martelli, J. Canning, K. Lyytikainen, and N. Groothoff, "Water-core Fresnel fiber," Opt. Express **13**, 3890-3895 (2005).

[4]. B. T. Kuhlmey, B. J. Eggleton, and D. K. Wu, "Fluid-filled solid-core photonic bandgap fibers," Journal of Lightwave Technology **27**, 1617-1630 (2009).

[5]. R. M. Gerosa, D. H. Spadoti, C. J. de Matos, L. d. S. Menezes, and M. A. Franco, "Efficient and short-range light coupling to index-matched liquid-filled hole in a solid-core photonic crystal fiber," Optics Express **19**, 24687-24698 (2011).

[6]. M. Vieweg, T. Gissibl, S. Pricking, B. Kuhlmey, D. Wu, B. Eggleton, and

H. Giessen, "Ultrafast nonlinear optofluidics in selectively liquid-filled photonic crystal fibers," Optics Express **18**, 25232-25240 (2010).

[7]. J. Ju, H. F. Xuan, W. Jin, S. Liu, and H. L. Ho, "Selective opening of airholes in photonic crystal fiber," Optics Letters **35**, 3886-3888 (2010).

[8]. Y. Wang, C. Liao, and D. Wang, "Femtosecond laser-assisted selective infiltration of microstructured optical fibers," Optics Express **18**, 18056-18060 (2010).

[9]. Y. Hoo, W. Jin, H. Ho, and D. Wang, "Measurement of gas diffusion coefficient using photonic crystal fiber," Photonics Technology Letters, IEEE **15**, 1434-1436 (2003).

[10]. Y. Hoo, W. Jin, H. Ho, J. Ju, and D. Wang, "Gas diffusion measurement using hollow-core photonic bandgap fiber," Sensors and Actuators B: Chemical **105**, 183-186 (2005).

[11]. J. Henningsen, and J. Hald, "Dynamics of gas flow in hollow core photonic bandgap fibers," Applied Optics **47**, 2790-2797 (2008).

[12]. J. H. Jeans, *An introduction to the kinetic theory of gases* (Cambridge University Press, 1967).

[13]. G. G. Raju, *Gaseous electronics: theory and practice* (CRC Press, 2005).

[14]. T. I. Gombosi, *Gaskinetic theory* (Cambridge University Press, 1994).

[15]. D. R. Lide, and T. J. Bruno, *Handbook of Chemistry and Physics* (CRC PressI Llc, 2010).

[16]. K. Boyd, H. Ebendorff-Heidepriem, T. M. Monro, and J. Munch, "Surface tension and viscosity measurement of optical glasses using a scanning CO2 laser," Optical Materials Express **2**, 1101-1110 (2012).

[17]. H. C. Nguyen, B. T. Kuhlmey, E. C. Mägi, M. J. Steel, P. Domachuk, C. Smith, and B. Eggleton, "Tapered photonic crystal fibres: properties, characterisation and applications," Applied Physics B **81**, 377-387 (2005).

[18]. M. Tachikura, "Fusion mass-splicing for optical fibers using electric discharges between two pairs of electrodes," Applied Optics **23**, 492-498 (1984).

[19]. A. D. Yablon, *Optical fiber fusion splicing* (Springer, 2005).

[20]. F. M. Cox, R. Lwin, M. C. Large, and C. Cordeiro, "Opening up optical fibres," Optics Express **15**, 11843-11848 (2007).

[21]. S. C. Warren-Smith, H. Ebendorff-Heidepriem, T. C. Foo, R. Moore, C. Davis, and T. M. Monro, "Exposed-core microstructured optical fibers for real-time fluorescence sensing," Optics Express **17**, 18533-18542 (2009).

[22]. C. M. Cordeiro, E. M. Dos Santos, C. B. Cruz, C. J. de Matos, and D. S. Ferreira, "Lateral access to the holes of photonic crystal fibers-selective filling and sensing applications," Opt. Express **14**, 8403-8412 (2006).

[23]. L. Xiao, M. Demokan, W. Jin, Y. Wang, and C.-L. Zhao, "Fusion splicing photonic crystal fibers and conventional single-mode fibers: microhole collapse effect," Journal of Lightwave Technology **25**, 3563-3574 (2007).

[24]. M. Steel, T. White, C. Martijn de Sterke, R. McPhedran, and L. Botten, "Symmetry and degeneracy in microstructured optical fibers," Optics Letters **26**, 488-490 (2001).

[25]. J. B. Aniano, "System for determining birefringent axes in polarization-maintaining optical fiber," (Google Patents, 1994).

[26]. L. Zang, T. Euser, M. Kang, M. Scharrer, and P. S. J. Russell, "Structural analysis of photonic crystal fibers by side scattering of laser light," Optics Letters **36**, 1668-1670 (2011).

[27]. L. Watkins, "Scattering from side-illuminated clad glass fibers for determination of fiber parameters," JOSA **64**, 767-772 (1974).

[28]. E. Mägi, H. Nguyen, and B. Eggleton, "Air-hole collapse and mode transitions in microstructured fiber photonic wires," Optics Express **13**, 453 (2005).

[29]. O. Frazao, J. Baptista, J. Santos, J. Kobelke, and K. Schuster, "Strain and

temperature characterisation of sensing head based on suspended-core fibre in Sagnac interferometer," Electronics Letters **44**, 1455-1456 (2008).

[30]. Y. Zhu, H. Du, and R. Bise, "Design of solid-core microstructured optical fiber with steering-wheel air cladding for optimal evanescent-field sensing," Optics Express **14**, 3541-3546 (2006).

[31]. R. Silva, M. Ferreira, J. Kobelke, K. Schuster, and O. Frazão, "Simultaneous measurement of curvature and strain using a suspended multicore fiber," Optics Letters **36**, 3939-3941 (2011).

[32]. M. Liao, C. Chaudhari, X. Yan, G. Qin, C. Kito, T. Suzuki, and Y. Ohishi, "A suspended core nanofiber with unprecedented large diameter ratio of holey region to core," Optics Express **18**, 9088-9097 (2010).

[33]. K. Okamoto, *Fundamentals of Optical Waveguides* (Academic Press, 2006).

[34]. A. W. Snyder, and J. Love, *Optical waveguide theory* (Springer, 1983).

[35]. K. Saitoh, and M. Koshiba, "Full-vectorial imaginary-distance beam propagation method based on a finite element scheme: Application to photonic crystal fibers," Quantum Electronics, IEEE Journal of **38**, 927-933 (2002).

[36]. F. Fogli, L. Saccomandi, P. Bassi, G. Bellanca, and S. Trillo, "Full vectorial BPM modeling of index-guiding photonic crystal fibers and couplers," Optics Express **10**, 54-59 (2002).

[37]. H. Ebendorff-Heidepriem, P. Petropoulos, S. Asimakis, V. Finazzi, R. Moore, K. Frampton, F. Koizumi, D. Richardson, and T. Monro, "Bismuth glass holey fibers with high nonlinearity," Optics Express **12**, 5082-5087 (2004).

[38]. T. Pustelny, and M. Grabka, "Numerical investigation of the photonic-crystal fibres with suspended core," Acta Physica Polonica-Series A General Physics **116**, 385 (2009).

Chapter 4 : The 6-hole Microcell - Properties and Application

In this chapter, the advantages of the 6-hole suspended core (SC) microcell are discussed. Based on this type of microcell, a novel robust micro-cantilever structure fabricated inside the cell is presented. The structure is realized experimentally with the aid of a femtosecond (fs) laser micromachining system. The micro-cantilever demonstrates a linear response to the acceleration imposed on the microcell.

4.1 Characterization

Research on the suspended core fibers (SCFs) with the core surrounded by six air-columns have been conducted for many years. Figure 4.1 illustrates cross-sectional micrographs of some typical six holes SCFs, where (a) is the grapefruit fiber which possesses relatively larger holes in the fiber holey region. The fiber core is about 8μm germanium-doped region in the central area, which guarantees single mode operation and low loss connection to SMFs. However, most power of light propagated in fiber is confined in the solid central area, that is, the evanescent field in the holey region is little. Figure (b) is a single material MOFs with solid core and large relative hole-size d/Λ. Since field distribution of the light propagating in fiber decays dramatically when it encounters the air holes, so the mode is actually confined within the innermost ring of holes. [1] The MOF in (b) can be simplified to a structure containing only the innermost ring of holes, such as Figure 4.1 (c) and (d). To enlarge the light-matter interaction in holey region, submicron sized core SCFs are always used in applications of evanescent field sensing. However, constrained by the fabrication technique, the holey region of current SCFs are typically small. By applying the modified fiber-drawing technique, SCF with diameter ratio of holey region to core (DRHC) up to ~20 can be produced (Figure 4.1 (d)). This might be the largest DRHC value in reported six holes SCFs. [2]

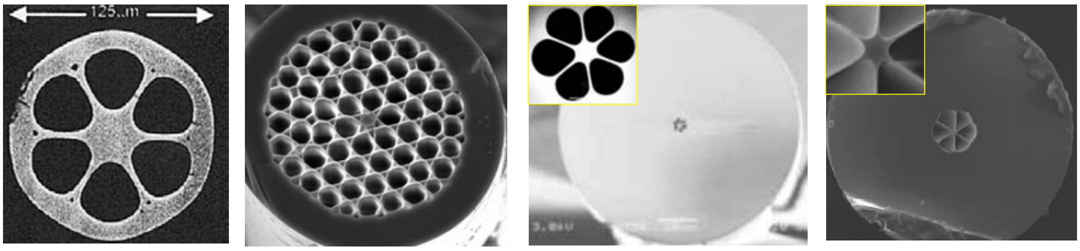

(a) (b) (c) (d)

Figure 4.1 The cross-section micrographs of typical six holes MOFs with six holes or six holes within the innermost ring. (a) Grapefruit fiber [3], (b) Holey fiber [1], (c) Six holes SCF [4], and (d) Six holes SCF with large DRHC[2]

Compared with the SCFs in Figure 4.1, the unique advantages of the 6-hole SC microcell include (a) a large DRHC (up to 40) which means lower confinement loss to the light with longer wavelength [5], (b) low loss connection to the SMF, (c) fundamental mode only because of the adiabatic transition to ESM PCF, and (d) a thin jacket tube. These distinguishing features enable the 6-hole microcell to be applied in many novel applications

Most research activities on the 6-hole SCFs are concerned with guidance properties, such as abnormal dispersion, supercontinuum generations, bending loss, and mode coupling [2, 6, 7]. However, we noticed the special interior structure would be suitable for building some micro-structures. The fs laser micromachining is a good choice for this task. As introduced in section 2.3, the interaction between fs laser and transparent material would take place only in the region around the focus while leaving the other place intact. Benefiting from the thin jacket region, the fiber core and struts in the microcell can be clearly observed from the fiber side with microscope. Meanwhile fs laser pulses can penetrate the jacket layer with little loss. The micrograph in Figure 4.2 shows the core and struts of a 6-hole microcell with 20x objective lens focused on the core region. Starting from these basic intuitions, a novel micro-cantilever in the microcell is proposed. Although the core of cell is tightly fixed in the cell initially, it could be set free by locally micro-machining. Then the freed fiber core would serve as the beam of a cantilever.

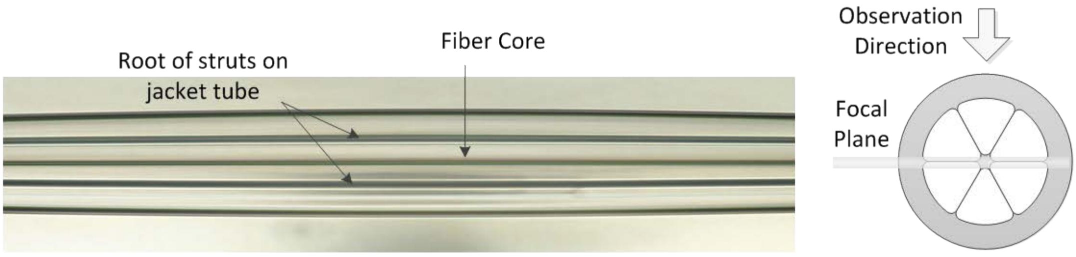

Figure 4.2 (Left) Side-view micrograph of a 6-hole microcell; (Right) Schematic of the observation condition

The mode field distribution of SC microcell is typically non-circular symmetrical and strongly modified by the shape of core. In the direction from center towards a hole, the field decays dramatically after the silica-air interface. And in the direction towards a strut, the field extends slightly longer into the silica struts [8]. Curves in Figure 4.3(b) are the calculated 1D power distribution of the fundamental mode at 1550 nm along directions ‘a’, ‘a’’, and ‘b’ which are defined in (a). The three microcells have the same effective radius r_{eff} = 3μm. ‘a’ is the direction towards the strut, and ‘b’ is the direction towards the center of air hole. For the 4-hole microcell, ‘a’’ is the direction towards the strut along short axis. The deviation between the curves along ‘a’ and ‘b’ could represents the maximum deviation of the mode in all radius direction.

The dot lines in figure (b) indicate the position where the intensity drops to the $1/e^2$ of the maximum value. The position is commonly used to define the radius of a Gaussian beam. For the Gaussian-like intensity profiles, boundaries of the fundamental mode along particular directions are indicated by the dot lines. The fundamental mode of each microcell is anisotropy in distribution. However, the boundary variance of the 6-hole microcell is just ~24.8% and ~30% of the value in the 4-hole and 3-hole microcell, respectively. So the variance of the mode of the 6-hole microcell in a radius direction is much lower than the other two types. Furthermore, the calculation results in Figure 4.3 (b) also predict that the struts can be removed with little influence on the fundamental mode because most of the power is deeply confined in the core region.

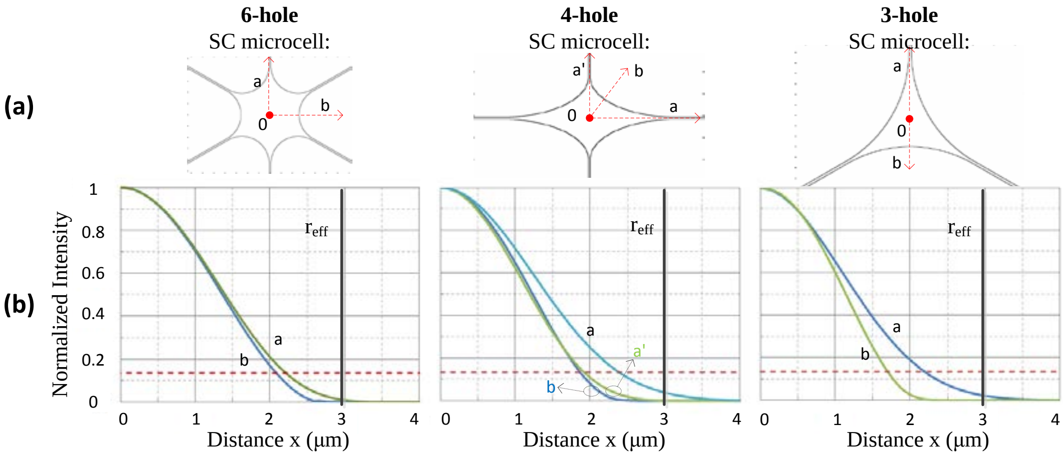

Figure 4.3 (a) Schematic of the microcell core regions; (b) The power distributions of the fundamental mode along the directions defined in (a)

4.2 Fabrication of Micro-cantilever in Microcell

In this section, the fabrication process of micro-cantilever inside a 6-hole SC microcell is introduced. The cantilever is produced by local micromachining the internal structure of a 6-hole microcell. The setup for the fabrication is shown in Figure 4.4. The sample containing a piece of 6-hole SC microcell is fixed on a motion stage by two rotation fixtures. By rotating the fixtures and moving the translation stage, the laser beam can be focused on any position in the microcell. One end of the sample is connected to a broadband source covering a wavelength from 1450 nm to 1650 nm, while the other end is connected to an optical spectrum analyzer to monitor the changing of transmission spectrum during the process.

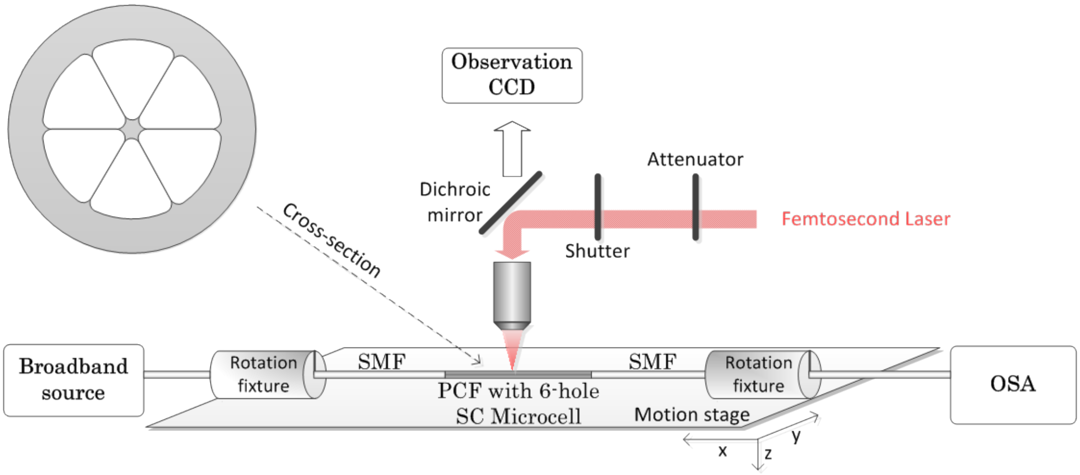

Figure 4.4 Equipment setup for building a micro-cantilever

The detailed procedure of building a micro-cantilever in a microcell can be explained with the aid of Figure 4.5. The initial status of a section of the 6-hole microcell is provided in (a). In order to highlight the interior structure, the jacket tube of the microcell is omitted in (b) and (c). The dash arrow lines represent the traces of an fs laser beam on the machining surface, and the numbers represent the operation sequence.

The first step is to designate the beginning and end positions of the cantilever beam on each strut by fs laser scanning in a direction vertical to the fiber axis. Then the struts, which connect the jacket tube and the fiber core (cantilever beam) is removed by scanning the focused fs laser one by one. The scanning path “2” should not be too close to the fiber core in case any damage on the core is caused with scattered fs laser beam. After this step, a short section of fiber core is suspended in the air inside microcell. Finally, in step “3”, the fiber core is cut off by fs laser at one end of the machining region. The fiber core at the cut end serves as the free end of the cantilever, and the other end as a fixed end.

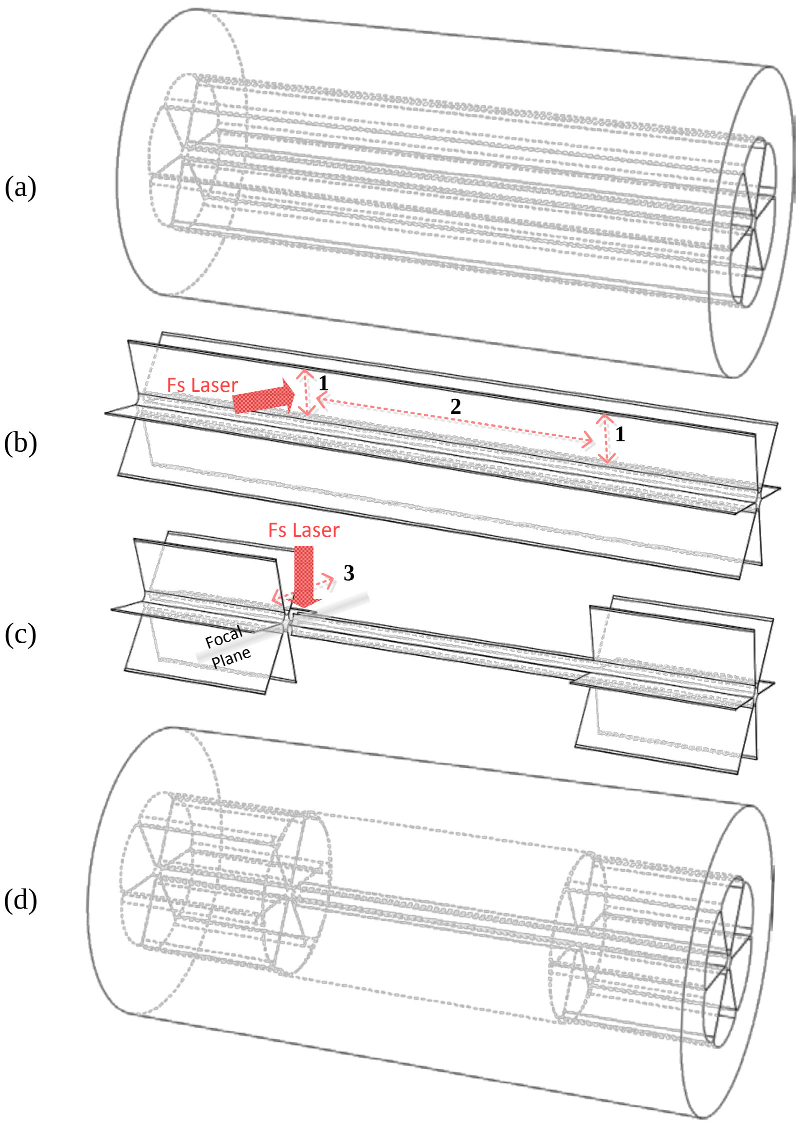

Figure 4.5 Schematic diagram of the fabrication process (a) initial status of a 6-hole microcell; (b) and (c) procedures of fabricating a micro-cantilever; (d) the final status of the cantilever based on a 6-hole microcell

Overall picture of a micro-cantilever is given in Figure 4.6 (a). The free end and fixed end regions of the cantilever are enlarged and shown in (b) and (c) respectively. As illustrated in (b), a small offset is purposely produced to make the optical intensity of transmitted light responding linearly to the deflection of cantilever. The offset is introduced by using the fs laser to pare one side of the beam.

Discussion about function of the offset is given in the next section.

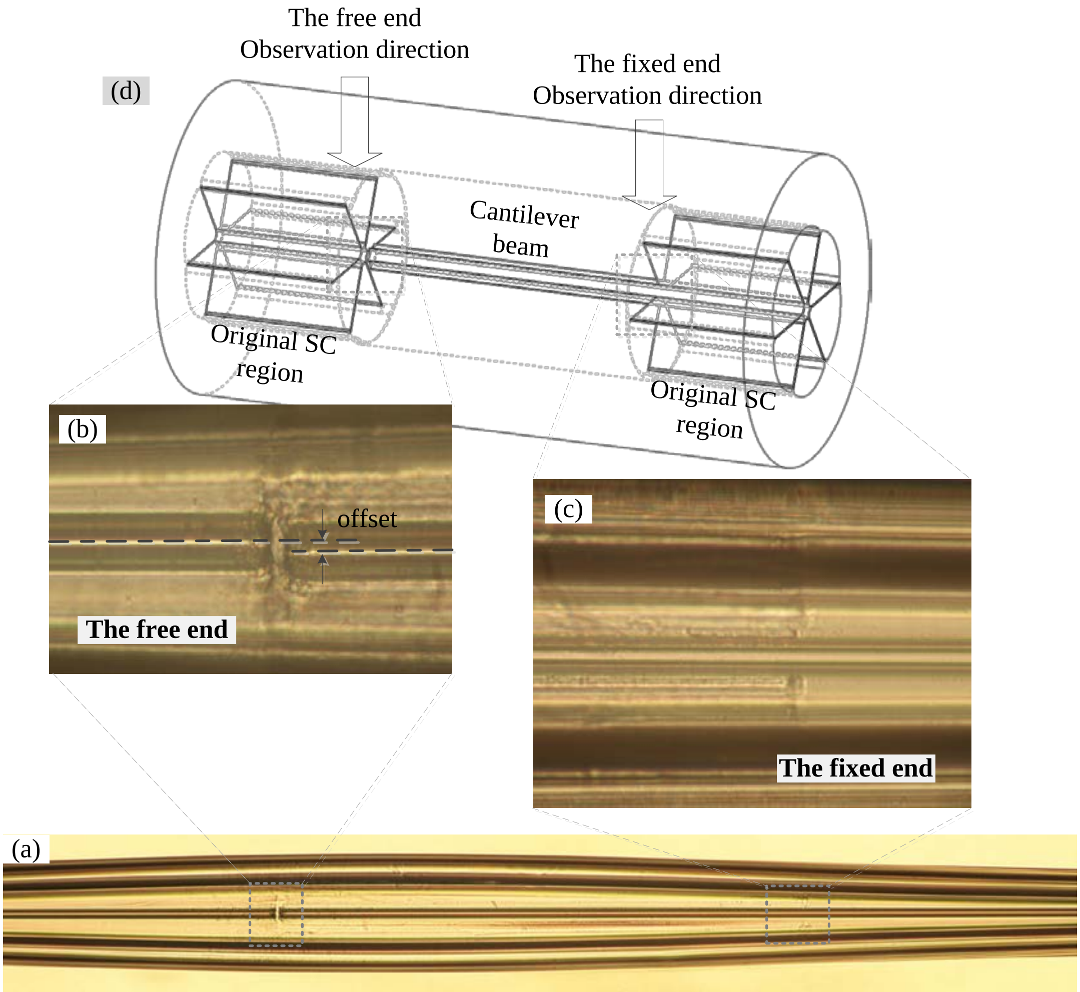

Figure 4.6 Photos and schematic of a micro-cantilever fabricated in a microcell

Compared with other types of cantilever design on fiber, such as fiber top cantilevers [9, 10], the advantages of this microcell-based cantilever are distinct. In our design, the cantilever is fabricated inside a microcell with intact surface. So the device is robust and unaffected by external contamination. Moreover, the beam can be fabricated with wide range in its length and thickness.

4.3 Acceleration Sensing with the Micro-cantilever

4.3.1 Principles

The micro-cantilever introduced in the last section can be used to sense acceleration imposed on the microcell. When a cell is accelerated, the small deflection of cantilever free end causes a misalignment between the beam and the fixed fiber core at the cut position, and results in a modulation on the transmitted light intensity.

To guarantee the transmission of light, the degree of misalignment would be a small value corresponding to a vertical offset not larger than the core size. Compared with the length of the beam (few millimeters), the offset of free-end is small. Under the small deflection assumption, the deflection at the free end δ of the beam is linearly related to the acceleration **a** according to formula (4.1). [11]

$$\delta = \frac{A\rho l^4}{8EI} a \tag{4.1}$$

where A is the cross-sectional area of the beam, l is the beam length, a is the acceleration, ρ is the mass density, E is the Young's modulus, and I is second moment of area. Under the assumption that the microcell cantilever is cylindrical, I of the cantilever can be expressed by the radius of the fiber core **r** as (4.2).

$$I = \frac{\pi r^4}{4} \tag{4.2}$$

From formula (4.1) and (4.2), the deflection of the cantilever under acceleration is proportional to the forth power of length (l^4**)** and the reciprocal of the radius' square ($1/r^2$). So increasing the cantilever beam length and decreasing the beam radius causes the sensitivity growth.

The resonant frequency of cantilever is also related to its length and cross-sectional dimension. The lowest resonance frequency of a cylindrical cantilever beam is given by the formula (4.3). [12]

$$f = \frac{1}{\pi l^2}\sqrt{\frac{2EI}{\rho A}} \tag{4.3}$$

Increasing the cantilever beam length and decreasing the beam radius causes the resonance frequency to decrease, and limits the range of flat frequency response.

The deflection of the micro-cantilever causes the mismatch loss of the light power propagating in the core. It can be estimated by the multiplication of the transmission coefficients corresponding to three different misalignment statuses, as illustrated in Figure 4.7 , i.e. separation, offset and tilt.

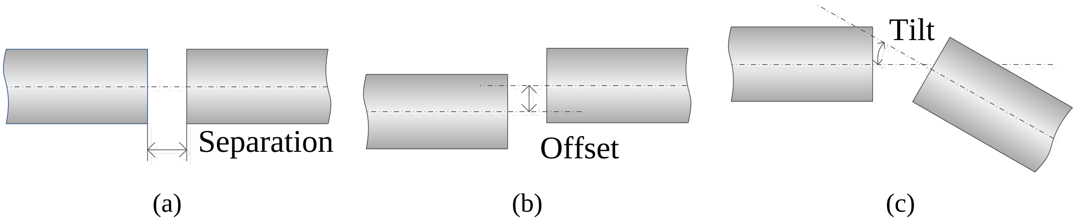

Figure 4.7 The misalignment status between two fiber ends. (a) Separation, (b) offset, and (c) tilt

The power transmission coefficients of each status in formula (4.4), (4.5), and (4.6) are derived by Marcuse for the computation of transmission losses between misaligned Gaussian beams.[13]

$$T_{seperation} = \frac{4\left[4z^2 + \frac{w_1^2}{w_2^2}\right]}{\left[4z^2 + \frac{w_1^2 + w_2^2}{w_2^2}\right] + 4z^2\frac{w_2^2}{w_1^2}}, \quad z = \frac{D}{nkw_1w_2} \tag{4.4}$$

$$T_{tilt} = \left(\frac{2w_1w_2}{w_1^2 + w_2^2}\right)^2 \exp\left[-\frac{2\left(\pi n w_1 w_2 \theta\right)^2}{\left(w_1^2 + w_2^2\right)\lambda^2}\right] \tag{4.5}$$

$$T_{offset} = \left(\frac{2w_1w_2}{w_1^2 + w_2^2}\right)^2 \exp\left[-\frac{2d^2}{w_1^2 + w_2^2}\right] \tag{4.6}$$

where w_1 and w_2 are the Gaussian radius of spliced fibers. D, θ, and d are, respectively, the separation, tilt and offset. n is the RI of the material between two fiber ends and λ is the operating wavelength.

The contour of the fundamental mode of the 6-hole SC microcell along the cut line **a** and **b** can be fit with Gaussian function with R^2 equal to 99.85% and 99.56%, respectively. So it is reasonable to apply Marcuse's theory in the application.

For the structure shown in Figure 4.6 (a), the cantilever beam is ~1.35mm long and the gap between the two sections of the core is ~5μm. The transmission coefficient is calculated and shown in Figure 4.8 (b). In the region marked by the bold line, the optical transmission exhibits a quasi-linear response to the free end offset. To make the device work in this region, a fourth step after the three steps in Figure 4.5 is required to introduce the initial offset to the cantilever beam. The fourth step is illustrated in Figure 4.8 (a). The initial offset is realized by paring one side of the beam with a focused fs laser. The offset can be accurately controlled by in situ monitoring the variation of transmission power of the sample. To achieve the optimized position, which is the center of the bold-line region in Figure 4.8 (b), a requirement to the decrease of transmission power is about 3 dB. The micrograph of a beam offset is provided in Figure 4.6(b).

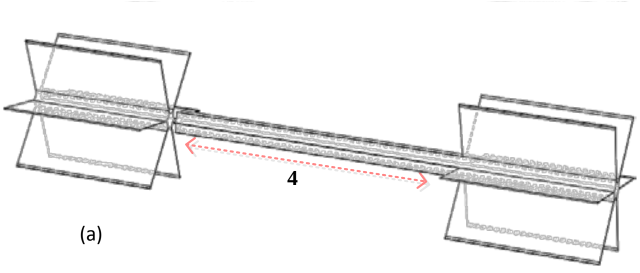

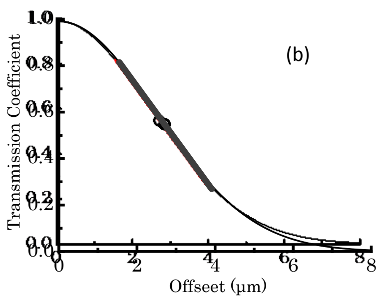

Figure 4.8(a) A fourth micromachining step to introduce offset at the free end; (b) Optical power transmission coefficient versus offset at the cantilever beam free end (the effect of tilt and separation are all included)

4.3.2 Experimental setups and the results

Preliminary tests of the in-line accelerometer were conducted with the setup shown in Figure 4.9. Light from a 1530 nm DFB laser was delivered to the microcell (device under test or DUT) and the output was collected by a photo receiver. The DUT was fixed to a vibration exciter by using a steel fixture, and a commercial piezoelectric accelerometer was attached to the same fixture to provide accurate real-time calibration of the applied acceleration.

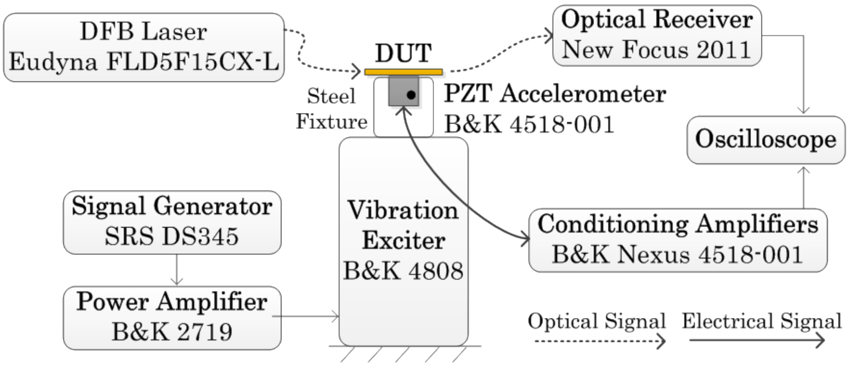

Figure 4.9 Setup for testing the in-line accelerometer. DUT is the cantilever beam accelerometer [14]

Figure 4.10 (a) shows the oscilloscope traces measured with the reference and the cantilever beam accelerometers when a 100 Hz excitation signal is applied. The sensitivity of the reference accelerometer is 31.6 mV/g. The conversion coefficient and gain factor of the optical receiver are 0.56 V/mW and 30x, respectively. Figure 4.10 (b) shows the output amplitudes of the fiber-optic accelerometer as functions of acceleration for an applied frequency of 100 Hz and 1 kHz. Good linear relationships were obtained within the test range from 0.01 to 5 g. This is about one third of the range reported in [15]. The test range of acceleration is limited by the experimental setup. A theoretical calculation based on the linear region of Figure 4.8 (b) indicates that the linear response range could reach 60 and 58.4 g for 100 Hz and 1 kHz, respectively. Figure 6 (c) shows the frequency response of the fiber-optic accelerometer. A resonant peak appears at ~6.6 kHz, and the response is flat until ~2.5 kHz with a sensitivity of ~2.6 mV/g. For frequencies closer to the resonant peak, the sensitivity would increase significantly, but the linear response range would decrease. Figure 4.10 (d) shows the spectrum of the fiber-optic accelerometer output when an acceleration of 10 mg in amplitude and 100 Hz in frequency is applied. The resolution bandwidth is set to 2 Hz. The signal to noise ratio at 100 Hz is ~35.5 dB, from which the minimum detectable acceleration corresponding to SNR=1 is calculated to be 119 μg/(Hz)$^{1/2}$. [14]

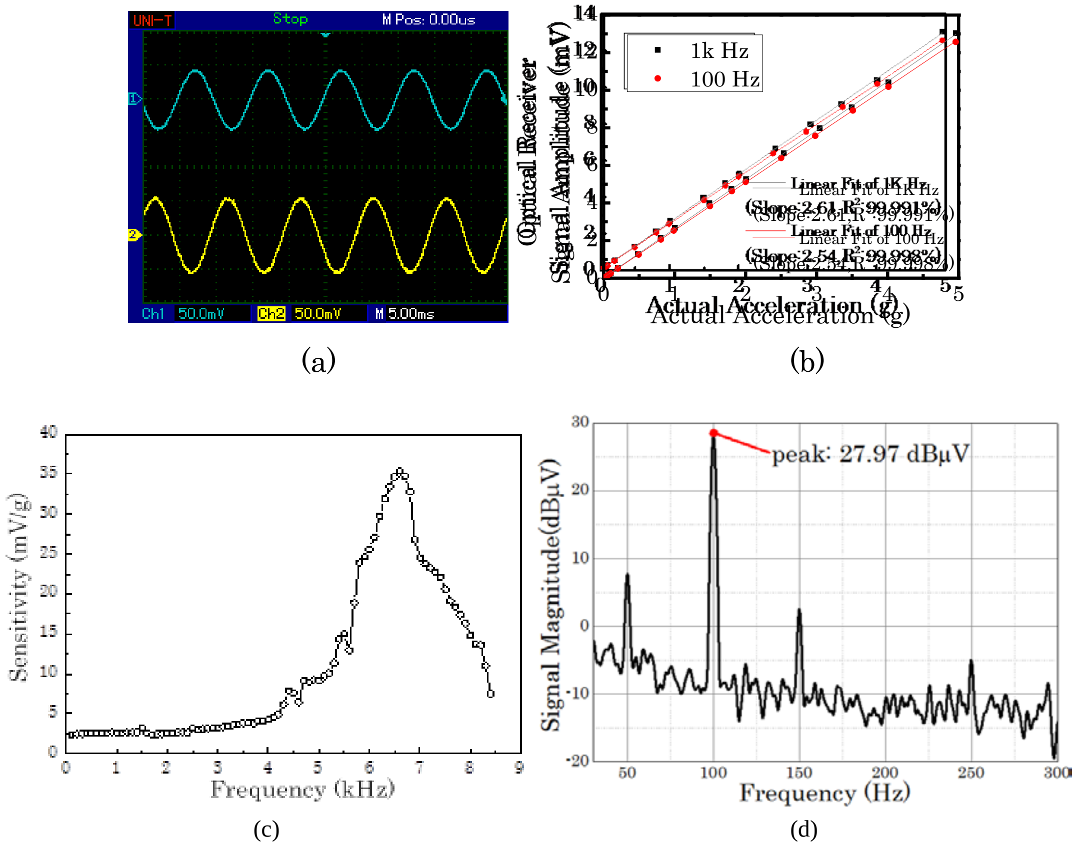

Figure 4.10 (a) Traces of the outputs from the reference piezoelectric accelerometer (upper) and our sample (lower); (b) Magnitude of the fiber-optic accelerometer output versus acceleration (obtained from the piezoelectric accelerometer); (c) Frequency response of the fiber-optic accelerometer; (d) Output spectrum when an acceleration of 10 mg (amplitude) at 100Hz is applied [14]

4.4 Summary

In this Chapter, the characteristics of the 6-hole SC microcell have been discussed. Based on such a microcell, an in-line micro-cantilever is demonstrated. The cantilever exhibited a linear response to the acceleration imposed on it. A sample with a sensitivity of ~2.6 mV/g and a minimum detectable acceleration of ~119 $\mu g/(Hz)^{1/2}$ was demonstrated. The response of sample was flat until ~2.5 kHz

4.5 Reference

[1]. T. M. Monro, W. Belardi, K. Furusawa, J. C. Baggett, N. G. Broderick, and D. J. Richardson, "Sensing with microstructured optical fibres," Measurement Science and Technology **12**, 854 (2001).

[2]. M. Liao, C. Chaudhari, G. Qin, X. Yan, T. Suzuki, and Y. Ohishi, "Tellurite microstructure fibers with small hexagonal core for supercontinuum generation," Optics Express **17**, 12174-12182 (2009).

[3]. B. Eggleton, P. Westbrook, C. White, C. Kerbage, R. Windeler, and G. Burdge, "Cladding-mode-resonances in air-silica microstructure optical fibers," Journal of Lightwave Technology **18**, 1084 (2000).

[4]. L. Dong, B. K. Thomas, and L. Fu, "Highly nonlinear silica suspended core fibers," Optics Express **16**, 16423-16430 (2008).

[5]. M. Liao, C. Chaudhari, X. Yan, G. Qin, C. Kito, T. Suzuki, and Y. Ohishi, "A suspended core nanofiber with unprecedented large diameter ratio of holey region to core," Optics Express **18**, 9088-9097 (2010).

[6]. E. Mägi, H. Nguyen, and B. Eggleton, "Air-hole collapse and mode transitions in microstructured fiber photonic wires," Optics Express **13**, 453 (2005).

[7]. T. M. Monro, and H. Ebendorff-Heidepriem, "Progress in microstructured optical fibers," Annu. Rev. Mater. Res. **36**, 467-495 (2006).

[8]. N. Asger Mortensen, "Effective area of photonic crystal fibers," Optics Express **10**, 341 (2002).

[9]. K. B. Gavan, J. H. Rector, K. Heeck, D. Chavan, G. Gruca, T. H. Oosterkamp, and D. Iannuzzi, "Top-down approach to fiber-top cantilevers," Optics Letters **36**, 2898-2900 (2011).

[10]. A. Said, M. Dugan, S. de Man, and D. Iannuzzi, "Carving fiber-top cantilevers with femtosecond laser micromachining," Journal of Micromechanics and Microengineering **18**, 035005 (2008).

[11]. J. M. Gere, and B. J. Goodno, *Mechanics of Materials* (Cengage Learning, 2009).

[12]. T. Guo, L. Shao, H.-Y. Tam, P. A. Krug, and J. Albert, "Tilted fiber grating accelerometer incorporating an abrupt biconical taper for cladding to core recoupling," Optics Express **17**, 20651-20660 (2009).

[13]. D. Marcuse, "Loss analysis of single-mode fiber splices," Bell Syst. Tech. J **56**, 703-718 (1977).

[14]. C. Wang, W. Jin, J. Ma, Y. Wang, H. L. Ho, and X. Shi, "Suspended core photonic microcells for sensing and device applications," Optics Letters **38**, 1881-1883 (2013).

[15]. A. Stefani, S. Andresen, W. Yuan, N. Herholdt-Rasmussen, and O. Bang, "High sensitivity polymer optical fiber-Bragg-grating-based accelerometer," Photonics Technology Letters, IEEE **24**, 763-765 (2012).

Chapter 5 : The 4-hole Microcell - Properties and Applications

In this chapter, the advantages of the 4-hole suspended core (SC) microcell are discussed. The intrinsic birefringence of the SC microcell is highly sensitive to the RI around the core. Based on this kind of microcell, sensors for temperature and pressure are demonstrated.

5.1 Characterization

High-birefringent (Hi-Bi) MOFs in which the linear polarization state of propagating light is tightly maintained have long been applied for various building fiber optical sensors [1], and optical fiber communication applications [2]. High birefringence can be produced in MOFs by the stress applied to parts around the fiber core and the geometrical effect of the core. Examples of these types of Hi-Bi fibers are the hybrid PCF [3], the bow-tie-like Hi-Bi MOF [4] and the panda-like Hi-Bi PCF [5].

For the SCF, the Hi-Bi structure by stress effect around the core might not be feasible because of the isolation of the fiber core by large air-fraction cladding. Nevertheless, Hi-Bi SCF could be realized by introducing a two-fold symmetrical structure to the fiber core. In Figure 5.1 (a) might be the first published two-fold symmetrical SCF [6]. The SCF could be used for a temperature-independent (~0.29 pm/°C) strain sensor (~1.94 pm/mε) when it was tested in a Sagnac loop interferometer configuration. However, this SCF exhibits a typical group birefringence ~ 4.8 x10^{-5} which is lower than the value of most Hi-Bi MOFs.

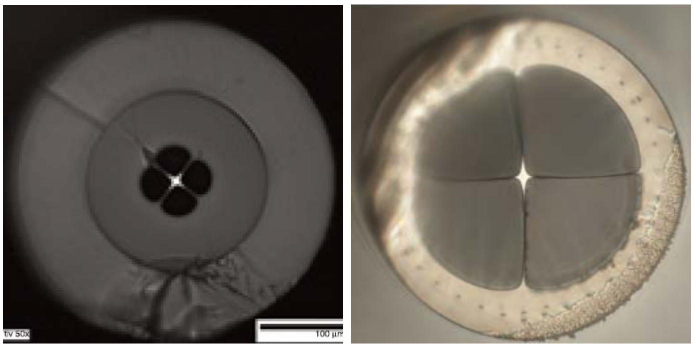

(a) **(b)**

Figure 5.1 (a) Micrograph of a SCF with four holes[6]; (b) Micrograph of a 4-hole SC microcell

The 4-hole microcell in Figure 5.1 (b) typically has a high aspect ratio core which enables the microcell to feature a very high birefringence (up to 10^{-2} in simulation). Although the aspect ratio 'a/b' of the 4-hole microcell core is ~2.1 and changes little with the core dimension, the (phase) birefringence defined by equation (5.1) changes with the core size and operation wavelength. $n_{x,eff}$ and $n_{y,eff}$ in (5.1) represent the effective refractive indexes (RI) of the fundamental mode in the x and y polarization states. They can be calculated numerically by the FEM software. The model of the 4-hole microcell for calculation was provided in section 3.3.2.

$$B = \Delta n = n_{x,eff} - n_{y,eff} \tag{5.1}$$

The birefringence B varies with the operation wavelength and waveguide dimension because the effective RIs are wavelength and dimension relevant. Figure 5.2 (a) shows the fundamental mode birefringence of the 4-hole microcell as a function of normalized frequency $\sqrt{a_{eff} \times b_{eff}} / \lambda$, where a_{eff} and b_{eff} are, respectively, the effective major semi-axis and minor semi-axis as defined in Figure 3.21. The birefringence of the cell has a theoretical maximum of ~3.6 x10^{-2} with the normalized frequency ≈0.31. This property provides an optimum normalized frequency window for the design of microcells with a large birefringence.

The birefringent curves of the microcell with various core sizes are given in

Figure 5.2 (b) for comparison. In the wavelength window 1450-1650nm, the optimized effective minor semi-axis of the core is ~0.35μm. When b_{eff} beyond a ~1μm, the birefringence in the window decreases dramatically. This may be explained by the shift of birefringence peak to longer wavelength region.

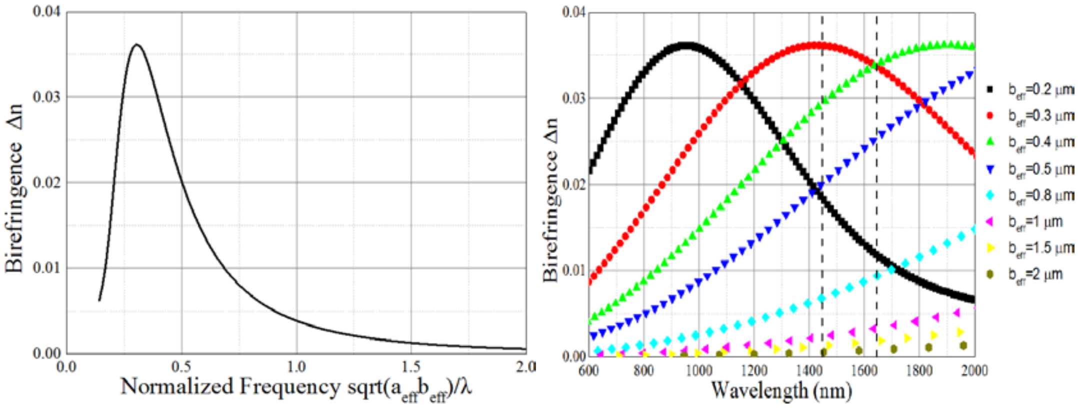

(a) **(b)**

Figure 5.2 Birefringence of the 4-hole microcell as a function of (a) normalized frequency, and (b) wavelength

The importance of the previous analysis is that it can be used in the practical design of the 4-hole SC microcell with desired properties. To achieve the maximum birefringence at a particular operating wavelength, the fiber parameters and modal property may be estimated.

The properties of the microcell would also be influenced by the RI of the holey region (n_{hole}) which can be changed by, for example, infiltrating RI oil into, or pressurizing the air in the holes of the microcell. For the microcell illustrated in Figure 5.3, the fraction of light power in the holes with n_{hole}=1.43 would theoretically be ~10 and ~37 times larger than in holes with an RI = 1.3 and an RI = 1, respectively (normalized frequency ~0.8).

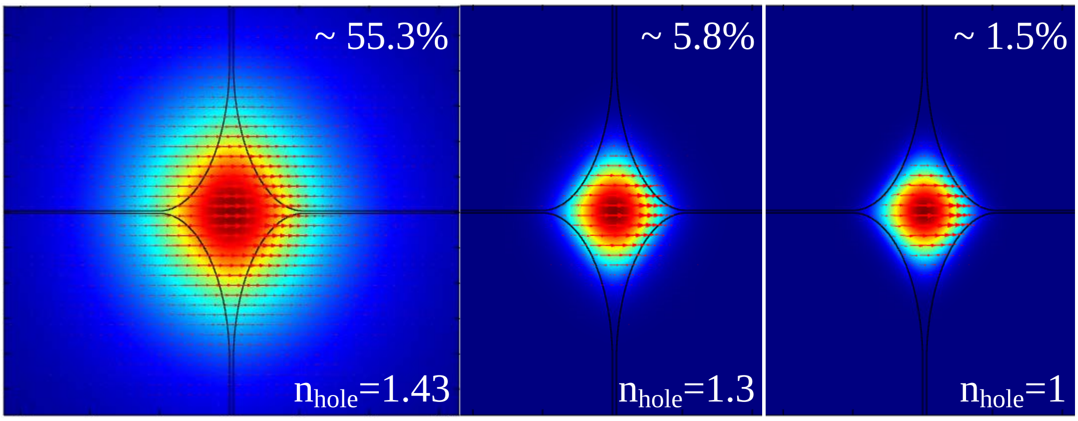

Figure 5.3 The intensity distribution of the 4-hole SC microcell with different holey region RIs

So when the RI increases in the holes, the lower RI difference between the core and holey region leads to more light power propagating in the holey region. And the increase of the power ratio in the holes becomes faster when the n_{hole} is close to the RI of the fiber core.

The birefringence of the 4-hole SC microcell will also be influenced by the n_{hole} because the confinement of light in the core region becomes weak when the n_{hole} increases. As a result, the birefringence introduced by the core geometry of the 4-hole SC microcell will decrease with increasing n_{hole}. Figure 5.4 (a) and (b), respectively, demonstrate the dispersion curves and birefringence of the microcell with a different n_{hole}. The non-degeneracy of the two polarization-states of the fundamental mode represents the birefringence of fiber. Corresponding to the n_{hole} equal to 1 and 1.3, the peak birefringence decreases from 3.6 $\times 10^{-2}$ to 3.3 $\times 10^{-3}$ and moves towards the high frequency region. The birefringence almost vanishes when the n_{hole} increases to 1.41. The decreasing of birefringence is significant with a higher n_{hole}.

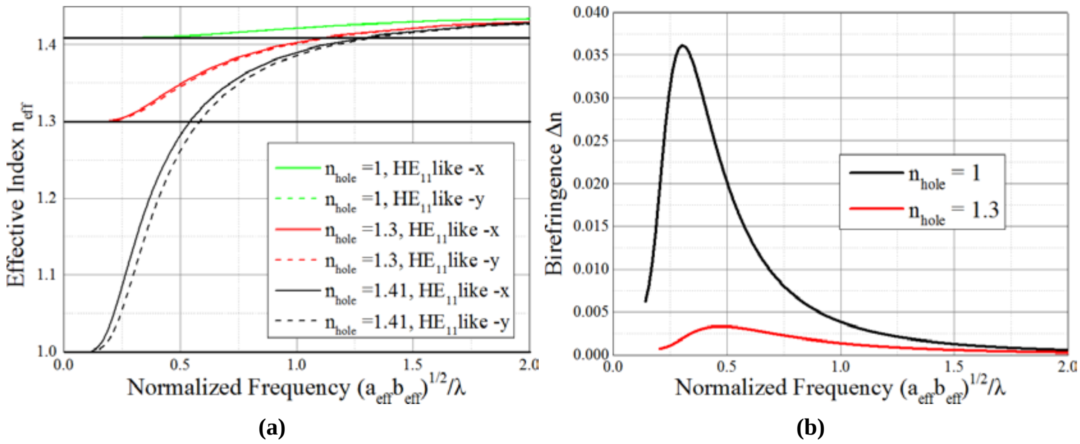

Figure 5.4 (a) The dispersion curves and (b) birefringence of the fundamental mode in the 4-hole SC microcell with a different holey region RI

The high sensitivity of the birefringence to environmental RI of core makes it possible to apply the SC microcell in sensing physical parameters according to the variance of RI.

5.2 Sensing with the 4-hole Microcells

The Sagnac loop interferometer is widely used in Hi-Bi fiber based sensing. Compared with the interferometer configuration, which consist of a Hi-Bi fiber sandwiched between two polarizers, the Sagnac loop scheme typically has a lower insertion loss. [7]

5.2.1 Principles

A common Sagnac loop interferometer contains of a fiber coupler, one or several polarization controller(s) (PC) and section(s) of Hi-Bi Fiber. As illustrated in Figure 5.5, the light wave from the input port 1 will be split into the two parts propagating along ports 3 and 4, respectively. The waves in ports 3 and 4 propagate oppositely in the loop and subsequently recombine at the coupler. The phase difference of the counter-propagating waves depends on the birefringence of the cavity. At the output port 2, the constructive or destructive interference can be observed. The polarization of light propagating along both directions in the loop can be adjusted by the PC to maximize the amplitude of the interference pattern.

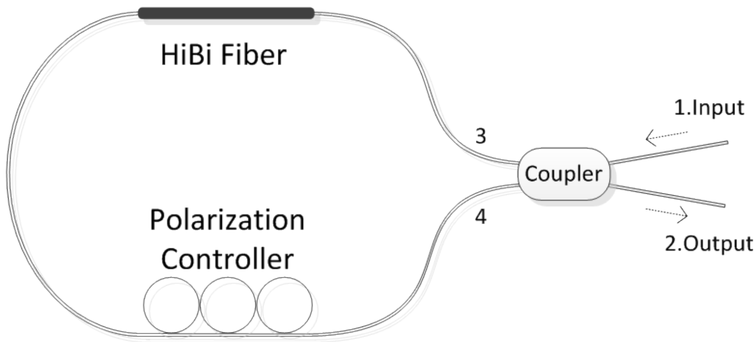

Figure 5.5 Schematic of Sagnac loop interferometer

The transmission can be calculated by combining the matrices of each sequential element in the optical path according to the rules of the Jones calculus. [8] Considering the condition with just one Hi-Bi fiber and one PC in the loop, the transmission function of the interferometer could be expressed by equation (5.2).

$$\begin{bmatrix} [E_{1,out}] \\ [E_{2,out}] \end{bmatrix} = [C] \begin{bmatrix} P(-\theta_1)F_1P(-\theta_2) & 0 \\ 0 & P(\theta_2)F_1P(\theta_1) \end{bmatrix} [C] \begin{bmatrix} [E_{1,in}] \\ [E_{2,in}] \end{bmatrix} \tag{5.2}$$

where $[E_{1,in}],[E_{1,out}],[E_{2,in}],[E_{2,out}]$ are column jones vectors which describe the input and output fields of port 1 and port 2, respectively. $P(\theta_n)$ is the Jones matrix of PC and the additional phase difference introduced by the fiber, splicing point, etc. $[C], F_n$ represent the matrix of the coupler with the coupling ration k and the Hi-Bi fiber. The expressions of these parameters are given by (5.3).

$$\begin{gathered} [C] = \begin{bmatrix} \sqrt{k} & j\sqrt{1-k} \\ j\sqrt{1-k} & \sqrt{k} \end{bmatrix}, \quad F_n = \begin{bmatrix} e^{-i\Phi/2} & 0 \\ 0 & e^{i\Phi/2} \end{bmatrix} \\ P(\theta_n) = \begin{bmatrix} \cos\theta_n & \sin\theta_n \\ -\sin\theta_n & \cos\theta_n \end{bmatrix}, \quad P(-\theta_n) = \begin{bmatrix} \cos\theta_n & -\sin\theta_n \\ \sin\theta_n & \cos\theta_n \end{bmatrix} \end{gathered} \tag{5.3}$$

where θ_n is the rotation angles introduced by the PC and other elements in the loop. The phase difference 'Φ' of the two polarization modes after passing an Hi-Bi fiber is expressed by equation (5.4) [9].

$$\Phi = 2\pi B(\lambda)L/\lambda \tag{5.4}$$

where L is the length of the Hi-Bi region. For the 4-hole SC microcell, the length of the transitions are not counted in L because the fiber core size is larger in transition and so possesses a much lower birefringence according to the relation in Figure 55(a). Therefore L can be approximately expressed as the length of the waist.

Ignoring the insertion loss of the coupler and the attenuation introduced by the other elements in the loop, the transmittivity T and reflectivity R of the Sagnac loop interferometer in (5.5) and (5.6) can be obtained.

$$T = \left|E_{2,out}\right|^2 / \left|E_{1,in}\right|^2 = (1-2k)^2 + 4k(1-k)\cos^2(\frac{\Phi}{2})\sin^2(\theta_1+\theta_2) \tag{5.5}$$

$$R = \left|E_{1,out}\right|^2 / \left|E_{1,in}\right|^2 = 4k(1-k)\left[1-\cos^2(\frac{\Phi}{2})\sin^2(\theta_1+\theta_2)\right] \tag{5.6}$$

The transmittivity can be maximized with k=0.5 which represents a 3dB coupler. By adjusting the PC, the term $\sin^2(\theta_1+\theta_2)$ can be set to 1. Equation (5.5) and (5.6) can be simplified to:

$$T = \cos^2(\frac{\Phi}{2}) \tag{5.7}$$

$$R = \sin^2(\frac{\Phi}{2}) \tag{5.8}$$

The maximum transmission and minimum reflection happened when the phase difference satisfies the equation (5.9)

$$\Phi = 2\pi B(\lambda)L/\lambda = (2k+1)\pi, \quad k = 0,1,2\cdots \tag{5.9}$$

The wavelength spacing $\Delta\lambda$ between two adjacent fringe peaks or dips could be related to the group birefringence by equation (5.10) with a first order approximation [9, 10].

$$\Delta\lambda \approx \frac{\lambda^2}{B_g L}, \quad B_g(\lambda) = B(\lambda) - \lambda \frac{dB(\lambda)}{d\lambda} \tag{5.10}$$

Figure 5.6 (a) provides the evolution of a 4-hole SC microcell's transmission spectrum during the fabrication process. By use of the transverse pressurization technique introduced in 3.2.3, the spectrum of the sample can be real-time measured in fabrication. The scan length of the nozzle in the process is 10mm. The cycle numbers in figure (a) represent the in-situ cycle times of the nozzle. The birefringence increase of the sample can be clearly observed. The curve with the densest fringes represents the final status of the sample.

The minor axis length of core (2B) was estimated to be a value in 4-4.5μm (corresponding to the effective minor semi-axis b_{eff} in 1.13-1.27μm) based on the micrograph photo of cross-section. Then the group birefringence B_g and phase birefringence B were numerically calculated based on the models in this region. The lines of B_g and B in Figure 5.6 (b) are the computed results of a microcell with a b_{eff} equal to 1.2μm. The simulated B_g line agrees well with the experimental B_g values (dots in figure (b)) calculated from the fringes' spans by equation(5.10).

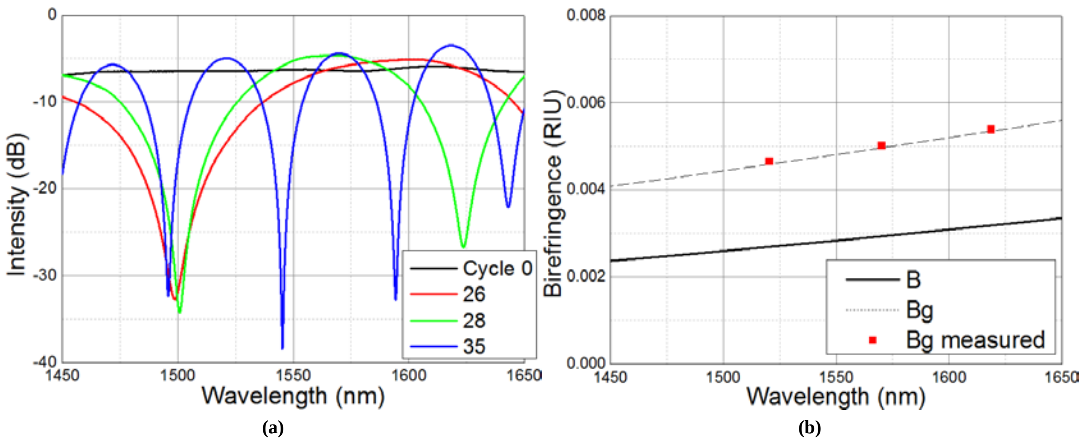

Figure 5.6 (a) Transmission spectra of a 4-hole SC microcell in fabrication; (b)

Group birefringence B_g and phase birefringence B as functions of wavelength for the microcell sample

According to previous discussion, the Sagnac interferometer configuration provides a reliable method by which to measure the birefringence of the Hi-Bi fiber. In the following sections, this configuration will be used to build sensors for temperature and gas pressure.

5.2.2 Temperature sensing

To measure the temperature response of the Hi-Bi microcell, the configuration in Figure 5.7 can be adopted. The instruments used in the configuration include a broadband source (BBS) (Amonics ALS-CWDM-FA), a polarization controller (PC), a 3dB coupler, an optical spectrum analyzer (OSA) (Yokogawa AQ6319), and a digitally controlled column oven (ECOM LCO 102).

In the 3dB coupler, the light from the BBS is split into two counter-propagating parts which pass the microcell in the oven from opposite directions. The fringe of transmission spectrum is recorded by the OSA. The sample in the experiment is produced with the same fabrication parameters as the one in Figure 5.6.

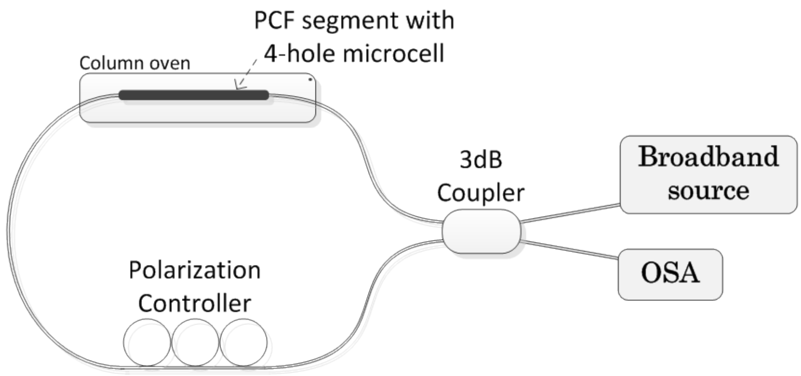

Figure 5.7 Schematic of the setups for measuring the temperature response of the 4-hole SC microcell

The shift of the dip wavelength of the 4-hole SC microcell in the Sagnac interference configuration is ~0.8 pm/°C. This is quite a low temperature sensitivity value which is comparative to most single material Hi-Bi MOFs [11, 12]. However, as discussed later in section 6.1, the 4-hole SC microcell is quite sensitive to the RI of the holey region (n_{hole}), especially when the n_{hole} becomes similar to the RI of fiber material. If a liquid with a high RI-temperature coefficient is infiltrated into the holey region of a microcell, the microcell can become highly sensitive to environmental temperature.

In experiment, the RI oil (Gargille Co.) with n=1.3 and a temperature coefficient dn_D/dt = 3.34 x10^{-4} RIU/°C was infiltrated into the microcell via small holes opened by the fs laser pulse on the jacket tube. The dip wavelength spacing became much wider when the core was immersed in the oil than in the air. As demonstrated in Figure 5.8, the spacing expands from 50nm to 162nm after the infiltration of oil. The oil with the higher RI was not adopted so as to avoid the too-wide dip spacing which would exceed the observation windows of wavelength.

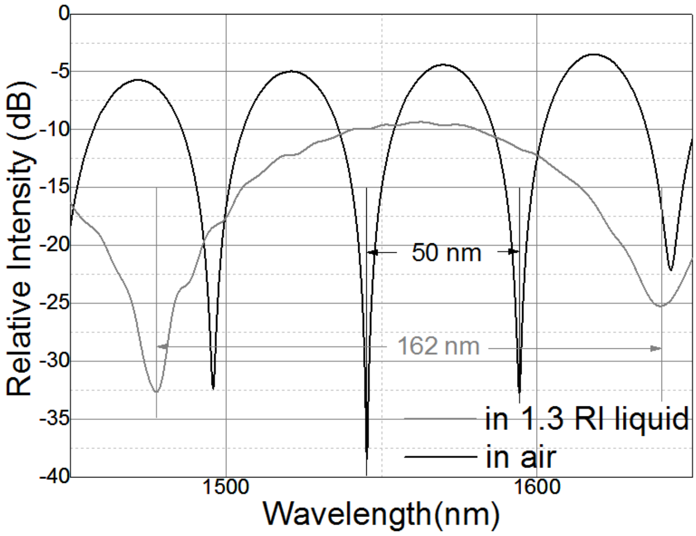

Figure 5.8 The transmission spectrum of the Sagnac interferometer before (black line), and after (gray line) the oil infiltrated into the microcell

The temperature response of the liquid infiltrated microcell was measured in the range from 25°C to 85°C with a 5°C step. The results are provided in Figure 5.9.

The transmission spectrums of the interferometer with different microcell temperatures are demonstrated in (a) and (b) with the central dip marked by a circle. From the wavelength response of the temperature in (c), the temperature sensitivity of the sensor is ~3.04 nm/°C (corresponding to an RI sensitivity of ~9.1 x10^3 nm/RIU).

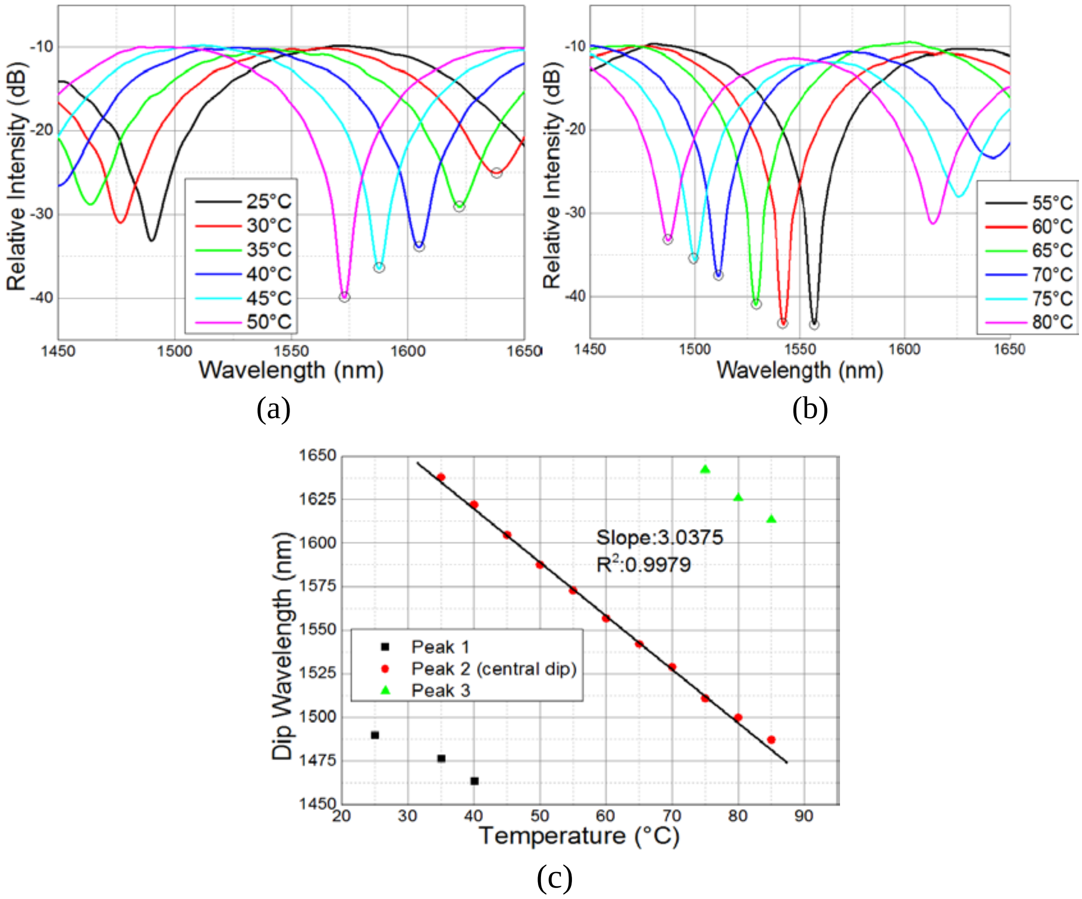

Figure 5.9 (a), (b) The transmission spectrums of the interferometer with temperatures from 55°C to 80°C with 5°C step; (c) The wavelength of the dips as a function of temperature

The RI sensitivity of the 4-hole SC microcell sensor can be calculated by equation (5.11) which is derived from (5.4) [7]. It suggests that the S_n is related to both the liquid induced birefringence variation $\partial B / \partial n$ and the group birefringence B_g.

$$S_n = \frac{d\lambda}{dn} = \frac{\lambda \cdot \partial B / \partial n}{B - \lambda \partial B / \partial \lambda} = \frac{\lambda}{B_g} \frac{\partial B}{\partial n} \tag{5.11}$$

The sensitivity curves at 1550nm for the microcell with n_{hole} =1 and 1.3 are provided in Figure 5.10 based on a numerical simulation performed by means of an FEM. The calculated curve agrees well with the experimental results. Figure 5.10 can also predict that the sensitivity would increase significantly when the minor axis length approaching 2.36 μm and 1.4 μm for the condition of liquid-filled and gas-filled cell, respectively.

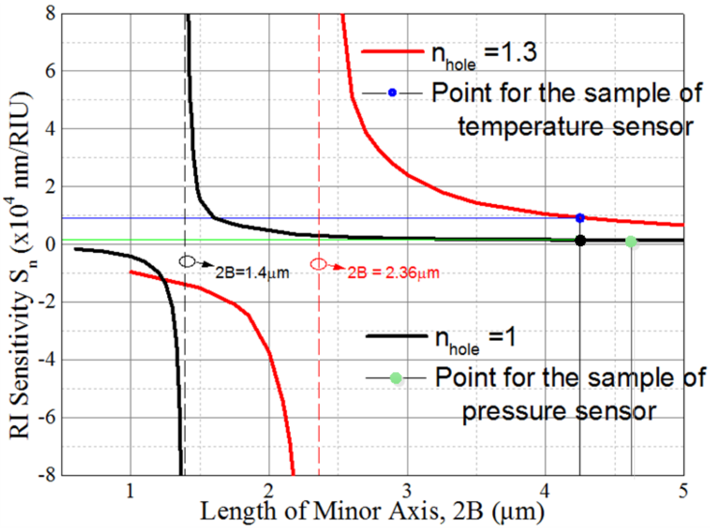

Figure 5.10 Calculated RI sensitivity at 1550nm as a function of the core's minor width (2B) for the microcell with n_{hole} = 1 (black line) and 1.3 (red line). The measured points in the experiments are marked

5.2.3 Pressure sensing

The microcell's feature of being highly sensitive to the RI variation around the core enables the possibility of a gas pressure sensor based on the change of gas RI with pressure. Figure 5.11 provides the experimental configuration which is similar to the configuration for the temperature sensor in Figure 5.7. Differently, the sample in this configuration is sealed in a glass tube which is a small gas cell for pressurization.

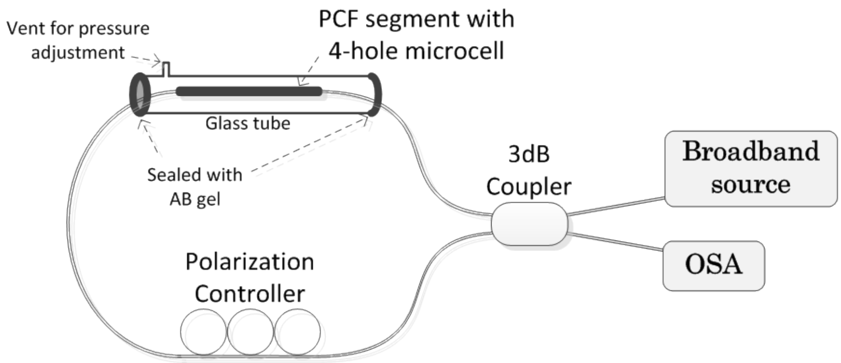

Figure 5.11 Schematic of the setups for measuring the pressure response of the 4-hole SC microcell

The photo of the gas cell is provided in Figure 5.12. A tee tube is used to connect the input tubes and the pressure chamber with the same bore size (~0.9mm) but a different length. To minimize the influence of axis extension force when gas pressure is applied to the cell, the length of the pressure chamber is chosen with much longer than the length of microcell and the fiber is sealed in the chamber loosely. Side-holes were opened on the microcell by a focused fs laser to make the applied pressure reaching the core region of the microcell.

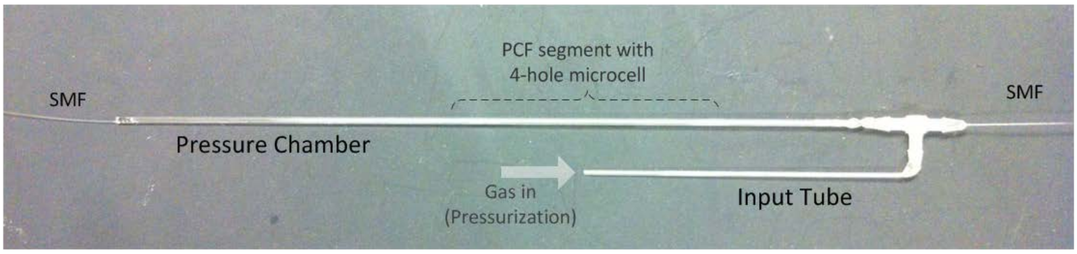

Figure 5.12 Photo of the gas cell for pressure sensor

Pure nitrogen gas was used to pressurize the chamber. To create a nearly all nitrogen circumstance to the microcell, the air in the chamber was dispelled by the nitrogen flow before the entrances were sealed. For nitrogen, the RIs of any two conditions of temperature and pressure can be described by the equation (5.12) which is derived from the Lorentz-Lorenz formula [13].

$$\frac{n_1-1}{n_2-1}=\frac{P_1T_2}{P_2T_1}\frac{Z_2}{Z_1}\left[1+\frac{n_1-1}{6}(1-\frac{P_2T_1}{P_1T_2})\right] \tag{5.12}$$

where P_i, T_i are, respectively, the gas pressure in unit Pascal and temperature in unit Kelvin. Z is the nitrogen's compressibility as expressed by the empirical formula (5.13).

$$Z_i=1-\frac{P_i(317.6-T_i)\times10^{-5}}{101325} \tag{5.13}$$

The RI n_1 = 1.00027907 detected at wavelength 1.53 μm, and temperature T_1 = 288 K is used for calculation. The dispersion in the nitrogen is little (Δn ≈ 3 x10^{-7} from 1350 nm to 1690 nm) and will be neglected in the discussion [14]. The calculated RI-pressure coefficient at 20 °C is ~2.7 x10^{-4} RIU/Bar.

The pressure response of a microcell in a range from 1 to 9 Bar with step of 1 Bar is given in Figure 5.13. In figure (a) is the transmission spectrums of the interferometer under different chamber pressures. From figure (b) which shows the change of dip wavelengths respond to the pressure, the pressure sensitivity of the sensor is ~0.31 nm/Bar (corresponding to RI sensitivity ~1.5 x10^3 nm/RIU). The RI sensitivity can meet the theoretical prediction by the black line in Figure 5.10. The pressure sensitivity of this sample is slightly lower than the Hi-Bi PCF pressure sensor based on the pressure-birefringence effect [15]. However, the sensitivity of this design can be improved by applying a microcell with a smaller core.

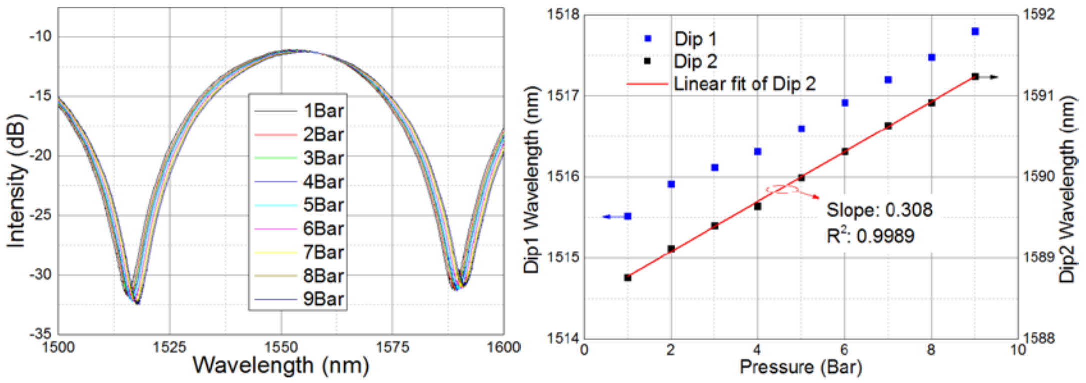

(a) (b)

Figure 5.13 (a) The transmission spectrums of the interferometer under *different chamber pressures from 1 Bar to 9 Bar; (b) The wavelength of the dips as a function of pressure*

5.3 Summary

In this Chapter, the characteristics of the 4-hole SC microcell have been discussed. The birefringence of the microcell's fundamental mode exhibits a high sensitivity to the RI around the core of cell. Based on the property, a temperature sensor and a pressure sensor are demonstrated. The sensitivities are ~3.04 nm/°C (corresponding to an RI sensitivity of ~9.1 x10^3 nm/RIU), and ~0.31 nm/Bar (corresponding to an RI sensitivity of ~1.5 x10^3 nm/RIU), respectively.

5.4 References

[1]. T. Nasilowski, T. Martynkien, G. Statkiewicz, M. Szpulak, J. Olszewski, G. Golojuch, W. Urbanczyk, J. Wojcik, P. Mergo, and M. Makara, "Temperature and pressure sensitivities of the highly birefringent photonic crystal fiber with core asymmetry," Applied Physics B **81**, 325-331 (2005).

[2]. X. Wang, and S. Li, "Design of flat-top comb filter based on photonic crystal fiber Sagnac loop," in *SPIE/OSA/IEEE Asia Communications and Photonics*(International Society for Optics and Photonics, 2011), pp. 83071M-83071M-83077.

[3]. M. Pang, L. Xiao, W. Jin, and A. Cerqueira S, "Birefringence of hybrid PCF and its sensitivity to strain and temperature," Journal of Lightwave Technology **30**, 1422-1432 (2012).

[4]. T. Martynkien, G. Statkiewicz-Barabach, J. Olszewski, J. Wojcik, P. Mergo, T. Geernaert, C. Sonnenfeld, A. Anuszkiewicz, M. K. Szczurowski, and K. Tarnowski, "Highly birefringent microstructured fibers with enhanced sensitivity to

hydrostatic pressure," Opt. Express **18**, 15113-15121 (2010).

[5]. J. R. Folkenberg, M. D. Nielsen, N. Mortensen, C. Jakobsen, and H. R. Simonsen, "Polarization maintaining large mode area photonic crystal fiber," arXiv preprint physics/0403043 (2004).

[6]. O. Frazao, J. Baptista, J. Santos, J. Kobelke, and K. Schuster, "Strain and temperature characterisation of sensing head based on suspended-core fibre in Sagnac interferometer," Electronics Letters **44**, 1455-1456 (2008).

[7]. J. Li, L.-P. Sun, S. Gao, Z. Quan, Y.-L. Chang, Y. Ran, L. Jin, and B.-O. Guan, "Ultrasensitive refractive-index sensors based on rectangular silica microfibers," Optics Letters **36**, 3593-3595 (2011).

[8]. T. Birks, and P. Morkel, "Jones calculus analysis of single-mode fiber Sagnac reflector," Applied Optics **27**, 3107-3113 (1988).

[9]. A. Ortigosa-Blanch, J. Knight, W. Wadsworth, J. Arriaga, B. Mangan, T. Birks, and P. S. J. Russell, "Highly birefringent photonic crystal fibers," Optics Letters **25**, 1325-1327 (2000).

[10]. H. Xuan, W. Jin, M. Zhang, J. Ju, and Y. Liao, "In-fiber polarimeters based on hollow-core photonic bandgap fibers," Optics Express **17**, 13246-13254 (2009).

[11]. T. K. Noh, and Y. W. Lee, "Temperature-Insensitive Polarimetric Fiber Strain Sensor with Short Polarization-Maintaining Photonic Crystal Fiber," Applied Physics Express **5**, 2502 (2012).

[12]. C.-L. Zhao, X. Yang, C. Lu, W. Jin, and M. Demokan, "Temperature-insensitive interferometer using a highly birefringent photonic crystal fiber loop mirror," Photonics Technology Letters, IEEE **16**, 2535-2537 (2004).

[13]. U. Griesmann, and J. Burnett, "Refractivity of nitrogen gas in the vacuum ultraviolet," Optics Letters **24**, 1699-1701 (1999).

[14]. M. J. Weber, *Handbook of optical materials* (2002).

[15]. H. Fu, H. Tam, L.-Y. Shao, X. Dong, P. Wai, C. Lu, and S. K. Khijwania,

"Pressure sensor realized with polarization-maintaining photonic crystal fiber-based Sagnac interferometer," Applied Optics **47**, 2835-2839 (2008).

Chapter 6 : The 3-hole Microcell - Properties and Applications

In this chapter, the advantages of the 3-hole suspended core (SC) microcell are discussed. Based on this kind of microcell, a novel in-line gain cell is demonstrated. Furthermore, we also inscribed a high quality long period grating (LPG) on the core of this type of microcell. Temperature response of the LPG is measured.

6.1 Characterization

Research on the SCFs with core surrounded by three holes have been conducted for years. Figure 6.1 demonstrates some typical structure of such kind of SCFs. (a) demonstrates the first 3-hole SCFs fabricated with SD57 glass with high lead concentration. The extrusion technique is also the first time used in producing the preform for (a). (b) and (c) are the typical 3-hole SCFs with submicron sized core reported in recent years for the applications in supercontinuum generation, evanescent field sensing etc. By applying the modified fiber-drawing technique, Liao et al produced the SCF in (c) with ~60 diameter ratio of hole-region to core (DRHC).

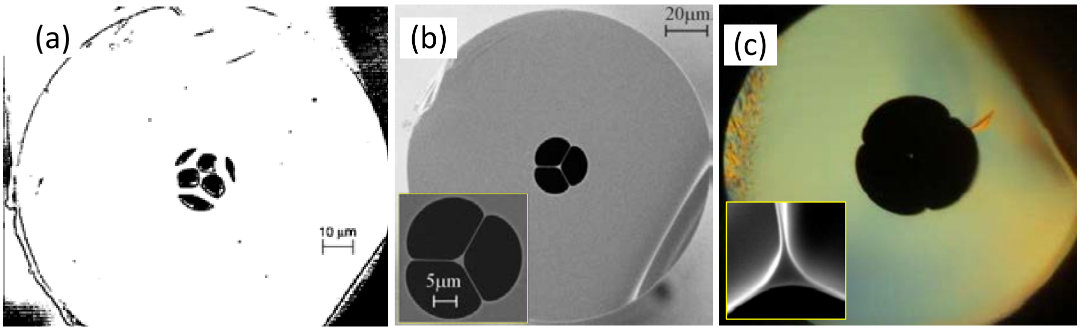

Figure 6.1 The cross-section of typical 3-hole SCFs reported by (a) Kiang et al [1], (b) Heidepriem et al [2] and (c) Liao et al [3]

Most research activities on the 6-hole SCFs have been concerned with the guidance properties, such as evanescent field sensing, abnormal dispersion and supercontinuum generations [2, 4-6]. Compared with the other SCFs with three holes in Figure 6.1, the advantages of the 3-hole SC microcell include (a) low loss connection to the SMF systems, (b) large hole-regions, (c) fundamental mode propagation in the multimode SC region because of the adiabatic transitions to the ESM PCF at both sides, and (d) thin jacket tube. These distinguishing features enable the 3-hole microcell can be applied in many novel applications

Compared with the other types of SC microcells, the 3-hole microcell is more suitable for building the microcell with smaller core dimension. This could be explained with the aid of Figure 6.2 which demonstrated the initial deformation statuses of the 6-, 4- and 3-hole SC microcells respectively. The arrows in figure represent the direction and magnitude of the initial deformation. The dark holes are the pressurized holes in microcell fabrication. The closed curve in core-region is the contour of displacement field with value 1.5 $\times 10^{-3}$ nm, which is a very low displacement level. So the core region enclosed by the contour would experience little deformation in fabrication, and the enclosed area would be approximately proportional to the core area of target microcells. In all three models, 3-hole model has the smallest core region enclosed. This roughly analysis predicts a smaller core of 3-hole SC microcell.

Actually the generation of microcell cores is a complicated procedure which will be influenced by the expansion, collapsing rate of air holes and the pulling rate in the fiber axial direction. The smallest core diameter realized in experiment is ~1.6 μm for 3-hole structure. Based on a small core 3-hole microcell, we built an optical gain cell by transversely pumping the laser dye in microcell. The design and experiments will be provided in section 6.2.

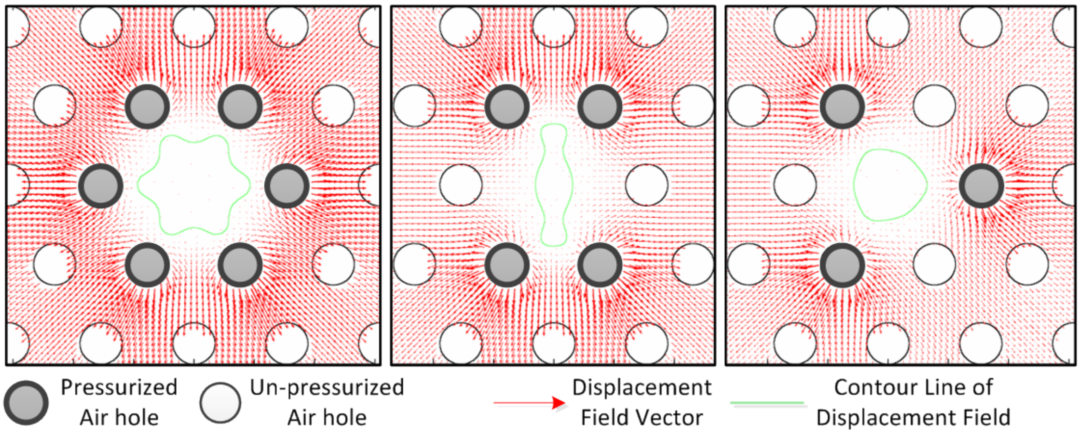

Figure 6.2 The initial displacement fields of the 6-, 4- and 3-hole SC microcells based on ESM-12 with pressure 5Bar

In addition, the 3-hole microcell has the largest angle (120°) between two struts than other types of microcells (refer to the Figure 6.3). So the fiber core can be observed and processed from the transverse direction with the least influences by the struts. Base on this feature, the long period grating (LPG) can be inscribed on the pure silica core of microcell. The details of LPG will be introduced in section 6.3.

Figure 6.3 (Right) Side view graph of a 3-hole microcell observed from the direction marked in the (Left) diagram

6.2 In-line Optical Gain Cell

Since a large portion of the guided light can be located in holes region, the SCFs attracted considerable interests in its potential ability to dramatically improve the performance of the all-fiber devices based on absorption and fluorescence spectroscopy [4, 7-9]. Most of the devices are developed based on the mechanism of evanescent field excitation and collection. To enhance the light-matter interaction region, the SCF with large effective mode area, high RI (but lower than core material's RI) in holey region, and long reactant infiltration region is preferred. 3-hole SC microcell is a good candidate to this kind of applications due to the small core size. In this section, the development of an in-line optical gain cell based on laser-dye solution infiltrated 3-hole microcells is demonstrated.

6.2.1 Principles

The transvers excitation technique is adopted in building the gain cell. The technique is widely used in pumping the microfluidic dye laser [10-12]. It is compact, high efficient and simple in setup. The pump laser is expanded to a beam with large diameter and focused onto the fiber via a cylindrical lens. The transvers excitation would prior to the longitudinal evanescent field excitation in the following two aspects: Firstly, no requirement to long infiltration region (typically tens of centimeters), which is time-consuming in building and introduces more absorption loss to both the pumping light and fluorescent light. [8] Secondly, the intensity of pump light in the light-matter interaction region is high.

However, the implement of this technique in the SCF-based applications is constrained by following factors. (1) The photo-bleaching phenomenon is notable when most laser dyes are pumped with high intensity light. The phenomenon would severely limit the lifetime of performance of fluorophores in laser dye solution, and cause the fluorescent lights decay rapidly in a dye infiltrated SCF [4]. (2) The aggregation the dye molecules would quench the fluorescence. For example, in the SCF, some types of dye molecules would block the channels by bonding the silica in small part of the fiber and cause remaining length of the fiber is filled only with the solvent [13]. (3) The thermal dissipation would also be problematic when pumped with relative high energy or in continuously working. The fluorescence life time of dye molecules would decrease with increasing in temperature, because the thermal agitated non-radiative processes are more efficient at higher temperatures [14]. Most of these problems can be avoid or alleviated by a regenerating continuous flow of dye through the cavity [10]. However, the continuous dye flow was impossible in the design, in which the capillary forces were used to pull the dye into the air-columns of SCFs.

Figure 6.4 is the schematic of the gain cell structure in our experiments. The laser dye solution can continuously circulate in the microcell with the aid of gas pressure. The structure consists of 3 microcells in series and spliced to SMF at both end. A longer microcell can also be adopted for the application. However the former design is easier in fabrication. The entrance and exit of laser dye solution are micro-holes on the short microcells drilled by fs laser pulse. Since all microcells are fabricated in a same PCF with same hole-selection pattern, the selected air-columns are in connection among all microcells. By applying pressure or vacuum on the entrance or exit, the dye solution will run continuously in the PCF. In the unprocessed PCF region, only few air-columns connected to the microcell contain laser dye in them. The pump laser beam is expanded to ~1 cm in width, and then focused onto the center of long microcell.

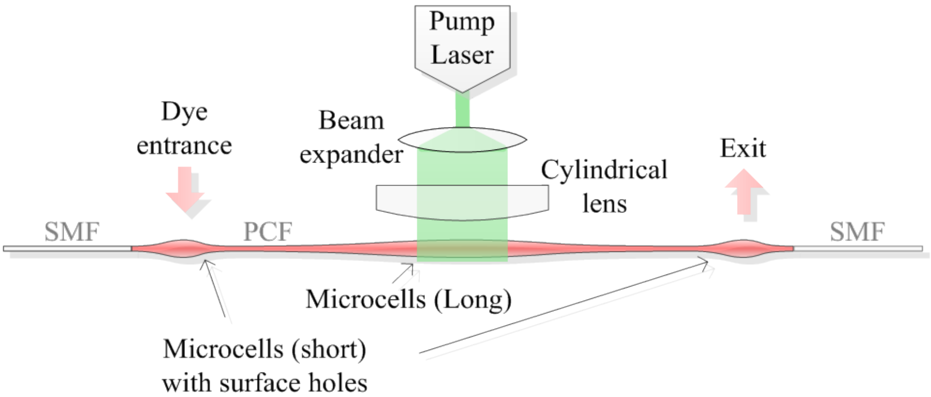

Figure 6.4 Schematic of optical gain cell

This structure is suitable for building in-line gain device because (a) low loss in adiabatic transitions and connections. (b) Continuously flowing gain medium, i.e. dye solution, in the light-mater interaction region, so the problems of photobleaching, molecule aggregation, and thermal dissipation can be avoid or alleviated. (c) The hole-regions of the long microcell are larger than most MOFs. So a larger amount of gain medium interacts with the pumping light in cells. (d) The thin jacket tube of long microcell enables the less scattering and absorption of the pumping light. Our first step in applying this structure is to build an optical gain cell in visible wavelength range. Following aspects should be taken in consideration in building the gain cell.

Microcells properties

Compared with the core dimension in evanescent-field-based gas sensing applications, the SCFs with relative larger core size can be used in fluorescent excitation and collection applications. Because when the fiber core is immerged in liquids with higher refractive index (RI), the evanescent fields extend further into the surroundings, so the light-matter interaction region is enlarged.

To represent the spatial scales of light-matter interaction region in SCFs, the effective area A_{eff} defined by (6.1) is commonly used [4].

$$A_{eff} = \frac{\left(\iint_A \mathrm{Re}\left\{\left(E\times H^*\right)\cdot u_z\right\} dA\right)^2}{\iint_A \left(\mathrm{Re}\left\{\left(E\times H^*\right)\cdot u_z\right\}\right)^2 dA} = \frac{\left(\iint_A S_z dA\right)^2}{\iint_A \left(S_z\right)^2 dA} \tag{6.1}$$

where S_z is the z component of the Poynting vector. A represents the whole area of the cut plane which is perpendicular to the fiber axis.

The effective mode areas of 3-hole microcells at 630nm wavelength with various core dimensions were calculated with the finite element method (FEM). The results are summarized in Figure 6.5. The solid lines represent the A_{eff} -r_{eff} relations with the hole-region RI equal to 1, 1.33 and 1.43 respectively. The dash line represents the effective boundary between core and hole-region. The portion of mode field beyond the boundary is available for light-matter reaction. In all RI condition, the mode area decreases as the core size decreases at first, and then exceed the boundary and largely increases after reaching a minimum when the radius continuously decreases. For a same core size, the confinement of the modes is alleviated in a high RI environment. So the microcell with higher RI in hole-region would have a larger mode area. According to the Figure 6.5, the microcells with ~ 1 μm core radius can exhibit large light-matter interaction region when the holes are infiltrated with high RI liquid.

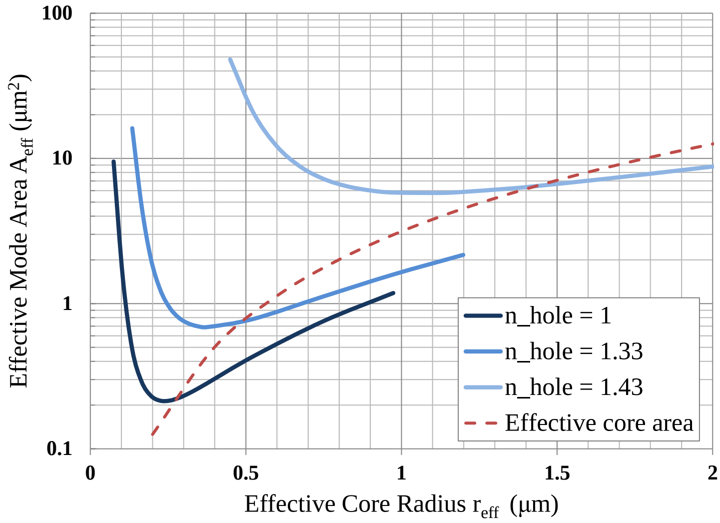

Figure 6.5 Effective mode areas of the fundamental mode in 3-hole SC microcell as a function of the core radius with different RI in hole-region (n_hole)

The cutoff condition of SC microcell will also be influenced by the RI of hole-region. The solid and dash curves in Figure 6.6 are the dispersion curves of the fundamental mode and the nearest higher order modes respectively. If the microcells are filled with higher RI materials, the cutoff wavelengths of the fundamental mode and high order modes will shift towards the higher frequency direction. So the single mode operation could be realized in the microcells with larger core dimension. This is useful for fluorescent absorption applications because the suppression of high order modes might result more fluorescent light coupled into the propagating fundamental mode.

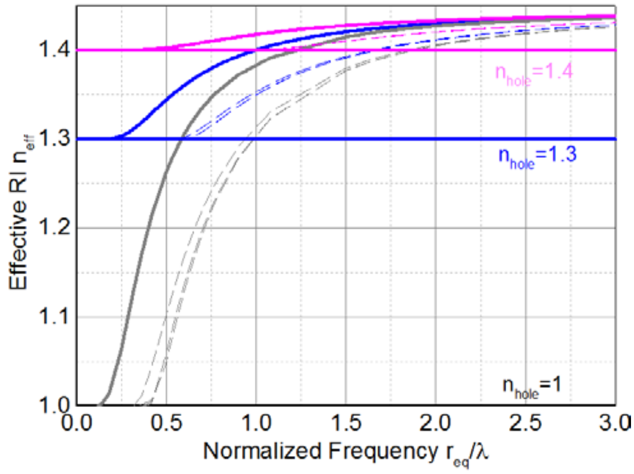

Figure 6.6 The dispersion curves of 3-hole microcell with hole-regions possess different RI

Dyes and solvents properties

Following aspects should be considered in designing the dye solutions for microcell: types of (laser) dye and solvent, wavelength, power and duration of pump light, solution concentration.

Dyes are fluorescent chemical compounds that can re-emit light upon light excitation. Compared with the inorganic dyes, the organic dyes emit light covering the wavelength from UV to far infrared region and are the first choice for our gain cell application. The fluorophores of organic dyes are complex molecules containing long chains of conjugated double bonds ($[-C=]_n$). The large molecular size and the delocalized π-electrons in the conjugated double bonds give rise to the large dipole moments (or oscillator strengths) of dye molecules. The complex molecular structure leads to many vibrational and rotational levels within a single electronic state. Therefore, laser dyes often have strong, wide-band absorption and emission.

The organic dye is a big family usually contain 3 major classes divided by emission wavelength range: [15]

(a) Coumarin: (emitting in the 400-500 nm region). The core structure is 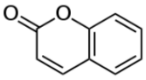. Different spectrums are produced by substituting the 7-position of core structure with auxochromes such as –OH, $–OCH_3$, $–NH_2$, $–NHCH_3$, $–N(CH_3)_2$ and other electron-donating substituents.

(b) Xanthene: (emitting in the visible region from yellow to red). The core structure is 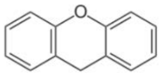. Include pyronins, eosins, rhodamines and some other derivative, such as Oxazine.

(c) Polymethine: (emitting in the 0.7 -1.5 um region). This kind of dye contains a chain composed of an odd number of methine groups (=CH-) with conjugated double bonds. Include cyanine, Merocyanine (DCM), Pyridine, et al.

The rhodamines 6G(590) in class (b) may be the most widely used fluorescent material in organic dye research, because of high quantum efficient (can reach 0.95), little dependent on temperature and easy to get [16]. Rhodamine 6G from the Exciton Co was used in our experiment.

To explain the optimization procedure of dye solution, the mechanism of a typical organic dye will be introduced with the aid of the energy level diagram (Figure 6.7). S_1 and S_2 are the ground and first excited singlet state, T_1 and T_2 are the first and excited triplet state respectively.

The singlet states region illustrates the common pumping and emission processes of a four-level laser system. The decay of the light emitted in the singlet states region, i.e. fluorescence, is governed by the emission lifetime τ_{sp}, which is in a nanosecond level. The gain of the dye is the result of the stimulated emission process with same time scale. The stock shift of emission peak wavelength is determined by the energy loss of the non-radiative decay processes in S_0 and S_1.

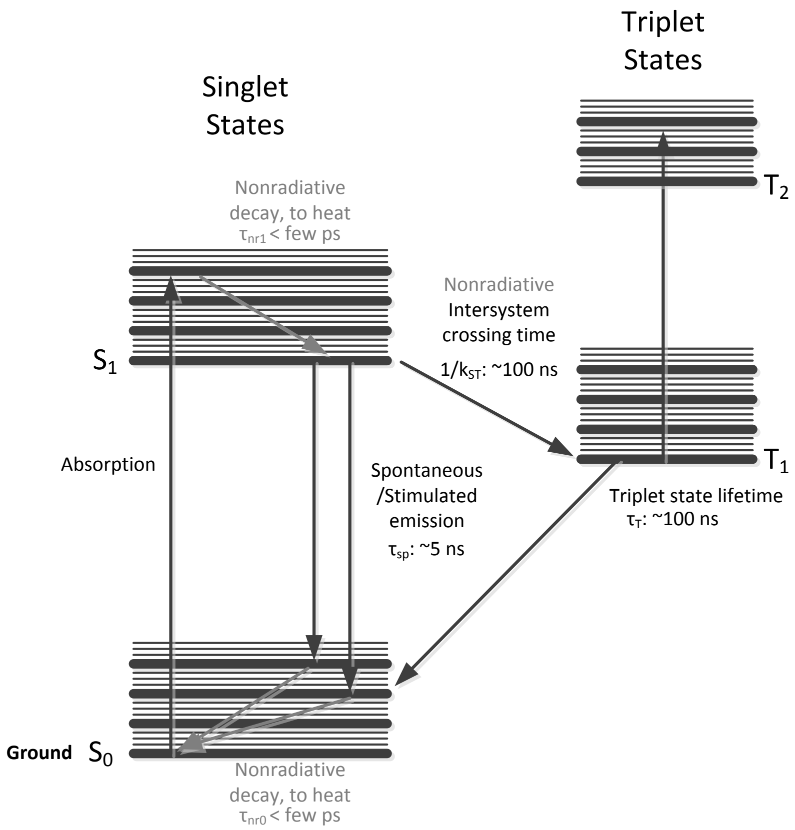

Figure 6.7 General energy level diagram of a typical organic dye

When the dye molecules are in the states S_1, although spin-forbidden, it is also largely possible to decay to the metastable triplet state T_1 (Spin-orbit coupling) via collisions. Due to the selection rules, the nonradiative intersystem crossing S_1->T_1 has a much slower transient time ($1/k_{ST} \approx 100$ nanoseconds) than the in-singlet transition processes. The decay process T_1 -> S_0 can be radiative (phosphorescence) or nonradiative. The long time scale intersystem crossing will attract large amount of excited molecule. In addiiton, while the molecule is in the lowest level of T_1, it can also absorb radiation to undergo the T_1 -> T_2 transition.

The transitions via triplet states compete with fluorescence during deactivation of S_1. This competition is detrimental to the operation of dye for two aspects. First, the trapped dye molecules in T_1 will decrease the available population inversion. Second, the absorption spectrum of T_1 -> T_2 transition is always concurrent with the singlet emission spectrum. [11, 15, 17]

According to the background information, the keys to obtain gains, i.e. stimulated emission, in dye solution are increasing the molecules in S_1 states (population inversion) and depressing the transition via intersystem crossing.

To excite more dye molecules to S_1 state, a high power laser is more efficient than the flashlamp, because laser spectrum is narrow, therefore all the light power can be tuned to the most efficient absorption wavelength. The 532nm Nd:YAG laser are widely used in rhodamine 6G research. Nevertheless, the photobleach effect of dye molecules become serious when pumped with higher power density pump light. The bleached dye molecules exhibit temporarily or permanently degeneration of the efficiency in emission. [18] A commonly method to avoid the beaching is circulating the dye solution.

To depress the intersystem crossing, three methods can be adopted. The first one is utilizing the pump laser with few nanoseconds pulse duration to depress the large time-scale intersystem crossing [19]. The second one is adding triplet quencher molecules, such as COT (cycloctatetraene), oxygen molecule and nitrogen molecule, into the dye solution. The third one is depopulate the triplet automatically by use of particular combinations of dye and solution. The last method was used in building the gain cell. Since the dye had been decided, i.e. rhodamine 6G, the ethylene glycol (EG) was a suitable solvent. [20]

Compared with other widely used solvents for rhodamine 6G, such as ethanol [21] and methanol [22, 23] listed in Table 6.1, the EG is suitable to our gain cell application in many more aspects besides the automatic triplet quenching property. (1) The RI of EG at wavelength ~600nm is very close to the RI of silica, as discussed in previous part, the property enable a large-light matter interaction region in the microcell. (2) The high (negative) dispersion of EG in visible region makes the EG's RI exceed silica's at lower wavelength, so the pump light is not guidable in the gain cell. (3) The high viscosity of EG would helpful to generate stable stream in the circulation channels [24].

Table 6.1 Properties of the commonly used solvents for rhodamine 6G [25]

Name	Molecular Formula	Viscosity at 25°C	Refractive Index	
		mPa·s	$N20_D$ [a]	$dn_D/d\lambda$
Ethylene Glycol **(EG)**	$C_2H_6O_2$	16.1	1.4318 [b]	-0.175 (μm^{-1})
Ethanol **(EtOH)**	C_2H_6O	1.2	1.3611 [b]	-0.031 (μm^{-1})
Methanol **(MeOH)**	CH_4O	0.59	1.3288 [c]	-0.124 (μm^{-1})

a. 20°C, 589.3nm;
b. data from .

A concentration of rhodamine 6g solution located in the 10^{-4} to 10^{-2} M (mol/L) is always adopted in dye laser applications [17, 19, 26]. However, at high concentration, the dye solution experiences a self-quenching of the emission due to the formation of dimers or other quenching complexes which have fast nonradiative de-excitation channels. In our experiments, a moderate concentration 3 mM (millimole per liter) was used.

Taking into account the above considerations, the rhodamine 6G EG solution (3mM) was used as gain medium for the gain cell fabrication. The absorption and fluorescent spectra of the dye solutions in Figure 6.8 were measured by using high resolution spectrometers (Ocean optics HR400). The fluorescent spectrum was measure by direct pumping the dye solution in a 1 cm quartz cuvette by a continue wave (CW) 532nm Nd:YAG laser. The absorption spectrum was measured by use of a halogen lamp (500-1000 nm). The absorption peak of dye solution is ~532 nm, which enable a high efficient pumping by the Nd:YAG laser. The emission peak of 3mM dye solution is ~563 nm. The peak experiences a small blue shift with decreasing the concentration of solution.

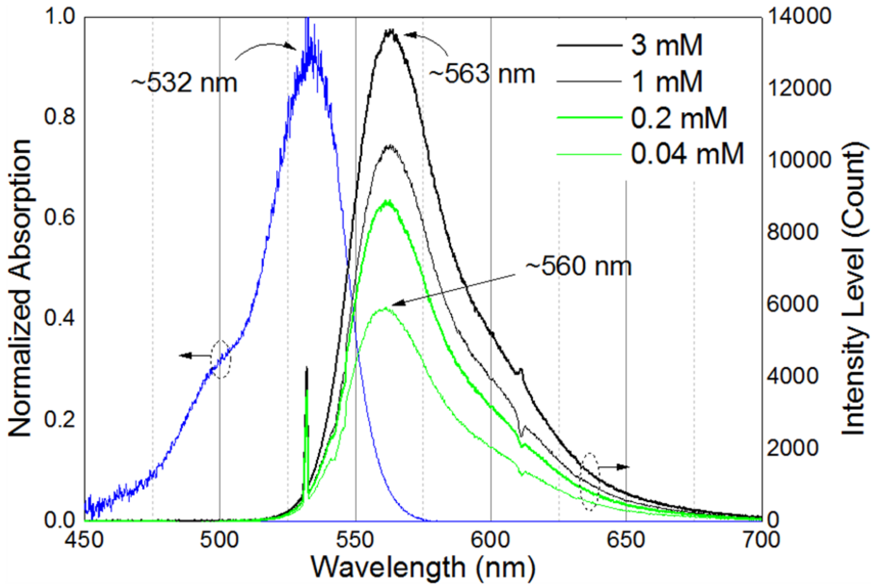

Figure 6.8 The Absorption and fluorescence spectra of rhodamine 6g (EG) solution in our experiments

6.2.2 Fabrication of the dye cell

The schematic of the dye cell are provided in Figure 6.9. The whole structure consists of 2 short microcells, 1 long microcell and 2 tee tubes. All of microcells are 3-hole SC microcells fabricated in series on a LMA-10 PCF. Two pieces of SMFs are connected to the structure at both ends. When the SMF-microcell-SMF structure is ready, small holes are drilled at the surface of each short microcell. Then the short microcells are sealed into two separate tee tubes. So the open ports of each tee tube can serve as the entrance and exit respectively.

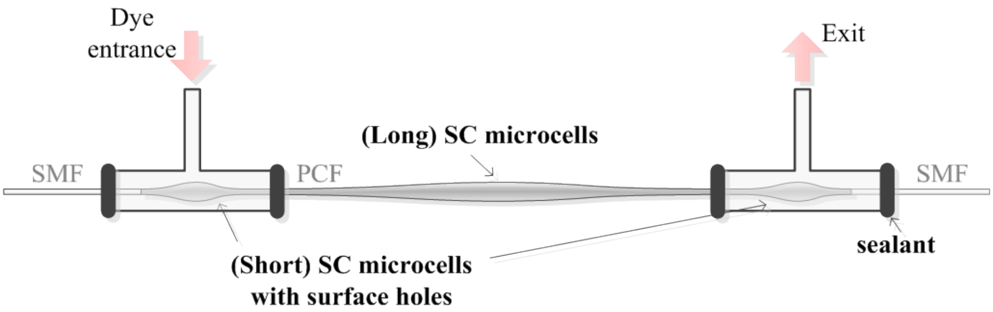

Figure 6.9 Schematic of the dye cell

Figure 6.10 (a) is the overall photos of a gain cell. The short microcells are sealed inside two tee-tubes. The glass tube connected to the up-port of left tee-tube is the entrance of the dye solution and gas pressure. The other two port of left tee-tube are blocked with glue. So the dye solution can only run through the microcells when high pressure is applied. The up-port of right tee tube is the exit. Both of the two tee tubes were stuck on a support rod to make the whole structure stable and straight. The waist length of the long microcell was ~10 mm which corresponding to the width of pumping laser beams. The total length of the processed PCF was ~70 mm.

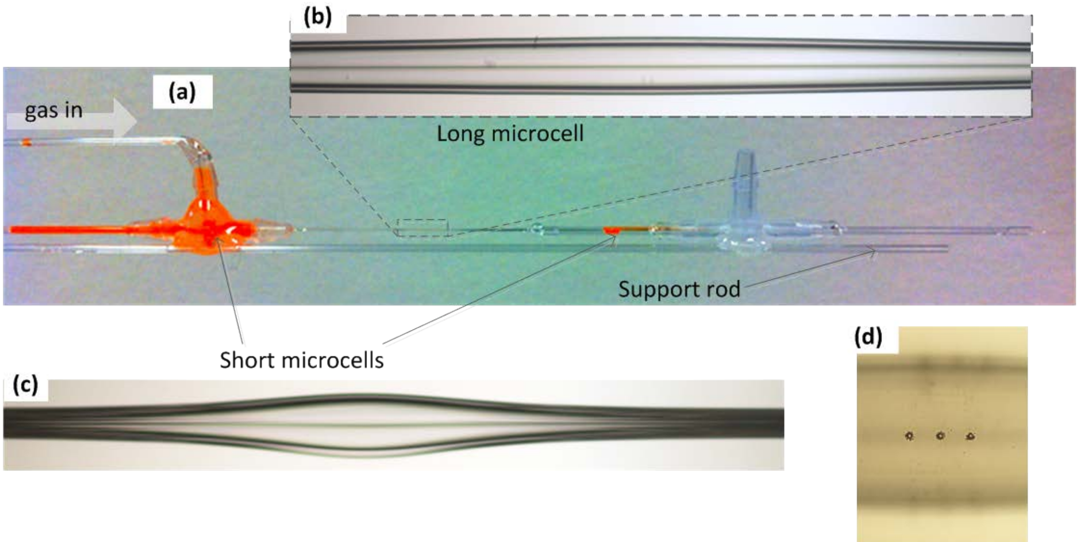

Figure 6.10 (a) Photograph of the Gin cell with rhodamine 6G solution in experiment; (b), (c) Micrographs of the long and short microcell respectively; (d) Micro-holes drilled by the fs laser on the surface of short microcells

The micrographs of the long and short microcells were provided in (b) and (c) respectively. To facilitate observation the outflow of dye solution, the output microcell (short one in right) was one-side sealed in a glass tube and then hermetically connected to the output tee tube. The dye solution was preload into the left tee tube before two horizontal ports blocked. Then the ports are sealed by AB glue, and ~1.5 Bar gas pressure is applied to the left tee-tube to push the dye solution through the microcells. The measured flow rate is ~3 μL/hr (micro liter per hour). In Figure 6.10 (a), the overflow of dye solution can be clearly observed in the right tee-tube. By connecting the output and input ports via a liquid pump, the dye solution would circulate in the structure.

The surface holes on the short microcells are demonstrated in (d). Diameters of the micro-holes are about 4μm. Since the flow rate is constraint by the size of air-columns in PCF, opening more holes won't increase the flow rate of dye solution. However, gas pressure can be used to accelerate the dye solution flow in microcells.

As illustrated in Figure 6.11, the fluorescent spectrum of the rhodamine 6G (EG) solution demonstrates a distinct red shift when in microcell. This phenomenon could be explained by the enhanced reabsorption of the laser dye to the excited emission at short wavelength when the density of fluorophores is high. [27] The wavelength shift is not observed in application with low concentration rhodamine EG solutions (<10^{-6}M) [28].

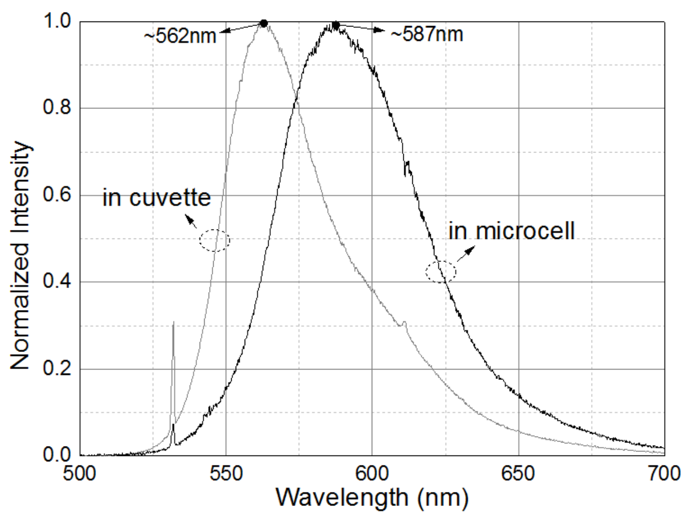

Figure 6.11 Fluorescent emission spectra of the rhodamine 6G (EG) solution in cuvette and microcell

6.2.3 Optical gain measurement

In order to verify the amplification effect of the gain cell to the light, we conducted two experiments on the gain cell with transverse pumping by focused ~100mW 532nm CW Laser. The beam width of the pump laser is approximately 10mm. The microcell is filled with a 3 mM rhodamine 6G (EG) solution.

The first experiment was performed to study the amplification of the microcell to a wide band light. The schematic of the experimental setup is provided in Figure 6.12. A white light LED (Cree Q5) is used as light source. The output spectrum is recorded by a high resolution spectrometer (Ocean Optics HR4000).

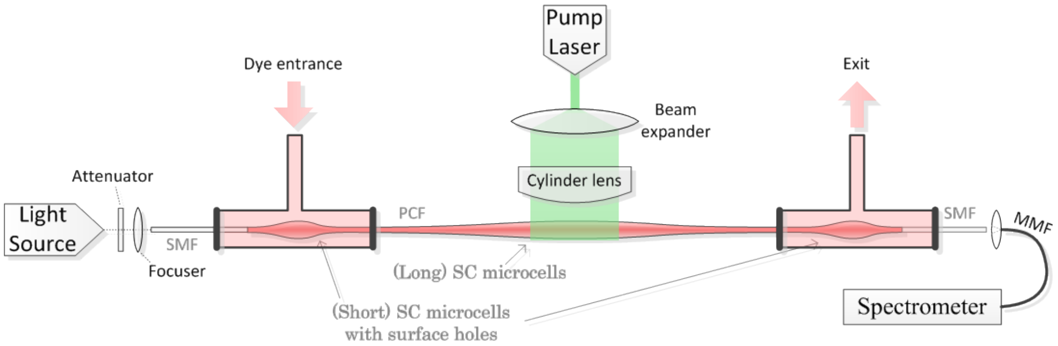

Figure 6.12 Setup for the gain spectra measurement with wide band source

The spectrums of the LED and the fluorescent of dye solution in microcell are recorded in advance. And then the LED light is coupled into the fiber and goes through the gain region when the pump laser is on. The spectrum including fluorescence and amplified LED are illustrated in Figure 6.13(a). The amplified LED spectrum can be extract by deducting the fluorescent light curve (C) from B. The result is provided in Figure 6.13(b). The net gain of the microcell to the LED light is estimated to be a value ~1.2 dB. Since the optical gain **G** is defined as the ratio of the optical density at the output $\mathbf{I_{out}}$ to the optical density at the input $\mathbf{I_0}$, i.e. $G = I_{out} / I_0$, so the loss of the whole structure should be considered. The loss of the whole structure is measure to be ~1.4dB at 1550nm and ~1.7 dB at 600nm. The majorly cause of the losses comes from the connection loss between SMF and PCF. So, actually this sample is failed to obtain optical gain because the loss is larger than the net optical gain.

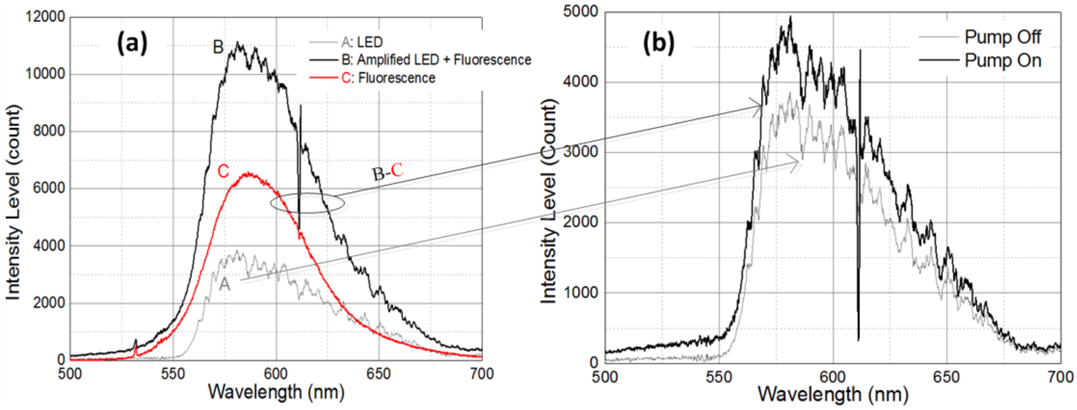

Figure 6.13 (a) The Spectrums of LED, amplified LED + fluorescence, and pure fluorescence; (b) The Spectrums of LED and amplified LED

The Second experiment was performed on another example to study the amplification of the microcell to a narrow band laser. The schematic of the experimental setup is provided in Figure 6.14. A 630nm semiconductor laser is used as light source. Thanks to the red shift of emission spectrum, the microcell has high emission intensity at this wavelength. (Figure 6.11) The output light is detected by a detector for low power (Newport 918-UV). To distinguish the stimulated emission from the influence, i.e. the spontaneous emission, a frequency (~1 Hz) is applied on the drive current of the probe laser. The low frequency is used because the detector and laser are both designed for DC operation, and cannot linearly respond to a higher frequency.

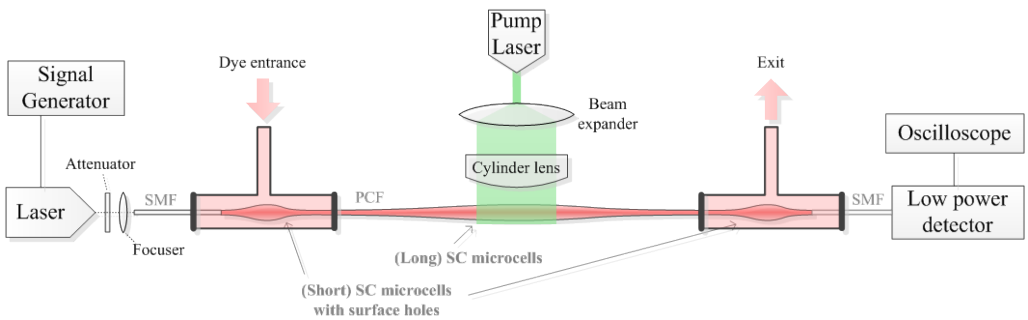

Figure 6.14 Setup for the gain measurement with a laser source

The signal of the probe laser without pumping is the black curve in Figure 6.15. When the pumping is started, the increase in both the DC floor and the AC amplitude can be clearly observed. The DC offset in Figure 6.15 corresponding to the response to the whole fluorescent spectrum. The increasing in V_{pp} is the net gain of the device at 630nm. According to Figure 6.15, the net gain is calculated to be ~2.04 dB. Since the net gain is larger than the loss of this sample (~1.7 dB) at 630 nm, the optical gain ~0.34 dB is obtained by this sample.

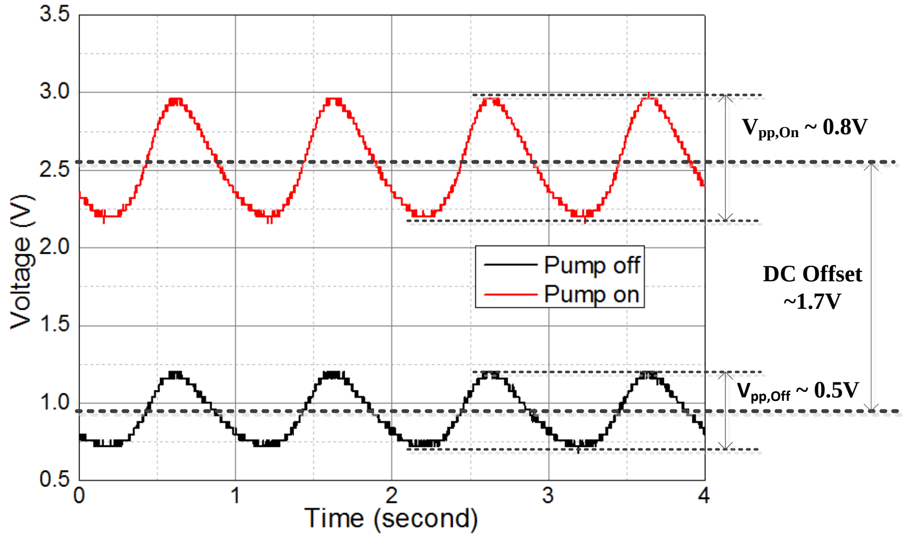

Figure 6.15 Signal of the AC probe light with and without pumping

In this section, we proved the feasibility of the optical gain design and get a positive result. Further research should be conducted. In chapter 7, some suggestion will be proposed for improving the optical gain.

6.3 LPG Inscribed in the SC Microcell

In this section, the LPG inscribed in SC microcell will be introduced. The 3-hole SC microcell is preferred for this application because the 3-hole microcell has a large struts angle (120°) than other types of microcells. This feature enables a wider operation region on the fiber core when the microcell is processed from transverse direction, for example by femtosecond (Fs) laser.

6.3.1 Principles

The fiber LPG refers to a structure with periodic RI perturbation on the core of a fiber. Different to the shot period grating, such as fiber Bragg grating (FBG), LPG is a transmission grating which couples the core mode of fiber to the co-propagation cladding modes or the other higher order core modes, and leads to attenuation bands to the fiber transmission spectrum at the wavelengths which the coupling happens. The coupling between fundamental and higher-order modes is determined by the phase matching condition

$$\lambda_{res} = (n_{eff}^{0} - n_{eff}^{p})\Lambda \tag{6.2}$$

where λ_{res} is the resonant wavelength, Λ is the grating period, n_{eff}^{0} and n_{eff}^{p} are the effective RIs of the fundamental and the higher-order mode.

Figure 6.16 demonstrates a transmission spectrum of a LPG written in conventional single mode fiber (SMF) with $\Lambda \approx 320\mu m$, the dip in the figure corresponding to the coupling from the fundamental mode LP_{01} to the cladding modes LP_{0x}. The advantages of LPG include ease of fabrication, low back reflection and compactness. Various LPG devices have been introduce for the use as in-fiber band-rejection filters [29], mode converters [30] and sensors for physical parameters such as temperature, strain and RI [31].

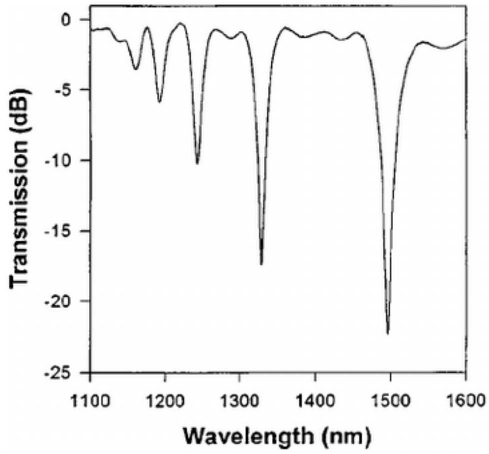

Figure 6.16 Transmission spectrum of a typical LPG on SM-28 fiber [32]

The modal property of 3-hole SC microcell has been studied previously in 3.3.2 by FEM method on 3-hole microcell cross-section model. By using the same model, the modal effective RIs are calculated for the LP_{01}-like, LP_{11}-like and LP_{21}-like modes. The results are summarized in Figure 6.17. We found that the microcell is a single-mode waveguide for $0.12 < r_{eff}/\lambda < 0.32$, where r_{eff} is the effective radius of the microcell and λ is the wavelength. For $0.32 < r_{eff}/\lambda$, the microcell can support several modes. Hence, by introducing an LPG satisfying (6.2), LPGs can be realized.

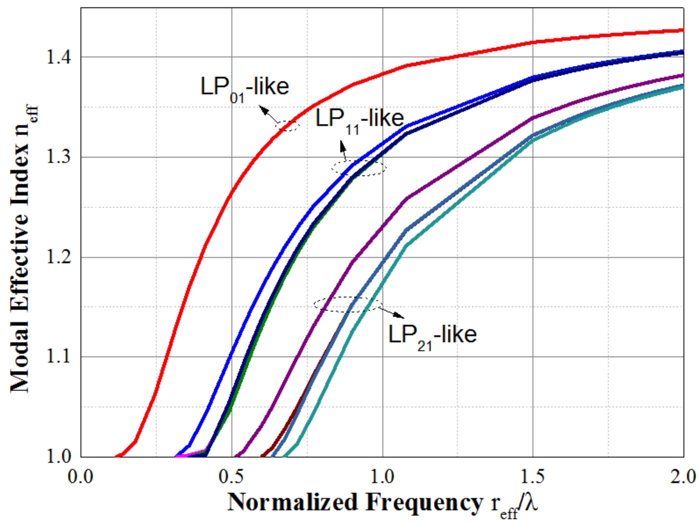

Figure 6.17 Effective RI n_{eff} of guided modes as functions of the normalized frequency r_{eff}/λ

From Figure 6.17, the RI difference between fundamental and higher-order modes in microcells is much larger than that in the standard SMFs. For example, the RI difference between HE_{11} (LP_{01}) and the nearest higher-order modes is ~ 0.07 for a microcell with r_{eff} ~1.5 μm at 1550nm, while the RI difference between HE_{11} and a cladding mode in a SMF is ~0.004. So, to achieve the resonant mode coupling, this larger RI difference would require a smaller grating period according to (6.2).

Based on equation(6.2), the phase-matching curves (Λ-λ) corresponding to the resonant couplings between the fundamental and the first group of higher-order modes (LP_{11}-like) can be calculated. Since the effective RI of $HE_{21\text{-}x}$ like, $HE_{21\text{-}y}$ like and TE_{01} mode are almost superposed in Figure 6.17, the grating period of these modes would be close in value. The calculated periods corresponding to HE_{11} -> TM_{01} and HE_{11} -> $HE_{21\text{-}x}$ like coupling in 3-hole SC microcells with radius from 2.1 to 0.6 μm are shown in Figure 6.18. The grating period decreases with the increasing wavelength from 1250 nm to 1650 nm. And a higher grating period is required for the microcell with larger core size.

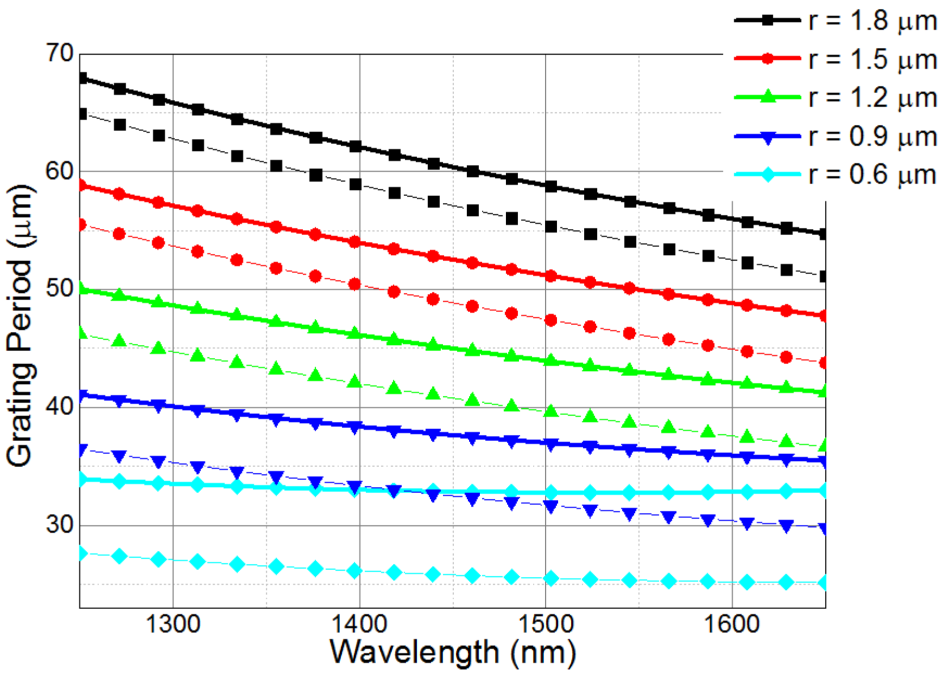

Figure 6.18 Grating pitches as the function of wavelength for modes coupling from HE_{11} to TM_{01} (thick line) and HE_{21-x} like (thin line) for microcells with different core radius

6.3.2 Fabrication and basic properties

There are many techniques can be used to inscribe LPGs on various fibers. Such as UV laser illumination [29], fs laser irradiation [33], CO2 laser irradiation [34], electrical arc discharge [35] and external mechanical pressure [36]. The fs laser irradiation technique is widely used in producing LPGs on MOFs because of high machining precision and workability independent of the fiber photosensitive. The periodic RI perturbation in this technique is produced by the radiation with intensity exceeding damage threshold of the material. So surface defects, such as micro-holes [37], scratches [38], are always exist on the MOF LPGs fabricated by this technique. The defects are detrimental to the mechanical properties of LPG.

Compared with the other MOFs, the microcell have a relatively simple cladding region construct by air cladding in thin jacket tube, which scatter little fs laser beam during the process. This features make the LPG on microcell can be inscribed directly on the core with low fs laser energy.

By scanning the focus of an fs laser beam across the core region, we successfully produced a LPG on the core of the 3-hole SC microcell while left the surface of microfiber intact. Figure 6.19 shows the fabrication setup. The instruments used for the LPG fabrication include broadband source (BBS) (Amonics ALS-CWDM-FA), polarization controller (PC), optical spectrum analyzer (OSA) (Yokogawa AQ6319) and fs laser micro-machining system (Ti:sapphire fs laser system + motorized stage systems + microscope).

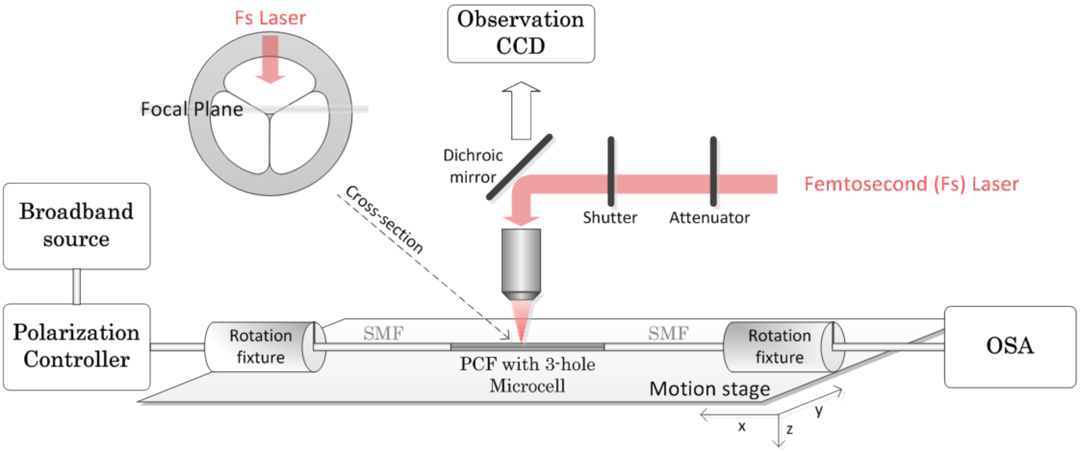

Figure 6.19 Schematic of the setup for LPG fabrication

The LPG was fabricated by point-by-point (PBP) fs laser irradiation. During the fabrication, the fs laser pulses (800nm, 120fs, 1k Hz) are focused via a 20x objective lens (NA0.5, WD2.1) on the upper surface plane of the core. A typical image of the 3-hole SC microcell observed from the LCD monitor is shown by Figure 6.3 in section 6.1. The energy of the fs laser pulse is ~0.18μJ which is much smaller than the other reported value used for producing LPG on MOFs [37, 38]. The focal spot of fs laser was moved along the Y direction to produce one point in the LPG by use of the three-axis translation stage as shown in Figure 6.19, and then moved along the X direction to the next point. The micrograph of LPG in microcell is provided in Figure 6.20. The estimated width of the laser-induced notch is ~2-3 μm, comparable with the spot size of fs laser focus.

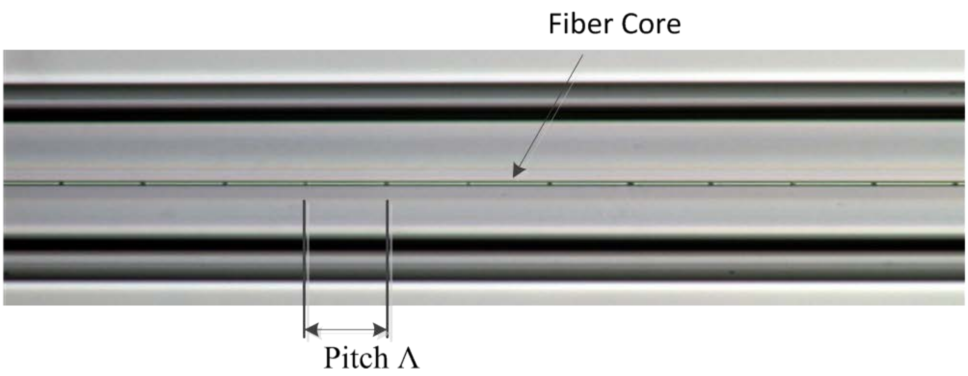

Figure 6.20 Micrograph of a section of LPG in the 3-hole microcell

For a microcell with ~1.5 μm core radius, the numerical calculation results with FEM software are summarized in Figure 6.21 (a). The coupling wavelengths of LP_{11}-like group are far apart to the wavelength of LP_{21}-like group. There are two possible resonance dips around 1350 nm and 1450 nm corresponding to coupling from HE_{11} (LP_{01}) to the modes in LP_{11}-like group would be formed on a microcell with ~53μm grating period. Figure 6.21 (b) shows the development of transmission spectrum during the process with increasing number of grating notch. The resonant dip reaches the maximum depth value with 31 notches. The transmission spectrum matches well with the calculated results. Since the coupling wavelength to the TE_{01} and HE_{21}-like (in LP_{21}-like group) are so close, the dip at 1331nm could be the coupling between HE_{11} to either of them. The missing of HE_{11}->TM_{01} resonant dip at ~1460 nm in Figure 6.21 (b) could be due to the polarization dependent mode coupling, because the strengths of the dips can be changed significantly by adjusting the PC.

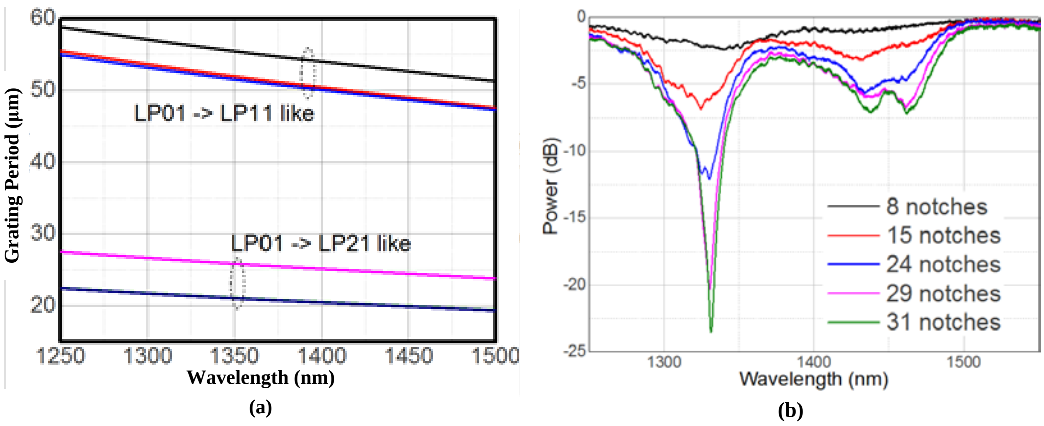

Figure 6.21 (a) Calculated LPG grating period as functions of wavelength for coupling from HE_{11} (LP_{01}) to LP_{11}-like and to LP_{21}-like modes for a 3-hole microcell with a core size ~3 um; (b) Measured transmission spectrums of the SC microcell LPG with increasing number of grating notches

The temperature response of a SC microcell-based LPG with a radius of ~1.5μm was measured by placing the LPG in a digitally controlled oven (ECOM LCO102) with temperature varying from 25 °C to 100°C. The results are shown in Figure 6.22. The sensitivity of dip wavelength to temperature is ~ -11.6 pm/°C, about 5 times smaller than that of an LPG in standard SMF [39] and close to LPGs on pure silica PCFs [40].

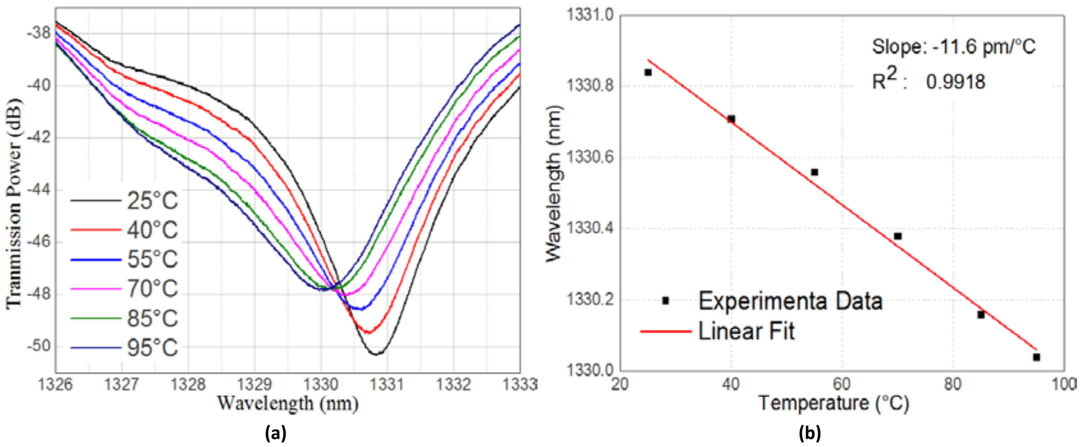

Figure 6.22 (a) Spectrum response of the LPG to temperature; (b) Dip wavelength as a function of temperature

The low temperature sensitivity may be explained with the aid of equation(6.3). The differential equation gives the temperature dependence of the LPG dip wavelength [33].

$$\begin{aligned}\frac{d\lambda_{res}}{dT} &= \Delta n\frac{d\Lambda}{dT}+\Lambda\frac{d\Delta n}{dT}\\ &=(n_{eff}^{0}-n_{eff}^{p})\frac{d\Lambda}{dT}+\Lambda\left(\frac{dn_{eff}^{0}}{dT}-\frac{n_{eff}^{p}}{dT}\right)\end{aligned} \tag{6.3}$$

In the right side of the equation(6.3), the first part describes the thermal expansion of the fiber core; the second part describes the thermal-optic effect of the fiber material. Since the two coupling modes are both exist in the same material region (microcell core), the thermo-optic coefficients of the both modes are almost indistinctive. The thermal optic effect part in (6.3) contributes little to the temperature sensitivity.

6.4 Summary

In this Chapter, the characteristics of the 3-hole SC microcell have been discussed. An optical gain cell is realized by infiltrating the laser dye solution (rhodamine 6G) into the microcell via the fs laser machined side holes and transversely pumped by a continue-wave green laser. In addition, the procedure to inscribe LPG on the core of microcell is demonstrated.

6.5 References

[1]. K. Kiang, K. Frampton, T. M. Monro, R. Moore, J. Tucknott, D. Hewak, D. J. Richardson, and H. Rutt, "Extruded singlemode non-silica glass holey optical fibres," Electronics Letters **38**, 546-547 (2002).

[2]. H. Ebendorff-Heidepriem, P. Petropoulos, S. Asimakis, V. Finazzi, R. Moore, K. Frampton, F. Koizumi, D. Richardson, and T. Monro, "Bismuth glass holey fibers with high nonlinearity," Optics Express **12**, 5082-5087 (2004).

[3]. M. Liao, C. Chaudhari, X. Yan, G. Qin, C. Kito, T. Suzuki, and Y. Ohishi, "A suspended core nanofiber with unprecedented large diameter ratio of holey region to core," Optics Express **18**, 9088-9097 (2010).

[4]. S. Afshar V, S. C. Warren-Smith, and T. M. Monro, "Enhancement of fluorescence-based sensing using microstructured optical fibres," Optics Express **15**, 17891-17901 (2007).

[5]. T. G. Euser, J. Chen, M. Scharrer, P. S. J. Russell, N. J. Farrer, and P. Sadler, "Quantitative broadband chemical sensing in air-suspended solid-core fibers," Journal of Applied Physics **103**, 103108-103108-103107 (2008).

[6]. J. Y. Leong, P. Petropoulos, J. H. Price, H. Ebendorff-Heidepriem, S. Asimakis, R. C. Moore, K. E. Frampton, V. Finazzi, X. Feng, and T. M. Monro, "High-nonlinearity dispersion-shifted lead-silicate holey fibers for efficient 1-μm

pumped supercontinuum generation," Lightwave Technology, Journal of **24**, 183-190 (2006).

[7]. J. Jensen, P. Hoiby, G. Emiliyanov, O. Bang, L. Pedersen, and A. Bjarklev, "Selective detection of antibodies in microstructured polymer optical fibers," Optics Express **13**, 5883-5889 (2005).

[8]. T. M. Monro, S. Warren-Smith, E. P. Schartner, A. François, S. Heng, H. Ebendorff-Heidepriem, and S. Afshar V, "Sensing with suspended-core optical fibers," Optical Fiber Technology **16**, 343-356 (2010).

[9]. S. C. Warren-Smith, S. Afshar Vahid, and T. M. Monro, "Fluorescence-based sensing with optical nanowires: a generalized model and experimental validation," Optics Express **18**, 9474-9485 (2010).

[10]. B. Helbo, A. Kristensen, and A. Menon, "A micro-cavity fluidic dye laser," Journal of Micromechanics and Microengineering **13**, 307 (2003).

[11]. Z. Y. Li, and D. Psaltis, "Optofluidic dye lasers," Microfluidics and Nanofluidics **4**, 145-158 (2008).

[12]. W. Song, A. E. Vasdekis, Z. Li, and D. Psaltis, "Low-order distributed feedback optofluidic dye laser with reduced threshold," Applied Physics Letters **94**, 051117-051117-051113 (2009).

[13]. B. Wajnchold, A. Umińska, M. Grabka, D. Kotas, S. Pustelny, and W. Gawlik, "Suspended-core optical fibres for organic dye absorption spectroscopy," in *Fifth European Workshop on Optical Fibre Sensors*(International Society for Optics and Photonics, 2013), pp. 87941B-87941B-87945.

[14]. B. Valeur, *Molecular fluorescence: principles and applications* (Wiley-Vch, 2001).

[15]. O. Svelto, *Principles of lasers* (Springer, 2010).

[16]. R. Kubin, and A. Fletcher, "Fluorescence quantum yields of some rhodamine dyes," Journal of Luminescence **27**, 455-462 (1983).

[17]. B. Huth, and M. Kagan, "Dynamics of a flashlamp-pumped rhodamine 6G laser," IBM Journal of Research and Development **15**, 278-292 (1971).

[18]. D. Beer, and J. Weber, "Photobleaching of organic laser dyes," Optics Communications **5**, 307-309 (1972).

[19]. G. J. Pendock, H. S. MacKenzie, and F. P. Payne, "Dye lasers using tapered optical fibers," Applied Optics **32**, 5236-5242 (1993).

[20]. C. Shank, J. Edighoffer, A. Dienes, and E. Ippen, "Evidence for diffusion independent triplet quenching in the rhodamine 6G ethylene glycol cw dye laser system," Optics Communications **7**, 176-177 (1973).

[21]. F. López Arbeloa, P. Ruiz Ojeda, and I. López Arbeloa, "The fluorescence quenching mechanisms of rhodamine 6g in concentrated ethanolic solution," Journal of Photochemistry and Photobiology A: Chemistry **45**, 313-323 (1988).

[22]. K. A. Selanger, J. Falnes, and T. Sikkeland, "Fluorescence Lifetime Studies of Rhodamine 6g in Methanol," Journal of Physical Chemistry **81**, 1960-1963 (1977).

[23]. A. Penzkofer, and Y. Lu, "Fluorescence Quenching of Rhodamine 6g in Methanol at High Concentration," Chemical Physics **103**, 399-405 (1986).

[24]. P. Runge, and R. Rosenberg, "Unconfined flowing-dye films for CW dye lasers," Quantum Electronics, IEEE Journal of **8**, 910-911 (1972).

[25]. D. R. Lide, and T. J. Bruno, *Handbook of Chemistry and Physics* (CRC PressI Llc, 2010).

[26]. B. Helbo, S. Kragh, B. Kjeldsen, J. Reimers, and A. Kristensen, "Investigation of the dye concentration influence on the lasing wavelength and threshold for a micro-fluidic dye laser," Sensors and Actuators A: Physical **111**, 21-25 (2004).

[27]. S. Smolka, M. Barth, and O. Benson, "Selectively coated photonic crystal fiber for highly sensitive fluorescence detection," Applied Physics Letters **90**,

111101-111101-111103 (2007).

[28]. S. Smolka, M. Barth, and O. Benson, "Highly efficient fluorescence sensing with hollow core photonic crystal fibers," Optics Express **15**, 12783 (2007).

[29]. A. M. Vengsarkar, P. J. Lemaire, J. B. Judkins, V. Bhatia, T. Erdogan, and J. E. Sipe, "Long-period fiber gratings as band-rejection filters," Lightwave Technology, Journal of **14**, 58-65 (1996).

[30]. K. Hill, B. Malo, K. Vineberg, F. Bilodeau, D. Johnson, and I. Skinner, "Efficient mode conversion in telecommunication fibre using externally written gratings," Electronics Letters **26**, 1270-1272 (1990).

[31]. X. Shu, L. Zhang, and I. Bennion, "Sensitivity characteristics of long-period fiber gratings," Journal of Lightwave Technology **20**, 255 (2002).

[32]. V. Bhatia, D. K. Campbell, D. Sherr, T. G. D'Alberto, N. A. Zabaronick, G. A. Ten Eyck, K. A. Murphy, and R. O. Claus, "Temperature-insensitive and strain-insensitive long-period grating sensors for smart structures," Optical Engineering **36**, 1872-1876 (1997).

[33]. Y. Kondo, K. Nouchi, T. Mitsuyu, M. Watanabe, P. G. Kazansky, and K. Hirao, "Fabrication of long-period fiber gratings by focused irradiation of infrared femtosecond laser pulses," Optics Letters **24**, 646-648 (1999).

[34]. G. Kakarantzas, T. Birks, and P. S. J. Russell, "Structural long-period gratings in photonic crystal fibers," Optics Letters **27**, 1013-1015 (2002).

[35]. G. Rego, O. Okhotnikov, E. Dianov, and V. Sulimov, "High-temperature stability of long-period fiber gratings produced using an electric arc," Lightwave Technology, Journal of **19**, 1574-1579 (2001).

[36]. J. H. Lim, K. S. Lee, J. C. Kim, and B. H. Lee, "Tunable fiber gratings fabricated in photonic crystal fiber by use of mechanical pressure," Optics Letters **29**, 331-333 (2004).

[37]. S. Liu, L. Jin, W. Jin, D. Wang, C. Liao, and Y. Wang, "Structural long

period gratings made by drilling micro-holes in photonic crystal fibers with a femtosecond infrared laser," Optics Express **18**, 5496-5503 (2010).

[38]. C. Liao, Y. Wang, D. Wang, and L. Jin, "Femtosecond laser inscribed long-period gratings in all-solid photonic bandgap fibers," Photonics Technology Letters, IEEE **22**, 425-427 (2010).

[39]. V. Bhatia, "Applications of long-period gratings to single and multi-parameter sensing," Optics Express **4**, 457-466 (1999).

[40]. S. Liu, L. Jin, W. Jin, Y. Wang, and D. Wang, "Fabrication of long-period gratings by femtosecond laser-induced filling of air-holes in photonic crystal fibers," Photonics Technology Letters, IEEE **22**, 1635-1637 (2010).

Chapter 7 : Conclusions and Future Works

7.1 Conclusions

In this dissertation, the novel in-fiber suspended core (SC) microcells fabricated from commercial available PCFs were proposed. A modified hole-inflation technique for PCFs was used in the fabrication of the microcells which would be useful in a number of applications. Six types of microcells with different interior structure have been practically made. Based on the three types of the microcells, i.e., the 3-, 4-, and 6-hole microcell, which are fabricated by inflating the innermost ring of holes, the following novel devices were demonstrated.

- Based on the 6-hole SC microcell, a novel micro-cantilever was built inside the microcell. It was demonstrated that the cantilever acts as a robust accelerometer. The purposely introduced initial offset makes the cantilever linearly responded to the acceleration, with a sensitivity of ~2.6 mV/g and a flat frequency response up to ~2.5kHz.
- The fundamental mode of a 4-hole microcell exhibits a high birefringence (up to ~3 x 10^{-2} in calculation). The birefringence is highly sensitive to the RI around the core. Integrating the device within a Sagnac loop interferometer, a sample linearly responded to the pressure with a sensitivity of ~0.31 nm/Bar. With the same test structure, but filling the microcell with a refractive index (RI) oil, a high sensitivity temperature sensor (~3.04nm/°C) is demonstrated.
- Based on the 3-hole microcell, an optical gain cell was produced by infiltrating a solution of laser dye (Rhodamine 6G) into the microcell via the side holes drilled with a femtosecond (Fs) laser. About 2 dB net optical gain

was achieved with a 10 millimeter cell at 633 nm when it was side pumped with a 100mW 532nm laser. Furthermore, LPG was successfully inscribed on the core of microcells with the fs laser and the point-by-point method.

7.2 Suggestion for future works

The fabrication techniques developed in this dissertation is highly dynamic in fabricating SC microcells with various interior structures. However, there is still scope for improvement; for example, how to further reduce the diameters of the SC down to the submicron size. A SC microcell with submicron core would have a larger evanescent field and enhanced nonlinearity effects, which might enable the microcell to exhibit good performance in many new applications, such as evanescent wave gas sensing and supercontinuum generation. Careful coordination of the gas pressure and drawing speed might help to achieve this goal.

Another fabrication issue worthy of further investigation is how to use an alternative heating source, such as a CO_2 laser, small scale discharge, in the selective inflation process for producing short microcells. Compared with the electrical discharge in fusion splicer, the focused CO_2 laser beam has a smaller heat region. It is possible to fabricate microcells with new features, such as smaller longitudinal size, asymmetric expansion.

Six types of SC microcells have been reported in this dissertation. However, three of them have not been studied on their optical features and applications. Furthermore, more microcell types can be fabricated by selecting new holes combination in fabrication which would provide further possibilities

Some SC microcell applications presented in this dissertation are just preliminarily investigated. The performance of the in-fiber devices could be further improved, and new applications could be found. For example, the gain of the optical amplification cell may be improved by adopting a higher power pumping source and optimizing the connection between the PCF and SMF. Different and multiple laser dyes may be infiltrated into the different holes of the microcell to produce a broadband spectrum, and a fiber laser in the visible wavelength region may be developed by incorporating these cells in a fiber cavity.